Dexterity and Guidance Without Automation: Surgical Robot-Like Capabilities at a Fraction of the Cost

By

Ray A. Lathrop

Dissertation

Submitted to the Faculty of the

Graduate School of Vanderbilt University

in partial fulfillment of the requirements

for the degree of

DOCTOR OF PHILOSOPHY

in

Mechanical Engineering

May, 2014

Nashville, Tennessee

Approved:

Robert J. Webster, III

Nabil Simaan

Michael Goldfarb

Robert L. Galloway, Jr.

Stanley Duke Herrell

Acknowledgments

I would like to acknowledge and thank the following people who were influential in the completion of this work:

Dr. Galloway and Dr. Netterville who provided the foundational "needs" on which my work was built.

The members of Dr. Galloway's Surgical Navigation Apparatus Research Laboratory who provided help and assistance during the development of the Conoprobe based surface scanner.

The development of the surface scanner and the dexterous surgical tools relied heavily on many of Vanderbilt's medical collaborators. Dr. Herrell contributed in part to all the areas of research covered in this work. Of particular help was offering insights into what makes the da Vinci Surgical System work so well from a surgeon's point of view. Dr. Herrell, along with Dr. Russell was also instrumental in gathering willing or semi-willing surgeons to participate in my user study.

The members of my lab have always been supportive in countless ways. Any time I needed a bigger brain, I could count on my lab mates.

Bob has been a great advisor and supporter. He has a remarkable ability to see where an idea is going and craft that into a research hypothesis. His general support and enthusiasm has allowed me to take something I was interested in and turn it into this thesis. I look forward to future collaboration with both Bob and the MEDLab.

I would like to thank Martha for her moral support during the writing of this document. It was certainly needed at times. I would also like to thank her for getting the defense room.

Sadly, I haven't been able to share this accomplishment with Prof. Kos Ishii who passed away in 2009. The MML will not be the same without him.

Finally, I would like to thank Mary. Were it not for her suggestion I might never have started on this long path.

Abstract

This dissertation offers ways that the dexterity and guidance associated with image-guided robotic surgery can be delivered without automation. The overall objective is to provide highly capable instruments to surgeons, which can, in principle, be produced for a lower overall cost or with greater overall capabilities than the robotic and image guidance systems currently on the market. Of particular interest is creating a system for soft tissue image guidance in a laparoscopic surgical setting, and designing laparoscopic tools that can deliver dexterity similar to robotic surgical systems without the need for the robot.

Existing surgical registration systems for use in the abdominal cavity have used laser triangulation or contact swabbing with a tracked probe to gather the point clouds of organ surfaces. These point clouds are used to register the preoperative imaging to the work site. This dissertation describes a new scanning system used to gather these point clouds which is unlike prior systems because it requires no automation (indeed, it can be constructed inexpensively from off-the-shelf components), is contactless, and can work through a laparoscopic port. The system pairs a laser range finder with a standard optical tracking system.

This dissertation then addresses the kinematic design of high dexterity tools with particular attention to creating natural user interfaces. Since there exists no definition in the literature for what constitutes a "natural" user interface for an articulated manual laparoscopic tool, this dissertation puts forth a metric and a design guideline to design for "naturalness" in this context. A user study is then used to explore the

performance of several competing instrument designs in the context of the metric and design guideline. Finally, the manner in which these results can inform surgical instrument design is illustrated in a description of a prototype designed for throat surgery.

This dissertation then proceeds to consider natural user interfaces from an elastic energy perspective. Under the assumption that a statically balanced mechanism that transparently transfers user motion to instrument tip motion is most natural, this dissertation sets about determining how energy storage elements used in laparoscopic "wrists" or "elbows" can be statically balanced with additional elastic elements. Without static balance in these mechanisms, the stored energy is felt by the user as a restorative force trying to return the device to a neutral position. If the tool is required to have significant joint stiffness, the restorative force felt by the user may be too high for practical surgical use. This section of the dissertation culminates with the design of a novel, manual, laparoscopic prototype tool with both wrist and elbow joints that features a statically balanced continuum joint.

The conclusion of this dissertation is that with appropriate mechanical design and sensor choices it is possible to deliver many of the advantages promised by image-guided robotic systems in manual devices. These devices can, in principle, be produced much less expensively than robotic systems providing similar capabilities. This paves the way for a future in which advanced surgical capabilities are delivered in a manner which places a lower financial burden on the overall health care system.

Table of Contents

List of Figures

List of Tables

Chapter 1

Introduction

Image-guided robotic surgery encompasses a wide range of technologies and has many potential applications. It represents an exciting intersection of recent engineering innovations and medical awareness of the potential of combining image guidance and robotics. Even robots alone offer a number of potential advantages and enhancements to traditional surgical methods. An example is Intuitive Surgical's da Vinci Surgical System [2], which is now in common use. The da Vinci system provides many of the benefits associated with surgical robotics. For example, the innovative Endowrist provides an additional two degrees of freedom to the surgical tools in the form of a wrist at the tool's end. But the da Vinci system does more than just provide a wrist. The natural mapping of the user interface to that wrist enables surgeons to smoothly coordinate those additional degrees of freedom. This enables complex motions in space in a way that had not previously been possible with conventional laparoscopic tools.

Image guidance is also valuable on its own, independent of a robotic system. Using imaging to guide surgery is actually a very old technique. The first application of imaging to guide a procedure was in 1895 in Birmingham, England, when an X-ray image, made just eight days after Roentgen's first paper on the subject, was used to aid in the removal of an industrial sewing needle from a woman's hand [21]. Cleary and Peters suggest that the modern era of image-guided interventions and surgery has been around for approximately two decades. What distinguishes the modern era

is the visualization capabilities that have become available.

Preoperative imaging gives surgeons a map of the surgical field before the patient enters the operating room. This map can be used for procedure planning and real-time navigation during surgery. Indeed, the process is analogous to the way a car's Global Positioning System (GPS) receiver aligns the computerized representation of the world (the electronic map in the computer's database) with the location of the car on a street in the physical world. The same thing is accomplished in the surgical world when preoperative medical images are registered to the patient in the operating room. When surgical tools are tracked, their locations can be continuously displayed with respect to the subsurface anatomical features.

But this "surgical GPS" can do more than just show the surgeon the locations of tools with respect to preoperative images. Additional images and other information such as the location of critical subsurface features or a resection plane can be overlaid directly into the surgeon's visual field [36] [96] [30] [27].

1.1 Image Guidance in Robotics

The da Vinci system provides binocular endoscopic visualization with a camera controlled directly by the surgeon rather than by an assistant. This alone is an enhancement over the typically monocular manual laparoscopic systems, but research groups have also taken things a step further. Zuzak created enhanced vision with wide spectrum cameras and near infrared light to differentiate between chromophores in anatomical structures [111]. Mid-infrared light was used by Roberts et al. to identify blood vessels and other anatomical structures in animal studies [80]. Both of these

efforts used the ability of the camera to see beyond the visible spectrum to detect extra information which was then overlaid on the surgeon's video image. Because the visible image and the extra information come from the same camera, they are inherently registered.

But this only lets the surgeon see what is on the surface or just under the surface in some cases. An obvious wish is for "X-ray vision" to see deep under the surface. Given the colloquial terminology of "X-ray vision," it is perhaps fitting that actual X-ray images can be used for this purpose. X-ray-based tomographic images can be registered to the space of the robot and patient to provide this capability. The benefits of performing image-guided surgery using these registered images have been of interest in research for over two decades [21].

There is great value for the surgeon in combining robotics (to enhance dexterity) and image guidance (to enhance accuracy) simultaneously. With augmented reality video displays, margins and critical structures can be seen on the same endoscopic video display of the da Vinci system's surgical console [90]. The location of the robotic tool tips can also be tracked and projected as an overlay on the preoperative surgical imaging [41].

1.2 The Price Paid

The problem with these excellent robotic and image-guidance systems (and the combinations of the two) is cost. The da Vinci system, due to its widespread use, is now being considered from a cost effectiveness point of view. The system is an obvious target given the high purchase price and tool cost. Purchase price claims range from

$1.3 million to $2.0 million [77] [103] for just the initial system. The da Vinci system is estimated to add approximately $1500 to the cost of a surgical procedure with approximately half of that being the cost of the limited-life tools [77]. Added cost alone is not a concern if it comes with sufficient added benefit. Here again, in the case of the da Vinci system, the cost to benefit ratio can be questioned [59]. A robotic system has an inherent cost disadvantage over a similar manual system. Both systems will have mechanical parts like graspers, tool shafts, and even user-input controls. To this the robot must add motors, sensors, computers, and corresponding additional physical structure. There is also the potential need for additional space in a crowded operating room.

In the context of image guidance, the goal in this dissertation is not to reduce costs with respect to the state of the art, but rather to increase capabilities without adding significant additional cost. The image-guidance systems currently used in surgery are limited in their ability to register structures *inside* the closed abdomen, since they typically require physical probes to be scraped across the surface of the organ to be registered. The disadvantages of this approach include loss of accuracy because of tissue deformation and potential trauma to the organ, and are described in detail in Chapter 2. Contactless approaches are a better option, and if one wishes to use these with a robotic system, there is a need for them to be deployable through a laparoscopic port. This is also true if one wishes them to be used with manual laparoscopic tools such as those described in Chapters 3-6 of this dissertation. There currently exist no commercial image guidance systems able to achieve this.

This begs the question: "Can the benefits of image-guided robotic surgery be

delivered at a lower cost through a manual approach?" Answering this question is the central objective of this dissertation. Toward this goal, this work will discuss technologies and tools which could ultimately be used to deliver dexterity similar to that of a robotic surgical system at a lower cost. Similarly, the development of an inexpensive, surface scanner that can be used laparoscopically could enable many of the benefits of image-guided da Vinci surgery in a manual surgical setting.

1.3 Contributions of This Work

The contribution of Chapter 2 is a new laparoscopic system for soft tissue preoperative image registration. This system is novel for a combination of reasons. First, it is based on existing industrial technology which is robust and low cost. Second, it operates through a single endoscopic port. Third, it does not require cooperative use of a traditional endoscope. Fourth, its accuracy is as good as or better than existing surface-scanning technologies.

The contributions of Chapters 3 are the development and evaluation of a metric and a guideline for the evaluation of the "naturalness" of manual user interfaces for high dexterity laparoscopic tools. Only a few examples of manual, high dexterity tools exist in the commercial or academic space. The user interface designs for these tools have been conducted in an ad hoc manner and vary widely, with a marked difference between the interfaces illustrated in the commercial and research worlds. Chapter 3 proposes methods based on kinematics to guide the design of a natural user interface and then tests their predictions with a user study.

Chapter 4 applies the methods of Chapter 3 to the design of a working prototype

dexterous tool. The focus of this particular tool is surgical procedures in the throat. This is the first articulated manual laparoscopic tool specifically designed for throat surgery of which the author is aware. The contributions of this chapter are the design optimization methods used in the creation of this tool and the novel design of a user interface which conforms with the previously presented definitions of naturalness.

Chapter 5 contributes an energy-based approach to static balancing of a continuum joint for hand-held articulated laparoscopic instruments. The use of static balancing with a manual laparoscopic tool opens the possibility of using high stiffness continuum joints in manual surgical tools. Prior to this work, the restorative forces of these joints made them impractical solutions for non-robotic surgical systems.

Chapter 6 describes the use of one of the static balance approaches from Chapter 5 to create a novel, manual dexterous tool with both a 2 degree-of-freedom wrist and 2 degree-of-freedom elbow. This is the first example of which the author is aware in which a multi-backbone continuum section has been incorporated into a manual surgical tool. Previously, multi-backbone devices have always been robotically actuated.

Chapter 2

Minimally Invasive Surface Scanning for Registration

As outlined in the introduction to this dissertation, there are significant potential benefits to image-guided surgery. The ability to register preoperative imaging to the physical world and the location of physical tools into preoperative images is critical to achieving these benefits. In the automotive world, a GPS receiver enables an electronic map to display a car's location in real time. The surgical registration system acts as the GPS which aligns the electronic, preoperative images with the physical world. Several means to achieve this exist, but all have some limitations that are addressed by this work.

This chapter describes a novel laparoscopic system for soft tissue, preoperative image registration. While relying on low cost, robust hardware, this system is able to operate through a single endoscopic port without relying on a specialty endoscope. This non-contact system delivers accuracy better than existing surface-scanning technologies.

In order to demonstrate the above, a series of experiments described in this chapter will provide experimental proof of concept and accuracy assessment for the system. In validating the system, a series of experiments will be described. The first experiments (Section 2.4) will ensure the laser range finder can be reliably used with biological tissue. Upon ensuring the selected sensor would reliably scan tissues, a complete system was constructed. The complete system was put through a series of test scans investigating known shapes as verification experiments (Section 2.6.3).

Finally, two experiments simulating an image-guided manual and an image-guided robotic procedure were conducted (Sections 2.7 and 2.8).

Some material in this chapter has been previously published by the author in [55–57].

2.1 Background on Minimally Invasive Surface Registration

To assist with surgical decision making, it is useful to display to the surgeon in real-time the position and orientation of surgical tools with respect to internal anatomical structures that cannot be directly viewed. One method of accomplishing this with intraoperative imaging is through image overlay, where a semi-transparent display (e.g. a half-silvered mirror) displays internal features at the correct spatial location with respect to anatomy, allowing the surgeon to visualize structures beneath the surface that otherwise cannot be seen [27, 30, 96].

However, often one does not have access to intraoperative imaging, or such imaging (e.g. ultrasound) is lower quality than the preoperative images available (e.g. computed tomography [CT] or magnetic resonance imaging [MRI]). In some areas of the body, such as the skull, a rigid registration can be performed based on fiducials or bone features to align preoperative image space with physical space (see [12] or [74] for an overview). Thorough overviews of the state of the art in all the various aspects of registration and its application in image-guided surgery are available in [31, 73]. While fiducial-based rigid registration works well in bone, soft tissues lack suitable alignment features and cannot support rigid screw connections, which makes registration more challenging. Because of this, surface-based registration is often employed

in soft tissues.

Surface-based registration typically involves matching a segmented preoperative image to a large number of organ surface points collected intraoperatively. An optically tracked touch-probe-based system has been used for this purpose by Maurer et al. for registration of segmented CT images to the skull [61]. Herline et al. applied the same contact-based concept to soft tissue (liver) registration [40]. One drawback of touch probes for registration is that the applied pressure deforms the organ surface, reducing the accuracy of registration. Furthermore, care must be taken to avoid inducing trauma or irritation to the organ surface via the probe. These issues inspired the development of non-contact surface-scanning techniques.

A common method of non-contact scanning is the use of a laser range scanner (LRS). LRS systems work by triangulating the location of a projected laser point. With knowledge of the direction of projected laser light and an observation of where it appears in a camera image, one can determine the location of the illuminated point in 3D space. Rapidly panning the laser allows the LRS to acquire a large number of points without physically moving the sensor. LRS has been applied to intraoperative liver registration [19], and used together with additional sources of information such as video for real-time organ tracking and/or enhanced registration accuracy [33, 65].

The system of Cash et al. [19] is of particular interest with respect to our current work, because the system we describe addresses similar clinical objectives and works in nearly the same way, except that our technique can be deployed minimally invasively. Cash et al.'s system consists of an optical tracker that tracks surgical tools and an LRS unit. Registration of preoperative image data to organ surface points

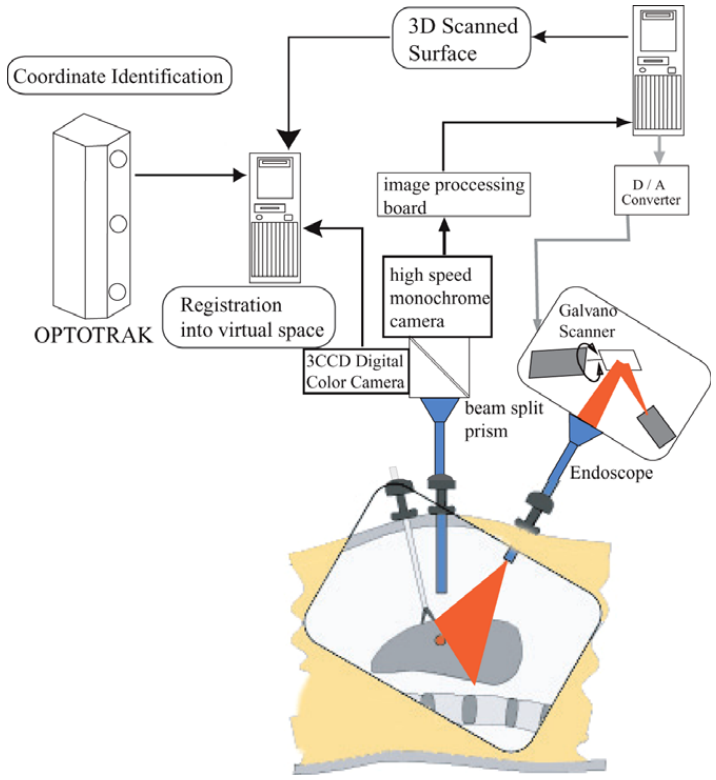

Figure 2.1: Two-port endoscopic surface scanner created by Hayashibe et al.

collected by the LRS allows the position of surgical tools and subsurface anatomy to be displayed in real time on a computer display to guide surgical decision making before and during incisions. Registration of the preoperative image is performed via the Iterative Closest Point (ICP) algorithm [11]. This work was the foundation of the commercial SurgiSight system (Pathfinder Therapeutics Inc., Nashville, TN). The primary drawback of LRS surface registration as currently implemented is its requirement of wide exposure of the organ of interest to enable the LRS to triangulate points.

Hayashibe and Nakamura proposed a system similar to LRS but introduced through endoscopic ports [37]. One port contained a scanning laser emitter while a second port

contained an endoscope modified with a beam splitter. The beam splitter allowed visible light to continue to a traditional color CCD camera. The location of the scanning laser point was fed to a high speed monochromatic camera. Inherent to the function of an LRS system is knowing the location of the receiver with respect to the transmitter. Normally the transmitter and receiver are rigidly attached in a single unit. By splitting the component parts of an LRS, Hayashibe and Nakamura established the relative position of the two components using an optical tracking system. Optically tracked markers were attached to the camera and laser scanner, enabling the system to know their relative locations. Though providing non-contact laparoscopic surface scanning, a drawback of this system is the need to modify the endoscope with a beam splitter, second camera, and optical tracking markers. Additionally the system required a custom-manufactured laser scanner. The system proposed in this chapter overcomes both limitations and also can operate through a single port alongside the conventional endoscopes already in use. The layout of this system is shown in Figure 2.1.

Another approach to surface scanning is the BrainLAB z-touch system [78], where the optical tracker tracks the laser dot on the tissue surface directly, rather than fiducials on the LRS emitter base unit. This has the advantage of removing calibration between the fiducials and the LRS coordinate system as a source of error. It also has the advantage of enabling the surgeon to directly specify the points collected (ensuring that they all belong to the organ of interest) in a manner similar to "painting" the desired organ surface with a laser pointer. The main drawback is that wide exposure is still required to enable all cameras in the optical tracking system to visualize the laser

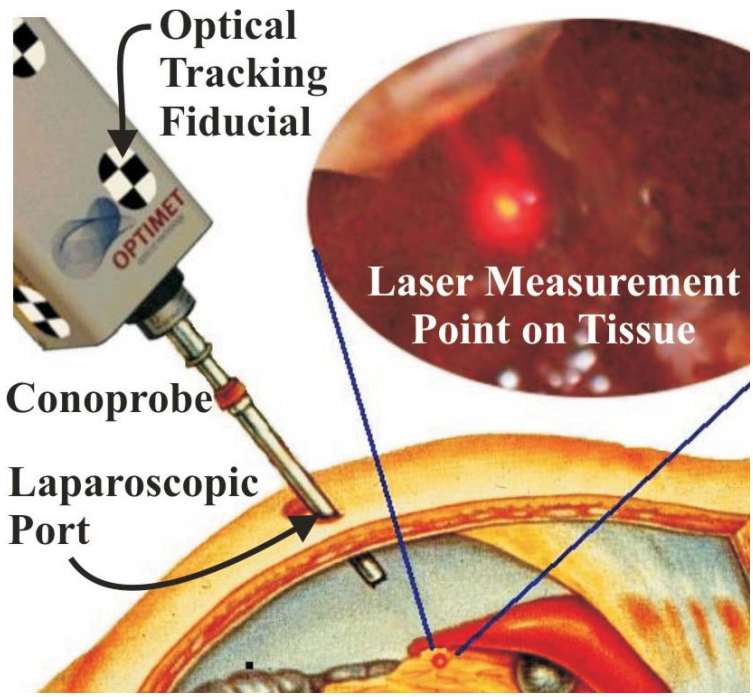

Figure 2.2: Conceptual drawing of organ surface scanning using conoscopic holography. The tracked Conoprobe returns distance measurements which are converted to a point cloud that defines the shape of the tissue surface.

dot. The tracked Conoprobe system we describe in this paper retains the advantage of being able to "paint" the desired surface, but does so minimally invasively.

Perhaps the most similar system to the tracked Conoprobe we propose in this paper is the Medtronic FAZER, a part of the Stealth Station (Medtronic Inc., Minneapolis, MN), which has been used for CT head registration [86]. This system uses a tracked 1D laser range finder that returns distance measurements which can be converted into 3D points. While little technical information is available about the proprietary FAZER system, the relatively large size and shape of the hand-held emitter suggest a triangulation approach is employed, which would preclude single-port minimally invasive use of the device. In any case, there has been no reported investigation to date of using the FAZER through a laparoscopic port.

2.2 Conoscopic Holography-Based Surface Scanning

To provide a low-cost, non-proprietary, minimally invasive alternative for collecting an intraoperative point cloud and thereby enable soft tissue image guidance, we propose the conoscopic holography-based system as illustrated in Figure 2.2. Here, a Conoprobe ($5,000 Conoprobe Mark 3, Optimet Optical Metrology Ltd., Jerusalem, Israel) is fixed to one end of a hollow tube, which passes through a standard laparoscopic port. The Conoprobe is tracked using an optical tracking system and provides distance measurements to points on tissue. As the laser point is traced over the organ surface by appropriate manual manipulation, a cloud of surface points on the organ is produced. As a side note, we have observed that it is possible to redirect the laser beam with a mirror over significant distances without compromising distance measurement accuracy, so automated aiming systems at the tip of the laparoscopic tube are also possible with a Conoprobe. While our particular application of abdominal soft tissue scanning does not require automation, it may be useful in other future applications (see, for example, the hearing aid fitting system of Prasciolu [76], which uses a micro mirror to bounce the laser over short distances).

2.3 Experiments: Overview and Testbed

A series of experiments were conducted to assess the feasibility of applying conoscopic holography for minimally invasive image registration to soft tissues. The first experiments were to test the ability of the Conoprobe to measure distances to various surfaces in an accurate and repeatable manner. While the sensor claims sufficient

accuracy for the task, this accuracy assumed opaque surfaces such as metal. These experiments are described in Sections 2.4 and 2.5. The mirror-aiming technique was inspired by the work of Prasciolu [76]. Of specific interest was whether this technique could work over distances greater than demonstrated in Prasciolu's work.[1]

The second set of experiments integrated optical tracking of the Conoprobe (Section 2.6). The 3D measurement abilities of the system were tested. The initial measurements involved scanning surfaces of known geometry.

A final pair experiments described in Sections 2.7 and 2.8 simulated the placement of surgical needles in the liver using preoperative images for guidance. In both experiments, an anthropomorphic silicone liver phantom model was CT scanned, and a Conoprobe-enabled surface scan was used to register the CT volume to physical coordinates. In the first experiment, a straight needle was inserted to desired targets identified in the CT volume. In the second experiment, a steerable cannula (described later) was registered with respect to the phantom and deployed to the target. The basic setup for these experiments is shown in Figure 2.3. The specific cannula needle setup is shown in Figure 2.15.

Before discussing each of these various experiments in detail, the major component parts of the overall scanning system and experimental setup will be described.

[1]We note that such a mirror-aiming system can be considered a future add-on to a conoscopic holography system such as that shown in Figure 2.2. Such an add-on to the system has the potential advantage of relieving the doctor from manually manipulating the Conoprobe base unit, but has the potential drawback of giving the doctor less control of the exact tissue scanned.

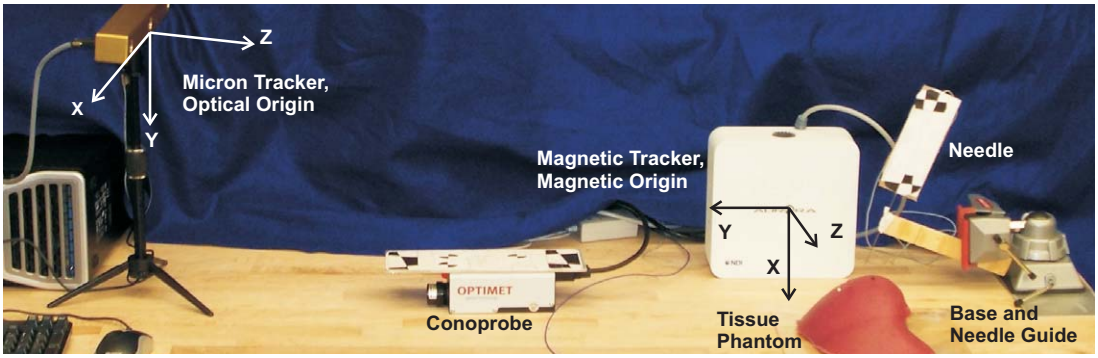

Figure 2.3: Experimental setup for surface scanning using the tracked Conoprobe and targeting needle. Optical and Magnetic origins are indicated. The black and white optical tracking fiducials can be seen on the Conoprobe and needle assembly.

Conoprobe

The principles by which conoscopic holography measures distance were proposed by Sirat et al. [93, 94]. The system illuminates an area of interest with a columnated light source. The cone of light returning from the illuminated area is filtered, then enters a birefringent crystal (See Figure 2.4). Inside the crystal, constructive and destructive interference occurs, which results in a Fresnel pattern from which distance can be deduced. Conoscopic holography is currently used for distance measurement in industrial profilometers, where it is combined with a motorized X-Y stage. This enables highly accurate measurements of dimensions on machined components, and is useful for manufacturing process control.

The published specifications for the Conoprobe Mark 3 (Optimet, Inc.) with a 200 mm objective lens list a measurement precision of <70 μm. The lateral size of the laser measurement spot is 170 μm. Specifications for the 250 mm lens used in our experiments are not published, but are similar. It is also known that surfaces which diffuse the red laser light of the scanner can reduce accuracy of the measure-

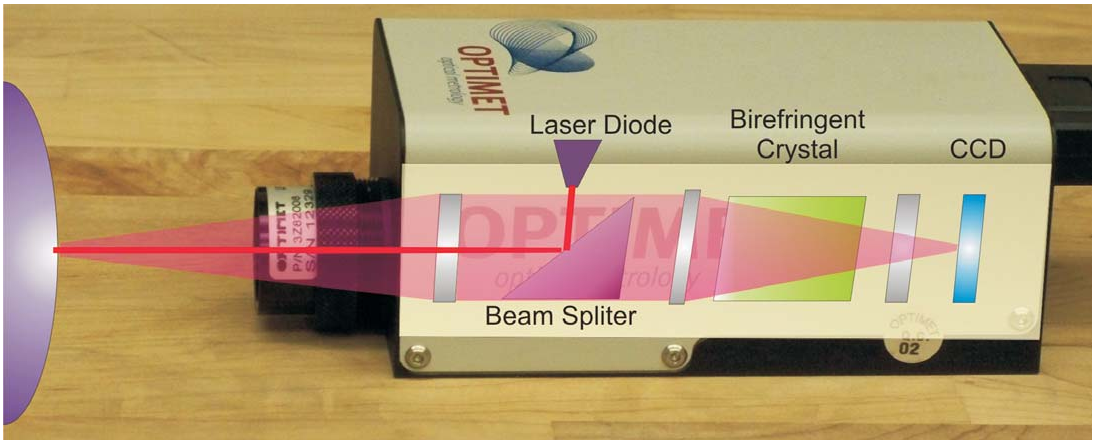

Figure 2.4: A photograph of the Optimet Conoprobe Mark 3.0, the off-the-shelf conoscopic holography system used in our experiments, which collects high precision distance measurements. Superimposed is a conceptual diagram of the basic components generally used in conoscopic holography to process returning light. The end product is an interference fringe pattern on the CCD sensing array at the back of the device, from which distances are computed.

ment, which motivates our experiments in Section 2.4 to validate the precision of the Conoprobe under these conditions.

The measurement range of the Conoprobe depends on the focal length of its lens. With a 250 mm lens the range is 155-337 mm. Since light returns from the measurement spot to the Conoprobe in a conical shape, one must also ensure that the trocar will cause minimal interference with the returning light. Using the inside diameter of the lens barrel (22.8 mm) for the base of the cone, the return beam will be 10 mm (a typical trocar diameter) wide at 44% of its return path. Thus, the distance between the trocar and the desired measurement point must be 0-148 mm for our particular lens. We note that these values can be designed as desired by choosing the appropriate lens focal length and trocar diameter.

The Conoprobe has two primary adjustments used to optimize the system to the properties of the surface to be measured. These are laser output power and sampling

frequency of the CCD. Together, these two settings determine the total light gathered by the CCD. Increasing laser power and decreasing the sampling rate (increasing sampling period) both increase the CCD's exposure. Thus the settings are analogous to increasing the ambient lighting and exposure time in conventional photography.

Optical Tracker

In the experiments that follow we use the MicronTracker 2 H3-60 (Claron Technology, Inc.). This is a passive optical tracking system that uses black and white checkerboard fiducials to identify and track objects in its field of view. The sensor head contains three 1280×960 pixel cameras whose images are processed using software supplied by the manufacturer to produce a coordinate frame transformation of the fiducial which is rigidly attached to the surface of the Conoprobe. The H3-60 has a roughly wedge-shaped workspace extending from the sensor head, and targeting accuracy of a single vertex is specified by the manufacturer at 0.20 mm. The maximum sample rate is 15 Hz, which in our initial proof-of-concept experiments also defines the maximum data capture rate of the system. Note that the Conoprobe measurements can be collected at significantly higher frequencies, since exposure time of its internal CCD elements is approximately 1-3 ms, depending on light levels. If a higher update rate is desired, it can be achieved simply through use of an optical tracker with a faster update rate. The Conoprobe and camera measurements are synchronized via a timing pulse sent from the Conoprobe to the camera.

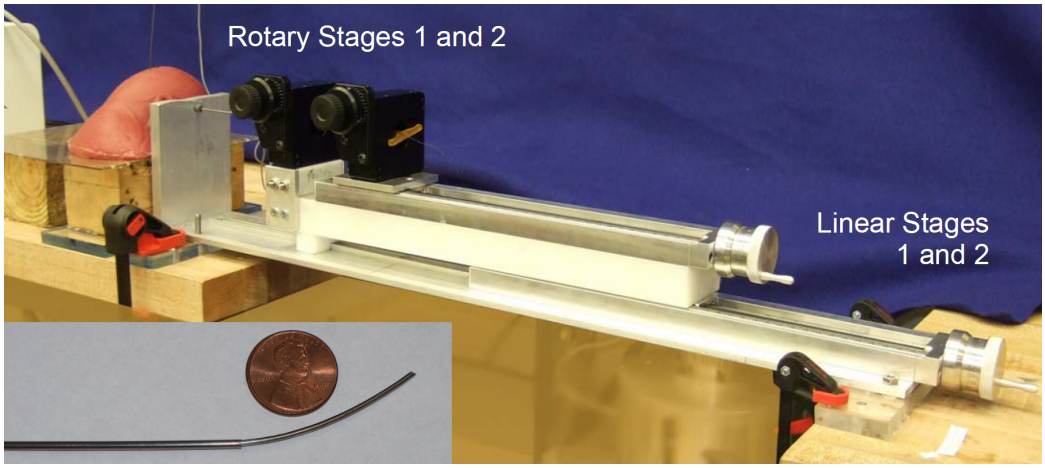

Figure 2.5: Manual cannula actuation unit and coaxial tubes (inset). The rotary stages independently rotate each tube axially. The primary linear stage, on the bottom, advances both tubes simultaneously. The secondary stage, on the top, advances only the inner tube and operates relative to the primary stage.

Manual Cannula Actuation Unit

The steerable steerable cannula system [84, 107] used in this study is a manually manipulated system that can specify the translation and axial rotation of each of its flexible, pre-bent, component tubes accurately (Figure 2.5). The component tubes are located coaxially within one another. The final shape of the steerable cannula results from the deformations of the individual tubes apply to one another. The details of this operation is described in Section 2.8.2. The manual actuation unit in this experiment consists of 2 rotary (Velmex small rotary table A5990T3) and 2 linear (Velmex model A25 series UniSlide linear slide) stages. These enable a rotational resolution of 0.1 degree and linear resolution of 0.01 mm. A Matlab implementation of the cannula inverse kinematics model (described in Section 2.8.2) yields the necessary rotational and linear positions of all four actuators, given a desired tip position.

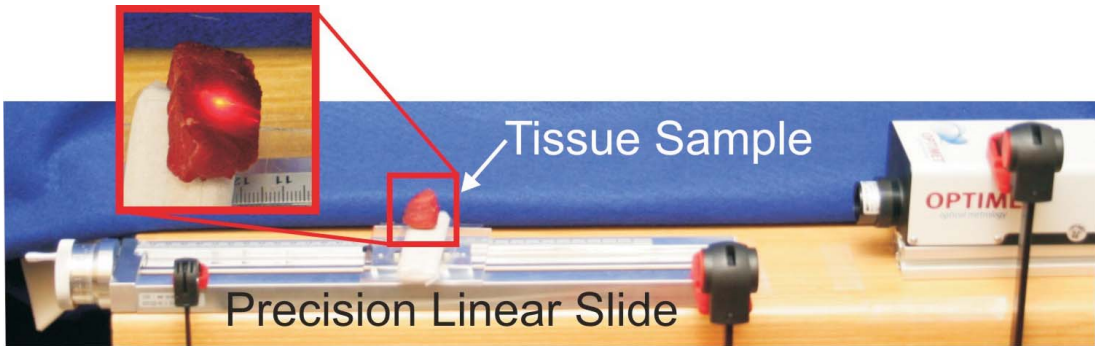

Figure 2.6: Baseline Conoprobe measurements were collected using a manually actuated precision linear slide. Tick marks on the actuation handle (visible at the left-hand end side of the slide) can resolve 10μm of linear sample motion. One full handle revolution produces 2mm of sample travel.

Other Components Used

Test samples were positioned using another A25 series UniSlide. An additional Velmex rotary table A5990T3 was used to rotate the mirror for the experiments that required mirror movement. The mirror used was a front surface rather than rear surface mirror, to eliminate the effects of optical refraction from mirror glass. The preoperative images used in the needle placement experiment were taken with standard clinical computed tomography at the Vanderbilt University Medical Center.

2.4 Conoprobe Repeatability and Accuracy

Before performing surface scans with the entire system described in Section 2.3, we experimentally validated the accuracy and repeatability for the Conoprobe itself when making measurements of ex vivo and phantom tissues. These experiments were designed to establish the baseline capabilities of the Conoprobe in order to provide context for the surface-scanning results described in Sections 2.6 and 2.7. We undertook

these experiments because the published specifications of the Conoprobe, discussed in Section 2.3, assume non-biological surfaces such as metal or plastic, rather than biological tissues which may absorb or diffuse laser light. Absorption could weaken the return signal and necessitate adjusting laser power or CCD sampling time. Diffusion could blur the fringe pattern, reducing measurement accuracy.

Our experimental setup for the experiments described in this section (Figure 2.6) consists of the Conoprobe, the linear slide, and various test samples. The axis of the slide was aligned with the Conoprobe laser, and both slide and Conoprobe were firmly clamped to the table to fix their relative positions. In both of the following sets of experiments, the following test samples were used: 1) a control sample of flat white paper (which provided a strong return signal with excellent signal-to-noise ratio, as reported by the Conoprobe), 2) ex vivo bovine liver, 3) ex vivo bovine muscle, and 4) ex vivo bovine liver with a topical surface preparation of talcum powder. This last sample was included because surface dusting is recommended by the manufacturer for less reflective surfaces. It was not motivated by any deficiency in measurements of untreated liver, but simply to provide a backup method for enhancing Conoprobe measurements if/when such enhancement is necessary in future studies with other types of biological tissues. Laser power and frequency were both experimentally adjusted to provide a signal close to 50% saturation (as reported by the Conoprobe manufacturer's software interface) for each tissue type, since this resulted in good accuracy. The resulting Conoprobe parameters are shown in Table 2.1.

Table 2.1: Experimental Conoprobe power levels (% of max power) and acquisition rates for various tissue types.

Tissue Type	Laser Power	Conoprobe Exposure
White Paper	31.25%	1000 Hz
Bovine Muscle	62.50%	400 Hz
Bovine Liver	62.50%	100 Hz
Liver with Surface Preparation	62.50%	1000 Hz

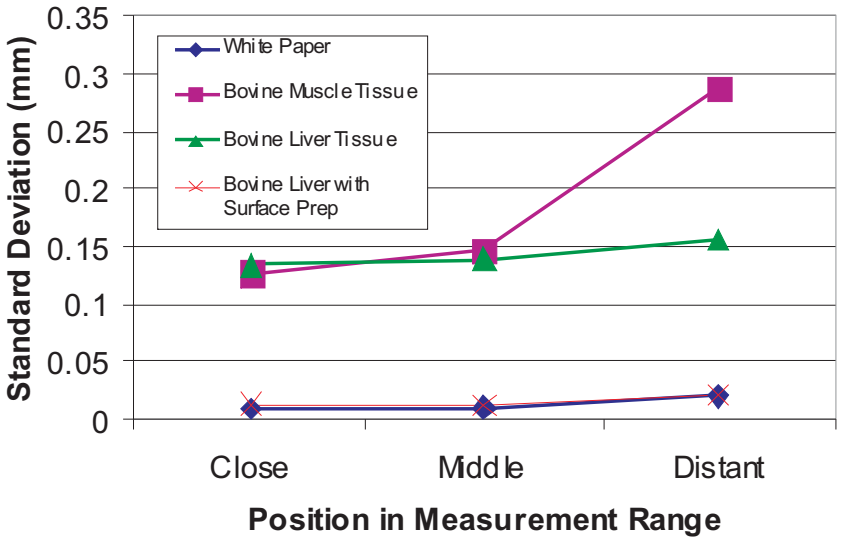

Figure 2.7: Standard deviations of repeated measurements taken with various tissue and control samples over the Conoprobe's measurement range. Each point represents the standard deviation of 10 repeated measurements taken at the beginning, middle, and end of the Conoprobe's measurement range.

2.4.1 Repeatability Experiment

In order to determine the repeatability of Conoprobe measurements, we collected distance measurements at three points: the beginning (∼160 mm from the Conoprobe), middle (∼240 mm), and end (∼330 mm) of the Conoprobe's measurement range. At each point, 10 measurements were recorded by momentarily interrupting and then reestablishing the Conoprobe's laser beam. Standard deviations of the measurements are shown in Figure 2.7.

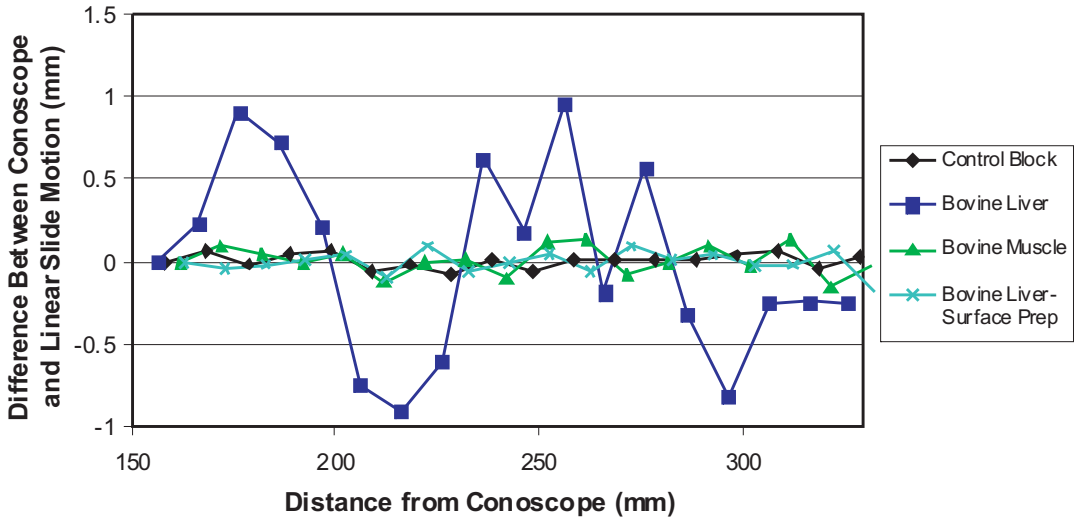

Figure 2.8: Experimental Conoprobe measurement error vs. distance for biological tissues. Each data point above shows the difference from 10 mm recorded by the Conoprobe when the sample was physically transported 10.00 mm.

2.4.2 Accuracy Experiment

We performed a second set of experiments aimed at assessing accuracy over the Conoprobe's measurement range. To do this, we began by recording an initial position near the minimum end of the measurement range, which we defined as a reference position for subsequent measurements. The linear slide was then used to move the sample in increments of 10.00 mm away from the Conoprobe until it reached the far end of the measurement range. For each increment, Conoprobe readings were used to compute distance traveled. The deviation of this distance increment from the actual increment of 10.00 mm is plotted in Figure 2.8.

2.4.3 Interpretation of Results: Repeatability and Accuracy

These results establish baseline precision and accuracy levels of the Conoprobe sensor itself, which are useful in interpreting the results of surface-scanning experiments

Figure 2.9: Experimental setup for mirror deflection experiments (Left) rotating mirror experiment, (Right) fixed mirror, translating sample experiment.

described in Section 2.6, and needle placement described in Section 2.7, since surface-scan errors contain both sensor noise and noise induced by optical tracking and coordinate frame conversions simultaneously. It is worthy to note that a surface treatment of talcum powder makes measurements nearly equivalent to white paper. Also, the shape of the error for untreated liver appeared to be repeatable, and compensation by calibration may be possible in the future, but this was not explored in detail in the context of these experiments.

2.5 Mirror Laser Deflection Experiments

Since it may be useful in some future systems (though not all) to automate laser aiming, we investigated the use of mirrors to deflect the Conoprobe's measurement direction. The use of either fixed or moving mirrors could allow measurements in areas that cannot be accessed via line of sight from outside the body. A front surface mirror was used for these experiments to ensure that no optical refraction took place inside the mirror. Two experiments were conducted: one with a fixed mirror and linearly moving target, and one with a fixed target and rotating mirror (see Figure 2.9). In

the latter experiment the Conoprobe measurement point traced out a line on the target.

The fixed mirror, moving target experiment was similar to the accuracy experiment described in the previous section, except that the Conoprobe and flat white paper target were oriented at right angles to each other with an angled mirror between them as shown in Figure 2.9 (Right). The target surface was then moved in 10.00 mm increments by the linear slide. Figure 2.10 shows a comparison of the actual distance traveled vs. the distance reported by the Conoprobe. The results of this experiment were similar to the results of the linear experiment with no mirror shown in Figure 2.8.

In a second path-deflection experiment, the flat white paper target and Conoprobe were both fixed at right angles with respect to each other. The mirror located at the base of the right angle was mounted to the rotary Velmex table, as shown in Figure 2.9 (Left). The distance to the mirror was recorded (the base distance). The mirror was then rotated to pan the measurement point across the surface of the target. The mirror angle and the Conoprobe-reported distance were recorded. Knowing the angle of deflection, length of the base distance, and the total distance, the location of the end of the laser in 2D space could be found. These points should form a line. To calculate the theoretical line the points should fit, the data was fitted to the equation of a line. The difference between the individual points and the line is shown in Figure 2.11.

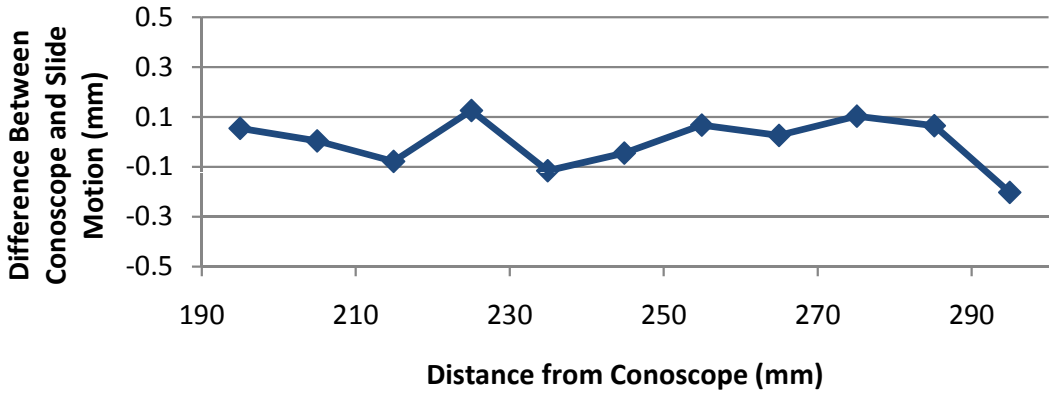

Figure 2.10: Experimental data for the fixed mirror, moving target experiment. Each data point above shows the difference from 10 mm recorded by the Conoprobe when the target was physically transported 10.00 mm. Comparing this data to the data shown in Figure 2.8 reveals no discernible measurement accuracy effects from using a mirror to aim the Conoprobe beam.

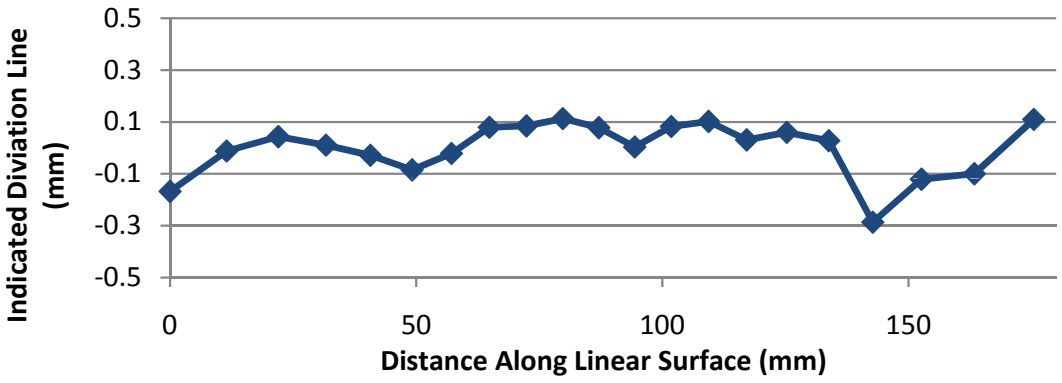

Figure 2.11: The deviation from a perfect line traced on the target plane as the mirror rotates, sweeping the Conoprobe measurement point across it.

2.6 Surface-Scanning Experiments

Using the experimental setup described in Section 2.3 (without the magnetic tracker), we conducted surface-scanning experiments for known parametric surfaces with a variety of surface properties, including biological tissues. During measurements the Conoprobe was held approximately 1 m in front of the optical tracker and 20–30 cm from the phantom along the axis of the laser. The beam was manually scanned over the surface of the phantom. Both spherical and flat objects with a variety of surface properties were scanned in this way, and the data fit to the known shapes of the objects scanned. Before presenting the data, we describe the calibration and fitting processes necessary for accurately reconstructing the surface point cloud.

2.6.1 Calibration

First, the position of each sensed point on the surface was expressed in the world (optical tracker) frame as,

$$ {}^{world}_{sensed}p = {}^{world}_{m}T \, {}^{m}_{c}T \, {}^{c}_{sensed}p, \tag{2.1} $$

where c denotes the Conoprobe lens frame and m denotes the fiducial marker frame. Here ${}^{c}_{sensed}p$ has zero y and z components and the Conoprobe reading as its x component. The transformation ${}^{world}_{m}T$ is given directly by the optical tracking system. The transformation between the Conoprobe measurement frame (located at its lens) and the fiducial marker frame on its surface, ${}^{m}_{c}T$, is unknown and must be determined by

calibration.

In contrast to rigid surgical tools where one might apply a pivot calibration, the distance to the point of interest here has no rigid physical structure attached to it. Thus we calibrated using several measurements along its axis returned by the Conoprobe. In this case, one might also consider applying a solution to the "Hand-Eye" calibration problem (e.g. the dual quaternion formulation of [23]), but in our case a simpler calibration procedure is possible, since we know that sensed measurements will always lie along a single axis in the sensor (Conoprobe lens) frame.

We performed this calibration by aiming the Conoprobe laser at a second fiducial marker that was not attached to the Conoprobe, the position of which (${}^{world}_{n}p$) was sensed by the optical tracking system. We repeated this for multiple Conoprobe poses. Then, parameterizing the rotation using Euler angles, we applied Matlab's `fminsearch` to minimize,

$$e = \sum_i a_i^{\mathrm{T}} a_i, \text{ where } \quad a_i = {}^{world}_{n}p - {}^{world}_{m,i}T \, {}^{m}_{c}T \, {}^{c}_{sensed,i}p \tag{2.2}$$

over the Euler angles and translation that compose the unknown transformation. The sum over $i \in \{1 \ldots n\}$ accounts for each of the n Conoprobe pose measurements made above.

2.6.2 Registration Algorithm

We conducted experiments with two parametric surfaces, a plane and a sphere. The algorithm for registering the known shape to the data was identical in both cases,

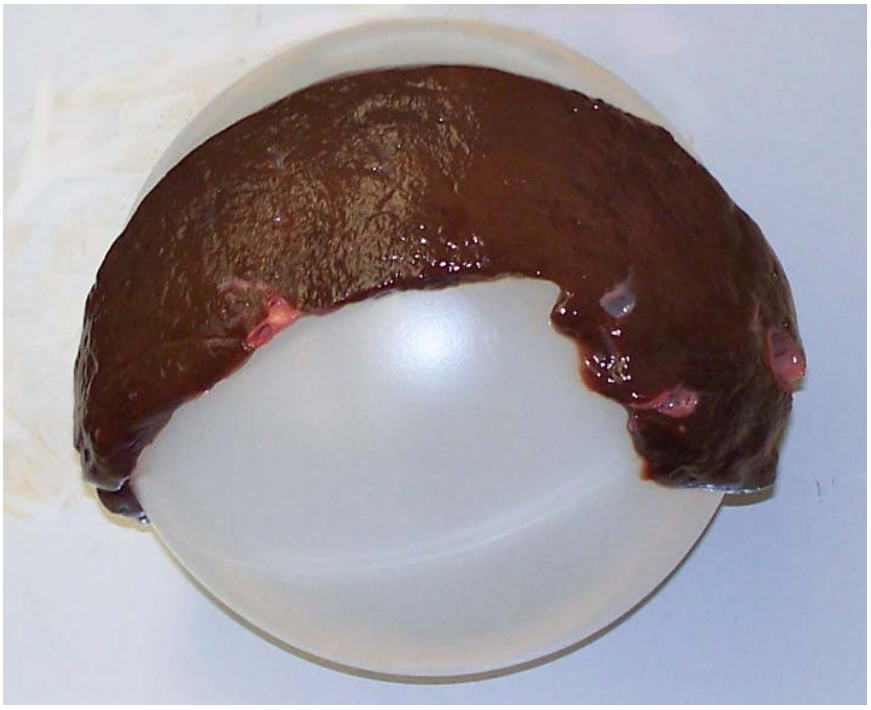

Figure 2.12: Liver tissue supported by spherical plastic ball creates a liver sphere.

except for the objective function. In both cases, we minimized the surface parameters over the distance between measured data and the known surface shape using Matlab's `fminsearch`. For the plane $ax + by + cz + d = 0$, we minimized the sum of the square of distances between the plane and each point,

$$e_{plane} = \sum_i \left(ax_i + by_i + cz_i + d\right)^2, \tag{2.3}$$

over the parameters of the plane, a, b, c, and d.

For the sphere $(x - x_c)^2 + (y - y_c)^2 + (z - z_c)^2 = r^2$, we minimized the sum of the square of the radial distances between the sphere and each point, namely,

$$e_{sphere} = \sum_i \left((x_i - x_c)^2 + (y_i - y_c)^2 + (z_i - z_c)^2 - r^2\right)^2, \tag{2.4}$$

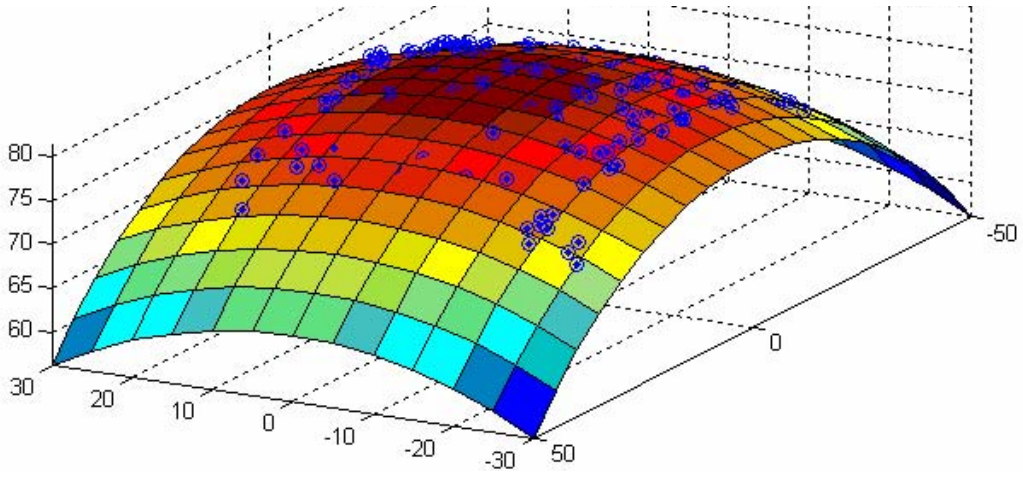

Figure 2.13: Liver sphere scan data with fitting parametric surface superimposed.

over the sphere parameters x_c, y_c, z_c, and r.

2.6.3 Parametric Surface Scans

Using the calibration and registration procedures outlined above, we scanned and fit two planes and two spheres. A control plane was created by attaching a piece of white paper to a flat metal surface. A tissue "plane" was created by laying a 5.4 mm thick slice of bovine liver flat on a piece of metal. A semi-translucent, polypropylene plastic sphere, as well as the "liver sphere" shown in Figure 2.12, were scanned as spherical shapes. The liver sphere was created in a manner similar to the flat liver phantom, namely by draping the same 5.4 mm slice of bovine liver over the plastic sphere.

We collected point clouds with the tracked Conoprobe system for each of these surfaces, and fitted the parametric surfaces to their corresponding clouds, as described previously in Section 2.6.2. Figure 2.13 shows the data returned from the Conoprobe scan of the liver sphere, together with a section of the parametric sphere fit to the point cloud. The results of all parametric scan experiments are summarized on Table 2.2.

Table 2.2: Experimental data for parametric surface scans.

	Plane	Liver Plane	Sphere	Liver Sphere
# points	800	400	400	400
Surface	White Paper	Liver	Plastic	Liver
Radius	—	—	75.0 mm	80.4 mm
Fit Radius	—	—	74.3 mm	81.0 mm
Std. Dev.	0.24 mm	1.22 mm	0.47 mm	0.61 mm

Note that fitted radii and plane parameters are very near known actual values, and standard deviations are low – even when the sphere is covered with ex vivo liver tissue.

2.6.4 Accuracy Experiments: NDI Polaris Tracker

The initial system experiments were conducted using the previously described Micron Tracker as the optical tracking part of the system. The system was subsequently tested while paired with an NDI Polaris Spectra tracking system (NDI, Ontario, Canada). With an upgraded optical tracking system, the accuracy of the system was shown to be comparable with an LRS tracked with the same Polaris Spectra. The results showed that the Conoprobe-based system showed RMS error in localization of less than 1 mm. Surface registration showed mean closest point error of less than 1 mm. Thus, the goal of creating a system with accuracy Equivalent to the existing LRS system was demonstrated [15]. A subsequent study by the same research lab found the Conoprobe-based system to produce better results than the LRS [92].

2.7 Needle Placement Experiment

Having verified the Conoprobe's ability to record known shapes, a pair of experiments were conducted to demonstrate the entire envisioned surgical workflow, from the surgeon's selection of desired targets on medical images, to use of the Conoprobe in registration, to final positioning of a needle tip at the desired location(s) specified by the surgeon. These experiments approximate the steps that might be taken to insert a biopsy needle or an ablation probe via a needle into a liver or other soft tissue organ. Final tip accuracy is assessed using the magnetic tracker, which would not be an intrinsic part of a final scanning system. It acts only as an exogenous measurement device to verify results.

2.7.1 Needle Experiment Setup

The experimental setup for this experiment is as shown in Figure 2.3. The Conoprobe with attached fiducials was as described in Section 2.6. The power and frequency were 70% and 300hz, respectively, selected as discussed in Section 2.4. The origin of the optical coordinate frame is located in the center of the Micron Tracker.

The Aurora magnetic tracker was used as an external measurement system to identify the location and orientation of the target and needle tip (both were equipped with embedded magnetic tracking coils). The needle to be placed was a 13 gauge beveled tip needle with an attached optical fiducial marker near the base. The optical fiducial was used for all targeting in the experiment. The target was a second magnetic tracking coil encased in a plastic catheter. The target could be inserted into a variety

of locations within the phantom liver through small channels created during the molding process. The phantom was a cast silicone rubber replica of a human liver (see Figure 2.14).

The location of the needle tip with respect to the optical fiducial was established using a pivot calibration. For the magnetic tracking coil in the needle tip, the 1.5 mm difference between the location of the coil and needle tip was compensated for in the measurements. The magnetic field generator was placed approximately 20 cm from the liver phantom in the positions shown in Figures 2.3 and 2.15. The origin of the magnetic coordinate frame is the center of the field generator. To hold the needle steady during alignment and insertion, a Civco Ultra-Pro II 13 g ultrasound needle guide was attached to an arm, as shown in Figure 2.3.

2.7.2 CT Scan and Segmentation

Prior to the experiment the liver phantom was scanned using the CT scanner with a voxel size of 0.729 mm $\times$ 0.729 mm $\times$ 2 mm slice thickness. Segmentation was performed with a level-set segmentation technique using Analyze 9.0 software (Mayo Clinic, Rochester, MN). A point cloud was extracted from the segmented data using the marching cubes algorithm [58] contained within Kitware's Visualization Toolkit (VTK, Kitware Inc, www.vtk.org). The extracted surface was then smoothed by fitting radial basis functions using the FastRBF toolkit published by Farfield Technology (Christchurch, New Zealand) [17,18]. This surface was then manually trimmed resulting in a point cloud representing only the upper surface of the liver in the CT coordinate frame.

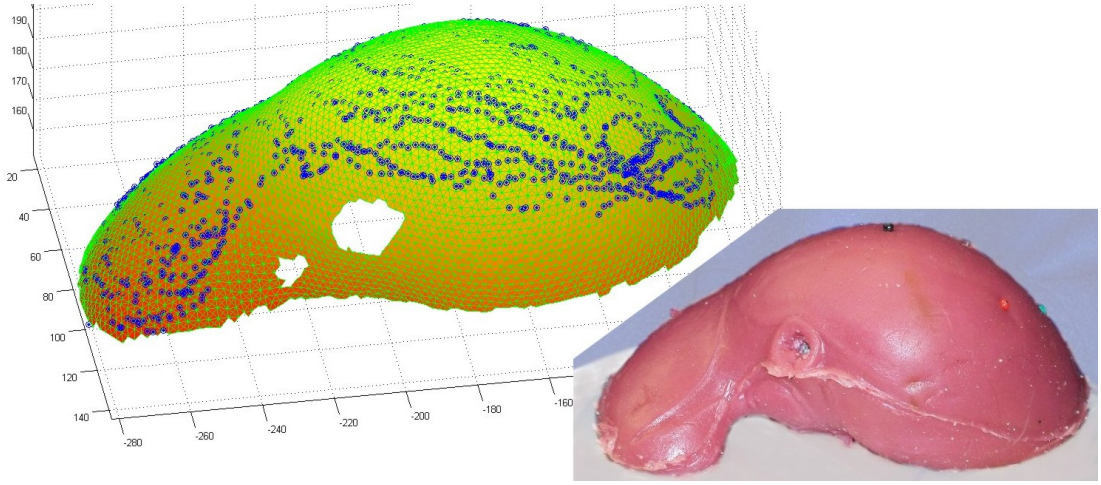

Figure 2.14: Scanned Conoprobe points displayed on meshed phantom surface taken from a CT scan. An ICP algorithm was used to register the data sets.

2.7.3 Registration

To register the Conoprobe data to the segmented CT scan of the phantom liver, we used the Iterative Closest Point (ICP) algorithm. ICP requires an initial guess of the transformation between the optical coordinate frame (in which the Conoprobe point cloud is represented) and the CT coordinate frame (in which the segmented liver data is represented). To establish this initial guess, we placed four stainless steel needles with colored plastic heads into the phantom prior to CT scanning, and used these to perform a quick rough rigid point registration [26,87] with which to initialize the ICP algorithm. Note that in an eventual clinical implementation, this initial guess could be generated from knowledge of the locations of the optical and magnetic coordinate frames, or through a quick trial-and-error procedure, or the ICP could be simultaneously initialized from several locations with computations run in parallel, and the result with the lowest residual error selected as the registration result.

2.7.4 Obtaining Input Target Locations in CT Space

In an eventual clinical implementation, target points would be identified by the physician by, for example, clicking on desired locations on medical images shown on a computer screen. Because the target coil needed to be repositionable to allow multiple target locations, it was not sufficient to simply determine target coil location in CT space by observing it in the CT image. This would have required many coils, which would have been expensive and caused artifacts in the CT image.

The test used an alternate method for determining the coordinates of the magnetic tracking target in CT space, based on magnetic surface registration. A magnetic tracking coil was lightly swabbed over the liver surface and a point cloud recorded. This was then registered to CT space using ICP, and the resulting transformation was used to project the location of the target magnetic coil into CT space to simulate a physician input target in image coordinates. It is also noted that this magnetic ICP would not be required in an eventual clinical implementation.

2.7.5 Conoprobe Scan and CT Registration

The Conoprobe system was used to collect a cloud of points on the liver surface in optical space. The point cloud was then registered to the CT surface data using the ICP algorithm. Using the resulting transformation, the location of the target point could be known in both CT and optical space.

2.7.6 Needle Insertion

The insertion procedure for the needle was similar to the procedure used in biopsy with the Medtronic Navigus system (Medtronic, Minneapolis, MN). Using a needle guide, the needle is aligned such that it targets the desired final location. In this case the needle was considered on target if the projected needle trajectory passed within 0.5 mm of the target. The needle guide can be seen in Figure 2.3. The needle was then inserted through the needle guide until its tip reached the depth of the target as nearly as possible (always within 0.75 mm). Here, in contrast to the following subsection, re-aiming during insertion was not possible. While a robot can offer higher accuracy [13], manual positioning using a passive, lockable positioning arm is a simpler solution for initial clinical implementation and can be made less expensive.

2.7.7 Results: Needle Placement

The results of five needle insertions to five different targets are summarized in Table 2.7.7. Total Error represents the distance reported by the magnetic tracker between the final needle tip location and the final target location after insertion. This includes all sources of error including surface registration error, tissue deformation, initial needle misalignment, needle deflection, etc. The Tip-Magnetic Target distance is the difference between the final needle tip location reported by the magnetic tracker, and the initial target in magnetic coordinates. This includes all sources of error except for target motion due to tissue deformation. The Tip-Optical Target error represents the distance between the optical target location as reported in optical

Table 2.3: Results of 5 needle placement trials

Trial	**Total Error**	Tip–Mag. Target	Tip-Opt. Target	Tip Opt.–Mag.	Target Shift
	mm	mm	mm	mm	mm
1	**3.2**	2.1	1.2	2.8	2.0
2	**2.5**	2.4	1.8	2.8	0.4
3	**3.1**	2.4	1.3	2.5	1.0
4	**2.2**	2.9	0.7	2.6	1.1
5	**3.7**	1.9	1.2	2.4	2.0
Average	**2.94**	2.34	1.24	2.62	1.30

space and the tip of the needle as reported by the optical tracker. This measurement can be considered a best-case system error, as it includes the error associated with manual aiming of the needle only and does not include any surface registration effects. The Tip Optical-Magnetic error indicates the difference in optically and magnetically reported final needle tip location. This measurement gives an indication of needle deflection during insertion, and contains the effects of both surface registrations. Finally, the target shift indicates the distance that the magnetic target moved during insertion due to tissue deformation, as reported by the magnetic tracker.

2.7.8 Discussion of Needle Placement Results

Overall the results of the needle placement experiment showed the viability of the basic system concept. The results of the Conoprobe registration and needle placement experiment can be compared with those obtained by Cash et al. using LRS for liver registration [19]. In the LRS experiments, the quality of an LRS registration was

evaluated by two metrics, the mean residual error of the scan points to the preoperative data set after ICP, and via Target Registration Error (TRE). TRE is defined as the difference between the reported location of a target and the actual location of the target [12]. Cash et al. report a mean residual error of 0.75 mm and a TRE of 2.0 mm for their LRS system. The mean residual error of our experiment was 1.17 mm, and the mean TRE was 2.34 mm based on Tip-Magnetic Target measurements.

Since the mean residual error of the test system is comparable to that found by Cash et al., it is believed that the Conoprobe measurement error is essentially Gaussian in nature, and thus does not significantly affect the quality of the ICP fit. Furthermore it is noted that while Tip-Magnetic Target is the best approximation of TRE available in this experiment, it does include the effects of both Conoprobe and magnetic ICP registrations, as well as any physical targeting error of the needle associated with manual alignment or needle bending. It is interesting to note that even with these additional sources of error the results are still comparable to the prior LRS scan results reported by Cash et al. This indicates that Conoprobe surface scans should be able to achieve the goal of enabling minimally invasive surface scans of comparable quality to existing LRS systems.

2.8 Cannula Placement Experiment

The steerable cannula (first mentioned in Section 2.3) has several advantages over the traditional needle placed in the previous set of experiments. The cannula can be guided around obstacles which would prohibit reaching a target location with a traditional strait needle. The cannula can also reach multiple locations inside an

organ without requiring multiple entry points. However, unlike a traditional needle, the curved path of a steerable cannula can be harder for a surgeon to mentally project in the workspace. For this reason it is natural to use steerable cannulas in conjunction with a trajectory planned in preoperative imaging. The steerable cannula is then deployed with computer assistance after being registered to the surgical workspace.

This set of experiments is similar in setup and procedure to the previously described needle placements (Section 2.7). One difference is that the manually targeted and advanced needle is now replaced with a steerable cannula with a manual actuation unit. The liver phantom and base of the cannula actuator will not be moved with respect to one another throughout the experiment. Thus, the experiment will simulate a case where a steerable needle actuation unit is registered to an organ and then deploys the steerable needle to target multiple locations within the organ though a single organ entry point.

2.8.1 Experimental Setup

The experimental setup for this experiment is as shown in Figure 2.15. The Conoprobe with attached fiducials was unchanged from the needle experiment. The needle of the previous experiment was used to provide a target location for the cannula.

The procedure to register the liver phantom and its CT scan into optical tracker space and magnetic tracker space is the same as before. Point clouds covering the top surface of the liver phantom were collected using the Conoprobe-based surface scanner and via swabbing a magnetically tracked probe. Both point clouds were registered to the surface extracted from the CT scan of the phantom. The Aurora magnetic tracker

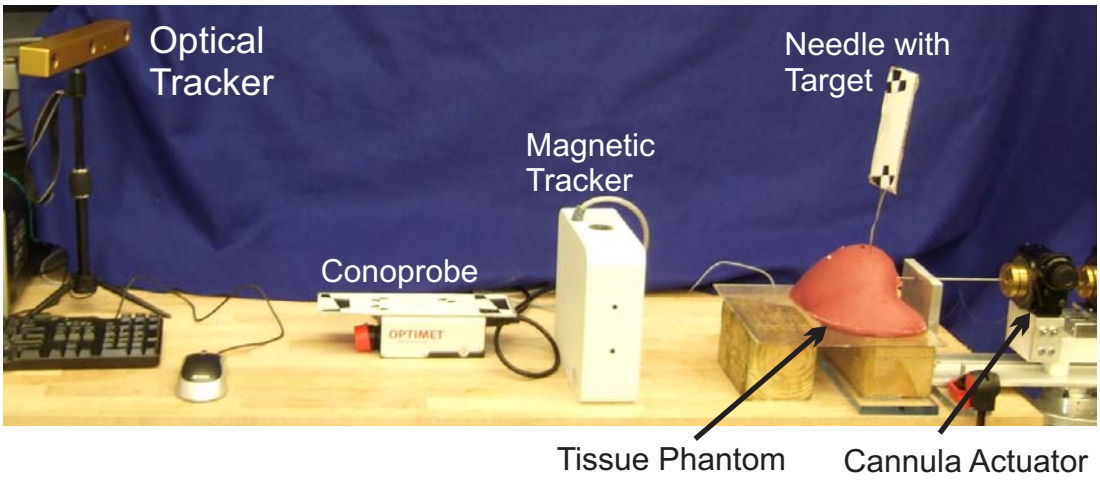

Figure 2.15: Experimental setup for surface scanning and placement of a steerable cannula deployed needle.

was again used as an external measurement system to identify the location target and cannula tip (both were equipped with embedded magnetic tracking coils). The registration of the steerable cannula base frame into optical space will be described in Section 2.8.2. The registrations of various coordinate frames in the experiment are illustrated in Figure 2.16.

2.8.2 Steerable Cannula Mechanics and Kinematics

While steerable cannulas can be made from larger numbers of tubes, the cannula used in this study is composed of two concentric tubes (see Figure 2.17). The outer tube is made of stainless steel and is straight. The inner tube is curved, and made from superelastic nitinol. The arc length of the curved portion is 54 mm long, with an approximately constant radius of curvature of 79.4 mm. The material and geometric properties of the two tubes are summarized in Table 2.4.

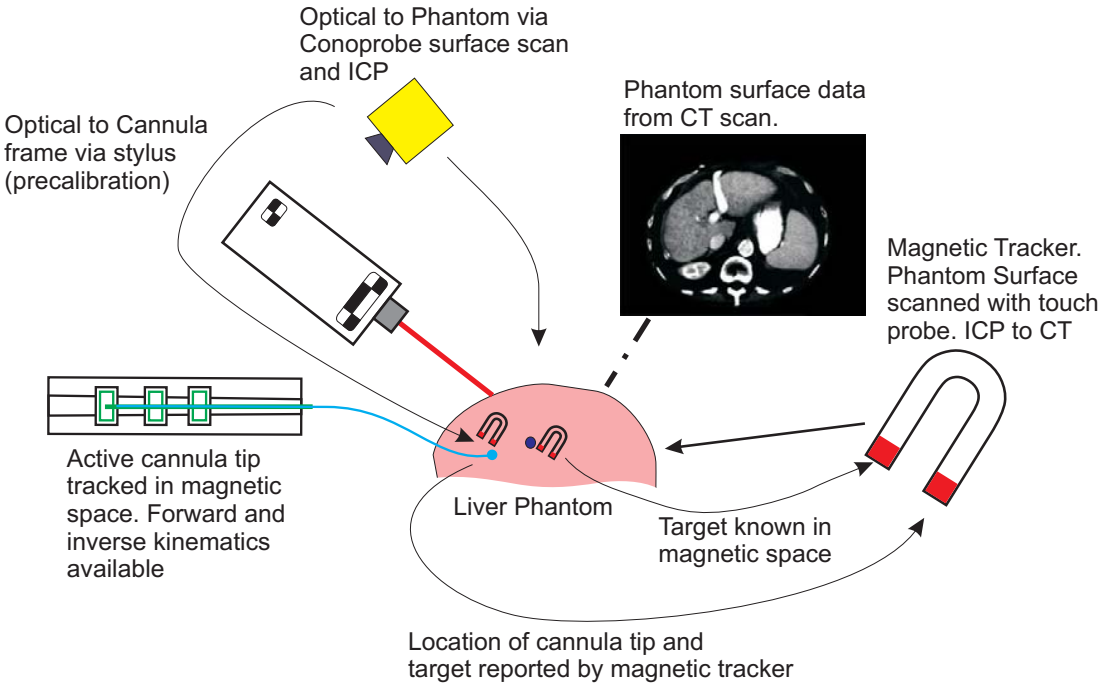

Figure 2.16: Schematic of the registrations in the system. The magnetic target (tracking coil in the needle tip) is known in magnetic space. The cannula base frame is located in optical space via an optically tracked touch stylus and a calibration procedure. During an insertion experiment, the cannula tip is tracked in magnetic space via an embedded coil in the tip and calculated in optical space cannula base frame via forward kinematics. A magnetic touch probe is used to swab the surface of the phantom to enable an ICP registration with the CT scan. A second surface scan with the Conoprobe-based scanner allows registration of the CT space to the optical space.

Cannula Mechanics

Since the outer tube is always straight, there will be no torsional "wind-up" of the tubes in the curved or straight sections, other than minor frictional effects. Therefore, this prototype cannula will consist of a straight section followed by a slightly curved section (where the curved section of the inner tube bends the straight outer tube), followed by the curved portion of the inner tube alone after it exits the outer (See Figure 2.18). The plane in which the curved sections lie is controlled by the angular rotation of the tube bases, α, and the length of each section is controlled by the translation of each tube's base. This cannula therefore has 3 degrees of actuation freedom (since axial rotation of the outer straight tube has no effect on shape). Using the Bernoulli-Euler beam-mechanics model of [107], the curvature of a section of the cannula where the curved portion of the inner tube overlaps the outer tube can be expressed as a weighted average curvature, weighted by the individual tube bending

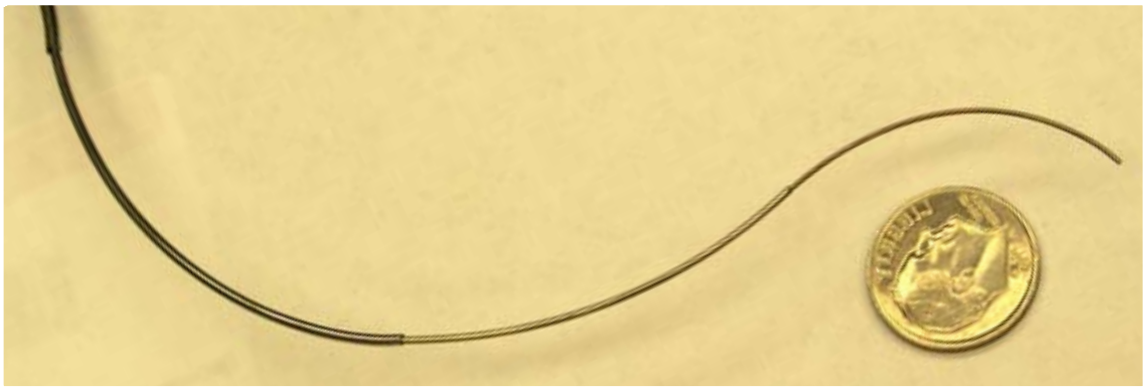

Figure 2.17: A prototype steerable cannula made of four superelastic nitinol tubes and one central wire (with three tubes and the wire visible).

stiffnesses,

$$\kappa_{eq} = \frac{\kappa_1 E_1 I_1 + \kappa_2 E_2 I_2}{E_1 I_1 + E_2 I_2}, \tag{2.5}$$

where E_i and I_i are the elastic modulus and moment of inertia of tube i, respectively.

Cannula Kinematics

A diagram with the kinematic variables labelled is shown in Figure 2.18. Due to clearance between the tubes, the inner tube comes out of the outer tube at a slight angle, which is denoted as θ. Prior models have not accounted for this non-tangency of arcs, but it is included here. The angular offset is experimentally measured (with respect to the tangent at the tip of the outer tube) using graph paper, and its effect is included as an additional transformation in our kinematic model.

The forward kinematic model consists of a series of transformations,

$$g_{tip} = g_{base} e^{\widehat{\xi_\alpha}} e^{\widehat{\xi_1}} e^{\widehat{\xi_2}} e^{\widehat{\xi_\theta}} e^{\widehat{\xi_3}} \tag{2.6}$$

each defined by a constant kinematic twist ξ_j (see [67] for a thorough review of this

Table 2.4: Measured and Assumed Physical Quantities for Experimental Cannula Tubes.

	Outer Tube (1)	Inner Tube (2)
Young's Modulus: E(GPa)	190	58
Inner Diameter: r_i(mm)	1.52	.96
Outer Diameter: r_o(mm)	1.82	1.26
Straight Length: L_s(mm)	171	255.7
Curved Length: L_c(mm)	0	54
Total Length: L(mm)	171	309.7
Curvature: κ(1/mm)	0	0.0126

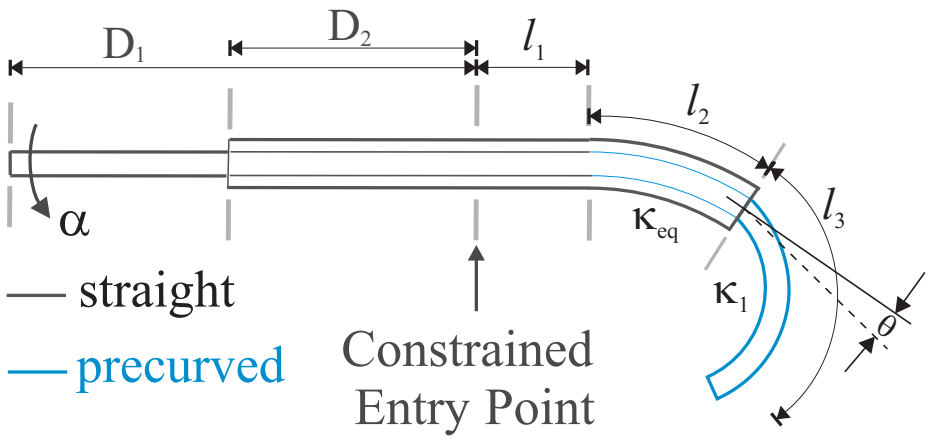

Figure 2.18: Diagram of the two tube cannula showing kinematic variables.

notation), where the twists are given by

$$\begin{aligned}
\xi_\alpha &= [0 \;\; 0 \;\; 0 \;\; 0 \;\; 0 \;\; \alpha]^T \\
\xi_1 &= [0 \;\; 0 \;\; \ell_1 \;\; 0 \;\; 0 \;\; 0]^T \\
\xi_2 &= [0 \;\; 0 \;\; \ell_2 \;\; \kappa_{eq}\ell_2 \;\; 0 \;\; 0]^T \\
\xi_\theta &= [0 \;\; 0 \;\; 0 \;\; \theta \;\; 0 \;\; 0]^T \\
\xi_2 &= [0 \;\; 0 \;\; \ell_3 \;\; \kappa_1\ell_3 \;\; 0 \;\; 0]^T
\end{aligned} \tag{2.7}$$

and the link lengths are given by

$$\begin{aligned}
\ell_1 &= L_{s2} - D_2 \\
\ell_2 &= L_1 - L_{s2} + D_2 \\
\ell_3 &= L_2 - D_2 - L_1 + D1
\end{aligned} \tag{2.8}$$

where D_1 and D_2 are the translational kinematic inputs as shown in Figure 2.18.

Cannula Inverse Kinematics

We computed inverse kinematics for the cannula using a nonlinear root finding algorithm, Matlab's `fsolve` function. The objective function was the difference in (2.6) evaluated at a known starting configuration and the desired tip position, namely,

$$||p_{tip}(\alpha, D_1, D_2) - p_{tip,desired}|| = 0, \tag{2.9}$$

To ensure that the root finding algorithm finds a feasible solution that can be accomplished on the cannula actuation unit, additional error terms were added to the error term which are zero in feasible actuator configurations and ramp functions of the actuator variables preventing cases where desired actuator positions would result in physical actuator collisions.

Steerable Cannula to Optical Registration

The cannula base frame, the kinematic origin of the cannula, was registered to optical space via a point based registration [7]. The cannula was positioned in 27 locations representing points near the beginning, middle and end of each actuator range. As described in section 2.8.2 the outer tube rotary state does not affect the position of the cannula tip. This results in 3 independent actuators with 3 positions each for 27 total positions. The location of the cannula tip was recorded via an optically tracked stylus. Because the stylus and cannula tip can not occupy the same physical space the stylus's position was recorded twice, once on either side of the cannula for each

pose, and the midpoint of the two readings was taken as the experimental tip point. The 27 points are registered to the expected position of the cannula as calculated by the forward kinematics using point cloud registration. This method resulted in a fiducial registration error of 1.82 mm, and was performed in free space, without the liver phantom present.

2.8.3 Cannula Needle Insertion

As with the needle experiments the location of the target is transformed from magnetic space to optical space via the common registration to CT space and then into the cannula actuator space. With the location of the target now in the frame of the cannula, inverse kinematics was used to solve for the joint positions required to reach the target.

The cannula was then advanced into the liver phantom. In order for the cannula to deploy along its own arc, the rotary stages were adjusted first, and then the cannula was linearly deployed, beginning with the outer tube. After insertion, the magnetic tracker was used to record tip and new target position (since the target may have shifted somewhat due to tissue deformation).

2.8.4 Results: Cannula Needle Placement

Experimental results for all 10 insertion experiments are reported in Table 2.5. The average difference between the cannula tip and target was 6.53 mm with a range of 5.42 to 8.87 mm. The difference between the reported final location and targeted location averaged 8.32 mm with a range of 5.53 to 13.49 mm.

Two of the performance metrics described in Section 2.7.7 do not apply to the steerable cannula experiments. Tip-Optical Target error describes an error due to the inability to perfectly aim the conventional needle at the target point prior to insertion and the inability to advance to an exact depth. Both issues are related to the method of hand aiming and advancing used in the needle placement experiment. Tip Optical-Magnetic error related the error due to bending of the traditional needle during insertion. Flexure of the needle results in movement of the needle tip relative to the base and optical tracking marker.

Tip-Optical Target error does not apply to the steerable cannula. Once the cannula actuation unit was registered in optical space it was never moved. For the purposes of this experiment it is assumed the forward kinematics of the steerable cannula and the registration of the cannula actuation unit to optical space were perfect. This assumption implies that there is no error between the desired location targeted in optical space and the final cannula tip location in optical space. Thus the Tip-Optical Target described in Section 2.7.7 would be zero in all cases.

The Tip Optical-Magnetic error assumes deflection of the steerable cannula from its kinematically defined shape. As with the assumption of perfect registration, it was assumed that the steerable cannula was not deflected by the phantom tissue during actuation.

It is acknowledged that both of the previously mentioned assumptions are simplicitations. Any level of error in the kinematic model, registration of actuation unit to optical space and deflection of the cannula during insertion would contribute to the total error reported in Section 2.8.5 and would not represent error due to the surface

Table 2.5: Results of 10 cannula placement trials

Trial	***Cannula to Target (mm)***	*Cannula to Original Target (mm)*	*Target Shift During Test (mm)*
1	**5.42**	4.21	7.99
2	**6.58**	3.71	8.43
3	**5.85**	6.68	5.53
4	**8.87**	5.39	10.07
5	**5.79**	5.35	6.96
6	**6.46**	6.27	7.06
7	**8.14**	3.20	9.41
8	**5.57**	4.43	7.10
9	**6.90**	1.91	7.21
10	**5.76**	9.20	13.49

scanning system.

2.8.5 Discussion of Cannula Results

Overall the results of the needle placement experiment showed the viability of the basic system concept. The steerable cannula placement experiment was less accurate though the largest contributors of error were believed to be errors not associated with registration.

The cannula-based experiment produced accuracies within 5-7 mm range. Such accuracies might potentially be suitable for some medical procedures, depending on the location and size of the tumor and the particulars of the ablator used. For example, liver ablation may be accomplished with this level of accuracy. However, it is likely that significantly higher accuracies can be achieved with a system similar to the one used in the cannula test. The sources of error are discussed below along with a perspective on what may be reduced, the accuracy improvement that can be expected, and how this might be accomplished in future work.

Magnetic Tracking

The registration between magnetic space and other coordinate systems is believed to be the largest source of error in the cannula experiment. The contact-based surface scan used may have deformed the surface slightly, affecting the results of the ICP fitting procedure. Furthermore, some unmodeled field distortion may have been present due to our metallic actuation unit. A field distortion would have warped the point could used for the ICP registration. Note that since the target and cannula coil are both subject to the same field distortion if any distortion were present it would affect both approximately equally. Furthermore, note that this magnetic tracking issue will not be a problem for practical implementation – magnetic tracking was simply a method of external data collection in the benchtop studies.

Optical Tracking

The Conoprobe and optical stylus are subject to optical tracking noise. This noise comes from small changes in the reported position and orientation of the optical fiducials resulting from the 0.20 mm RMS sensor noise in individual markers. The rotational portion of this is amplified by the distance from the optical fiducial to the point of interest, either the stylus tip or the laser dot. By collecting 200 measurements of the needle and Conoprobe while each was held in a stationary pose it was determined that the standard deviation of the absolute stylus position error was 0.169 mm, while the standard deviation Conoprobe measurement noise at 240 mm was 0.159 mm. These can be reduced by using larger or alternate arrangements of

fiducial markers.

ICP Fitting

The magnetic and optical spaces were registered to each other via a common registration to the segmented CT surface. Note that the segmentation process itself introduces some error. To assess the accuracy of the ICP fit qualitatively, one can plot it on the surface, as shown in Figure 2.14. One ICP fit (Conoprobe measurements to CT data) is intrinsic to the procedure and must be retained in an eventual clinical system. However, prior surface registration results using other methods of surface scanning indicate that this will not be prohibitive.

Cannula Modeling Enhancements

In this experiment a simple cannula and a simple model of that cannula were used. More advanced models that do not assume circular curvature (instead using direct measurements of actual tube curve) exist [84], and the latest models can even account for external loading on the cannula [83]. By employing these methods one might expect to reduce registration error of the cannula base frame, potentially increasing accuracy by several millimeters (depending on how well externally applied forces can be determined).

Cannula and Tissue Deformation

The flexible cannula is subject to deformation as it is inserted into the phantom tissue, and the tissue also deforms. The effect on the cannula can be minimized by using

larger and stiffer tubes, or by use of the more advanced kinematic models mentioned above. Tissue deformation can be modeled using finite element methods (see e.g. [6]), which would lead to accuracy enhancements.

2.9 Conclusions and Future Work

These experiments established the initial feasibility of creating a minimally invasive surface scanner for soft tissue registration using low cost, off-the-shelf hardware. A scanning system based on conoscopic holography promises the ability to scan through a laparoscopic port without requiring wide exposure of the organ of interest. The facts that conoscopic holography is a proven technique for high precision distance measurements, is readily available commercially in inexpensive packages (approximately $5,000 for the Conoprobe base unit), and can deliver high-quality distance measurements to biological tissues make it a compelling technology for laparoscopic surface scanning.

Additional beneficial features of this scanning method include the fact that, in contrast to LRS, it does not collect unwanted data points and that the physician can directly specify intraoperatively which surfaces to scan. One challenge of deploying LRS is that one must trim many points from the data set, because it will collect surface data on the entire intraoperative field, rather than just the organ of interest. Because the Conoprobe is manually aimed, the surgeon can ensure that it captures only the area of interest. Furthermore, the system's ability to selectively scan individual anatomical features (e.g. ridges or lobes of the liver, etc.) makes it an ideal candidate for use with registration methods such as that proposed by Clements et

Figure 2.19: First prototype of a laparoscopic tube attached to the Conoprobe. A small CCD camera is attached to the tip of the tube, enabling the physician to view the position of the laser measurement spot on a hand-held display screen. The inset image in the lower left shows the display screen and the tip of the tube seen end-on. This first prototype illustrates the basic concept but is not yet airtight.

al. which use selected surface patches or features to improve ICP registration and eliminate the need for an initial alignment guess [22].

Subsequent to the success of these experiments, the Conoprobe-based surface scanner has been used in several additional experiments further exploring the accuracy of the system and finally using the system as a component of an overall image-guidance system. First and second generation laparoscopic trocar-compatible housings have been created. The first, shown in Figure 2.19 was meant to demonstrate the possibility of scanning through a single port with a distal camera installed at the end of the sensor assembly. The second generation laparoscopic trocar-compatible assembly was functional and used in an animal study [15]. The assembly included provisions for sterility control and is shown in Figure 2.20.

With an upgraded optical tracking system, an NDI Polaris Spectra in place of the Micron Tracker, the accuracy of the system was shown to be comparable to a LRS tracked with the same Polaris Spectra [92]. The results showed that the Conoprobe-based system exhibited an RMS error in localization of less than 1 mm.

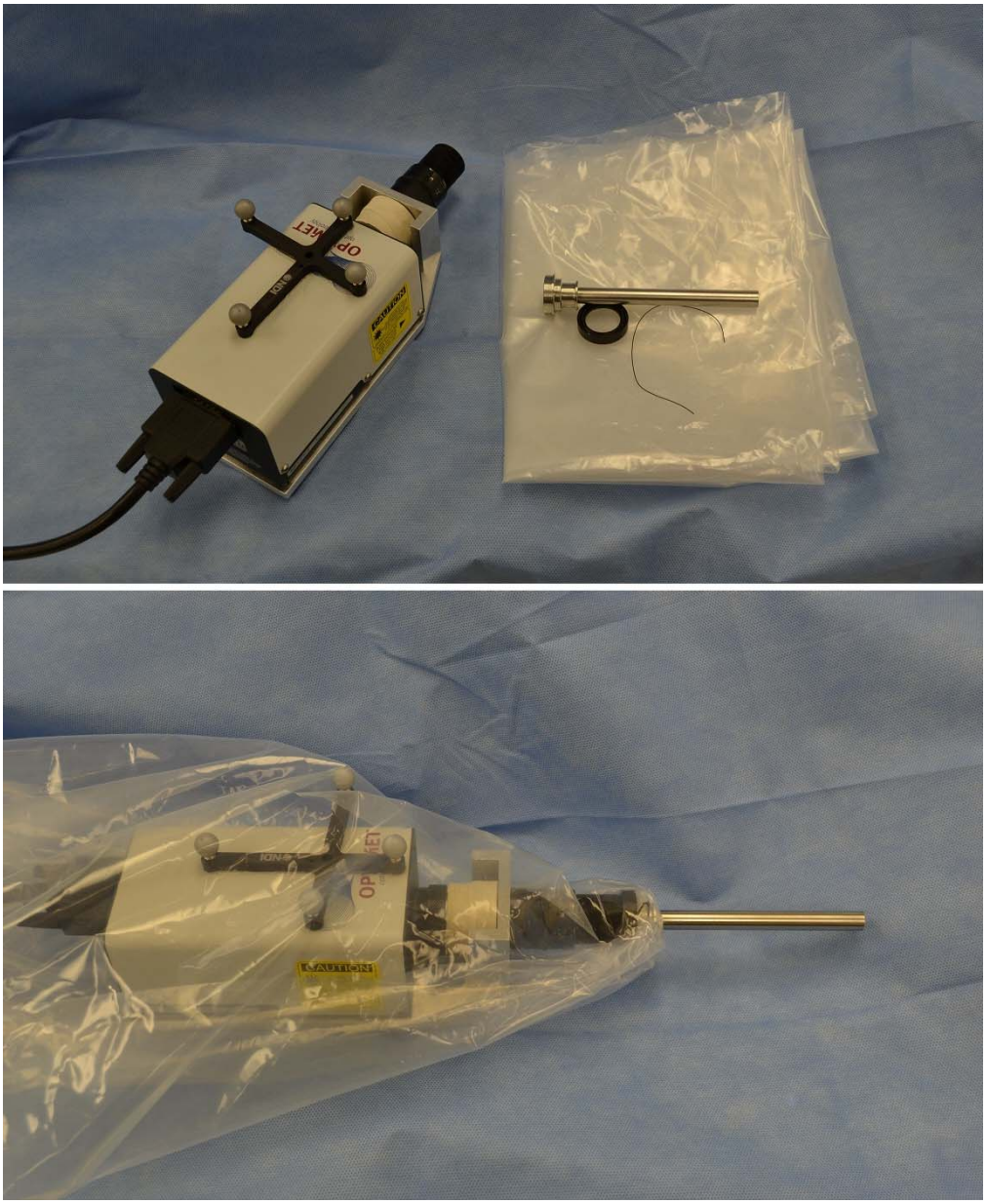

Figure 2.20: Functional prototype of the Conoprobe mounted to frame and endoscopic tube assembly. The sterile portion of the system is shown to the right in the top image. An NDI Polaris optical tracking marker is attached to the unit. During the bagging procedure, the sterile bag and endoscopic tube are attached to one another. The bag is inverted over the tube and then attached to the front of the Conoprobe assembly. Finally the bag is reversed over the non-sterile part of the assembly thus isolating the sterile field from the Conoprobe.

Surface registration showed mean closest point error of less than 1 mm. Thus, the goal of creating a system with accuracy equivalent to the existing LRS system was demonstrated [15]. A subsequent study by Simpson et al. found the Conoprobe-based system to produce better registration results than physical touch probes or LRS [92]. Finally, the system has been used to collect data in the operating room in conjunction with research characterizing the shape of the cavity left in the brain during resection [91].

The goal of this research was to produce a low cost, yet accurate, surface scanner using primarily off-the-shelf hardware. The resulting Conoprobe-based scanner has accuracy better than established scanners currently used in surgery. A means of sterile use has been illustrated and the system has been used for data acquisition in the operating room. The initial objectives of this research have been accomplished. Such a system can enable the benefits of surgical navigation with preoperative images. When paired with the dexterous manual tools discussed in subsequent chapters of this dissertation, this scanner offers a foundational component of dexterous, image-guided surgery system that does not require automation.

Chapter 3

Natural User Interfaces for Manual Articulated Laparoscopic Tools

One of the often cited advantages of the da Vinci Surgical System is the dexterity offered by the system's EndoWrist tools and the "naturalness" of the user interface used to control them. Naturalness in this context is the ability of a surgeon to sit down at the control console for the first time and almost immediately understand how to operate the remote instruments.

The high dexterity and natural user interface of the system are the result of commanding wristed laparoscopic tools, the EndoWrist tools (Figure 3.1), with multi-DOF "joystick-like" controllers. The movements made by the surgeon's hands on the controls are followed by the robotically controlled tools. The distal wrists at the end of the tools offer a full six degrees of freedom (DOF) vs. the four typical of manual laparoscopic tools (Figure 3.2). The system designers chose what is perhaps the most natural choice for master-slave control of a hand-like end effector, a simple 1:1 mapping (plus scaling of the linear displacements) of the operator's hand to that of the robot [35]. Due in part to the increased dexterity of the EndoWrist, the da Vinci system use has grown to dominate radical prostatectomy surgical procedures [97]. The system can also be considered a gold standard for natural interface performance.

While the da Vinci's mapping between the surgeon's hands and the tool movements is the current gold standard, the system has significant limitations. The da Vinci system is large, making it difficult for the system to work in collaboration with traditional surgical staff. Significant time is needed to position and engage the robot

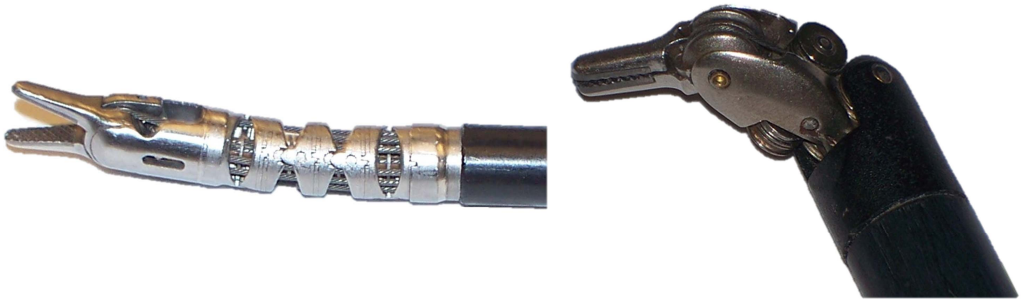

Figure 3.1: Intuitive Surgical's EndoWrists. Shown are the 5mm and 8mm needle drivers.

with the patient. Additional time is needed to reverse the process later in the surgery when the robot is no longer needed. The placement of arms can be limited as they all emanate from a single robotic base [103]. This can limit the choice of port locations when compared to traditional laparoscopic procedures. The lack of haptic feedback has resulted in rupturing of suture materials in the hands of inexperienced surgeons [103].

The size and placements constraints as well as improving the ability of robot and humans to work cooperatively has led to other robotic designs. Several robotic systems are attempting to reduce the bulk of the da Vinci's patient side manipulator cart, the part of the system that supports the robotic arms, by attaching the robotic actuators to the surgical bed. Systems such as the Laprotek system [97], the Raven system [60], and the University of Hawaii-Manoa [9] system work to addresses the size issues of the da Vinci system. The above systems use a series of smaller robotic arms which are directly supported by the surgical bed which allows for more collaborative work between the humans and the robot.

Though these systems may allow better surgical collaboration between robots and

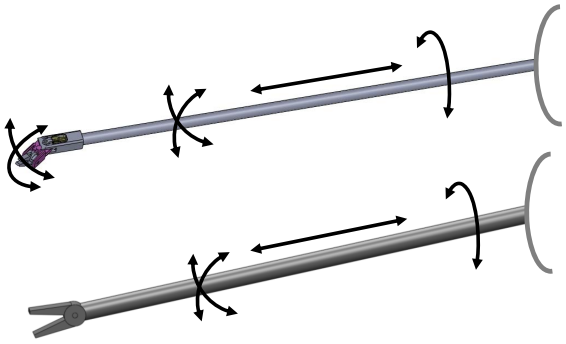

Figure 3.2: 6 vs. 4 degree of freedom graspers. The bottom figure illustrates the typical 4 DOF associated with a traditional laparoscopic tool. The top figure shows the additional 2 DOF added by a wrist at the end of the tool.

humans, the issue of cost is a still significant consideration. The purchase price of the da Vinci systems is substantial with quoted prices ranging from $1.3 million to $2.0 million [77] [103] for just the initial system purchase. The da Vinci system is estimated to add approximately $1500 to the cost of a surgical procedure with approximately 1/2 of that being the amortization of the interchangeable tools which have a defined number of uses [77]. The cost of future systems may be lower than that of the da Vinci system but robotic system costs will still be driven by the fundamental need for motors, primary and secondary sensors, power supplies, computers, sterile to non-sterile interfaces and the other parts needed to create a robotic rather than mechanical system.

Articulated manual tools have been offered as a means to address a number of the above issues. The commercial tools described in section 3.2 are similar in size, shape, and weight to conventional laparoscopic tools and can be used in conjunction with traditional manual tools. Like the da Vinci EndoWrist tools, these tools utilize a distal wrist to offer 6 DOF + grasp. Like traditional 4 DOF manual endoscopic

tools, the existing 6 DOF tools cannot achieve the level of natural control mapping possible with robotic tools. For example to move the distal wrist of a 6 DOF tool to the left the main shaft of the tool must, as observed at the surgical site, swing left. To do this, the surgeon must move the portion of the tool outside of the patient to the right, as would be required with a traditional 4 DOF tool. This means that lateral motions of the main tool shaft are reverse mapped due to the pivot point at the body wall. Insertion and retraction of the tool shaft into and out of the body is produced by a forward mapped movement of the surgeon's hand.

Surgeons can learn the mapping and coordination of existing 6 DOF manual tools with effort and practice, but the learning curve for laparoscopic surgeons is formidable. The ease with which it can be learned is one of the main reasons for the popularity of the da Vinci robot. The central objective of this chapter is to see if the naturalness of 6 DOF manual tools can be improved through appropriate mechanical design and interface mapping.

3.1 Chapter Contributions

This chapter hypothesizes that interface naturalness can be improved by following basic user interface design approaches. Thus, the first contribution is mathematical metric for naturalness and a design guideline, both of which can be used during the design of manual dexterous tool. The metric and guideline are based on analysis of the Jacobian relating the velocities of the user input with the distal grasper.

The second contribution of this chapter is the presentation of a pair of user interfaces based on the above metric and guideline for designing a natural interface.

The interface designs will be compared to interfaces based on existing tools via a user study. The third contribution of this chapter is the user study and its results. Notably, a conclusion that neither the current commercial tool interface designs nor the current research tool interface designs are well optimized to the needs of the operator.

The chapter will begin with an overview of existing dexterous, wristed laparoscopic tools followed by background theory on the human body's ability to orient and position objects. This leads into the discussion of naturalness and the Jacobian relating control input to grasper output. With the naturalness metric and guideline described, the creation of an improved user interface will be outlined. A pair of related interfaces were created as part of a set of test tools. The complete set of tools used in the user study represent both existing interfaces found via the literature review and the improved interfaces designed in accordance to the Jacobian-based methods. Finally, the user study and its results are presented in support of both the design theories and the interface designs.

3.2 Overview of Wristed Tools

This overview of wristed tools is intended to give the reader a frame of reference on this subject. It is not intended to be an exhaustive listing of all possible designs. The majority of the current concepts for manual dexterous tools in both research and the commercial space have three features in common. First, the tools have a primary rigid shaft similar to that of a conventional rigid laparoscopic tool. Second, they have a distal wrist. Third, they have a proximal user control with the ability to accept inputs to both position the primary tool shaft and to articulate the distal wrist joint.

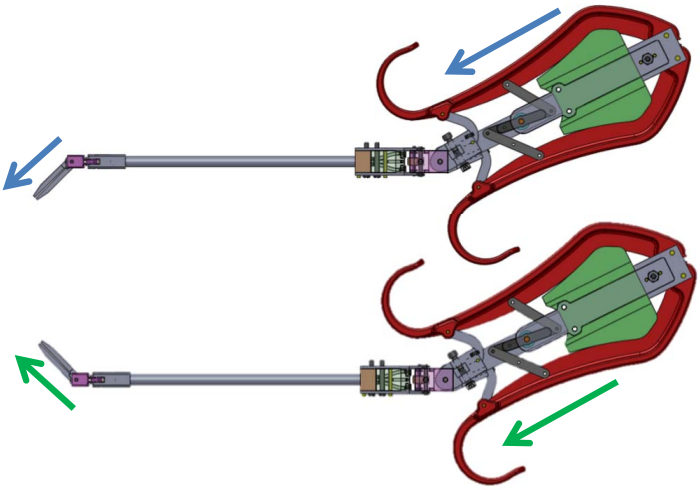

Figure 3.3: The top figure illustrates a "parallel mapping" where the direction of orientation of the handle and jaws remain approximately parallel. The lower figure illustrates the "anti-parallel" mapping.

Tools of this configuration, like traditional, rigid laparoscopic instruments, are presumed to be supported by a combination of the operator's hand and the laparoscopic port about which the tool pivots and passes into the body. Retaining this familiar configuration results in tools which can be integrated into a current surgical work-flow and setting. The majority of manual tools have a 2 DOF proximal wrist mechanism which is mechanically mapped to the distal wrist. A deflection of the proximal wrist results in a corresponding movement of the distal wrist. The mapping between the movements of the proximal and distal wrists fall into two general groups which will be referred to as parallel and anti-parallel (Figure 3.3). In the parallel case, the mapping of the control handle and end effector is such that the central axis of the two remain approximately parallel during articulation. The anti-parallel case represents the reverse of this mapping.

It is noted that the above are not absolute requirements for manual, dexterous

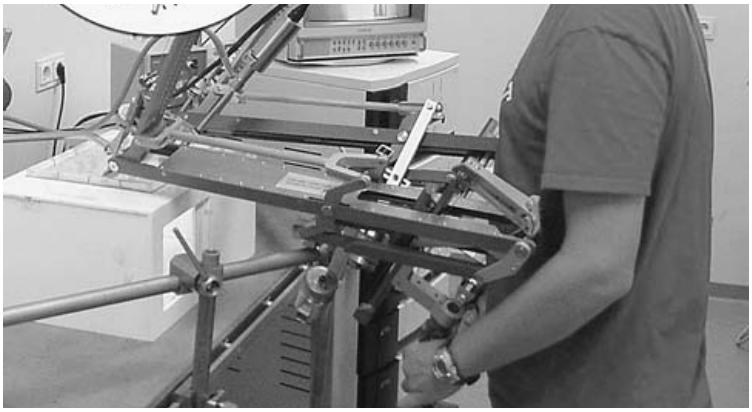

Figure 3.4: Manually actuated, dexterous surgical system based on pantograph mechanism [46].

tools. The system created by Jaspers et al. was based on a pantograph mechanism (Figure 3.4) [46]. This enabled the system to deliver scaled, parallel mapping between input and output like the da Vinci system, but without automation. However, the complexity of the system and the need to fix a base to the surgical bed prevent this from being a tool which would readily replace a traditional laparoscopic tool on the surgical tray.

3.2.1 Existing Commercial and Research Designs

The following is a brief description of manual, dexterous tools in the commercial and research spheres.

Novare Surgical Systems RealHand

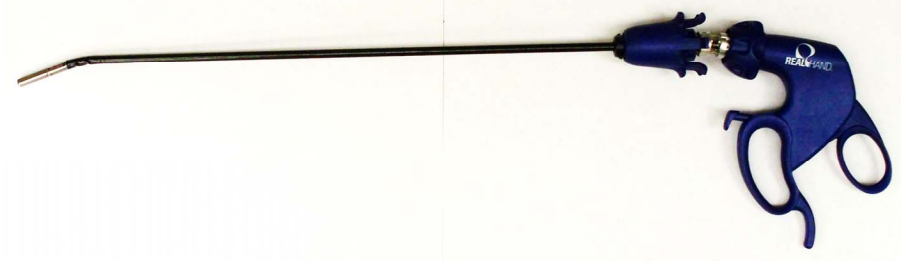

The RealHand [4] is a family of commercial, manually actuated tools. The wrist and control are coupled in an anti-parallel fashion. Based on measurements of an example tool, these tools have a factor of 1.5 scaling between the movement of the control and grasper wrists (i.e. the wrist deflects 1.5 times as far as the handle is deflected). Two models were available for study, a grasper (looped handles) and a needle driver (open handles).

CambridgeEndo Autonomy Laparo-Angle

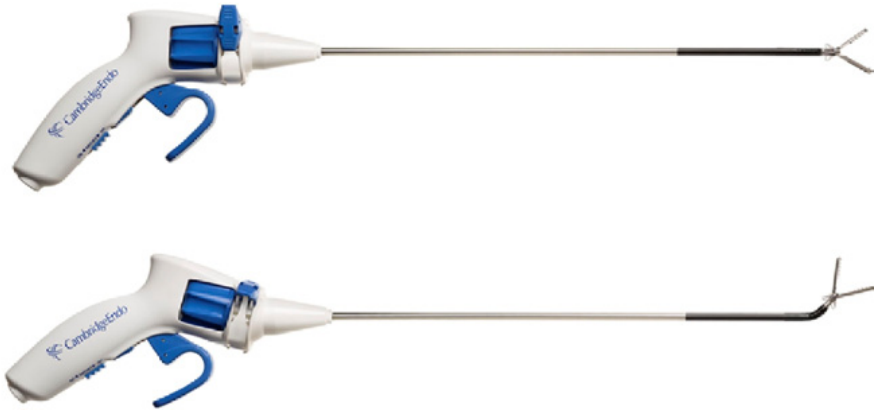

The Autonomy Laparo-Angle [1] is a commercial, manually actuated tool with operation and control is similar to that of the Novare RealHand. The wrist and handle move in anti-parallel fashion. Based on published images of the device it is estimated to have a factor of 1.5 scaling between handle and grasper wrists.

Radius Surgical System

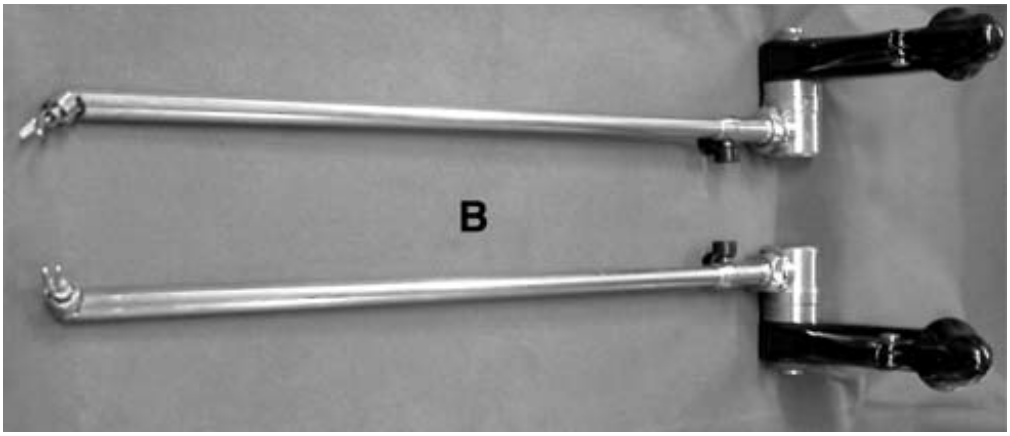

The Radius by Tuebingen Scientific [10] differs from the other listed systems. It uses gears and drive shafts to operate the end joint. This tool has only a single DOF wrist plus a rotation about the axis which supports the wrist. The system uses knobs and grasp triggers rather than the 2 DOF, joystick-like controls, used in many of the other manual tools. Because it does not contain a wrist joint at the handle end of the device it cannot be classified as parallel or anti-parallel.

Easy Grasp

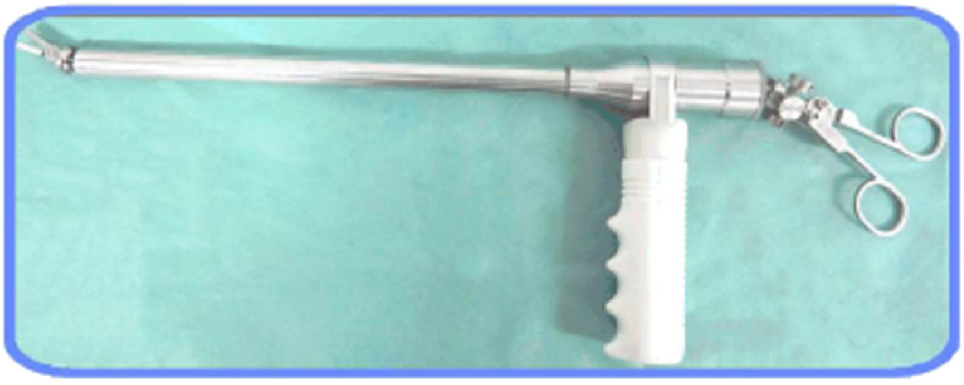

The Easy Grasp is a research tool developed by Wang et al. [105]. It uses a gimbal-based wrist joint. The handle and grasper are coupled such that they

remain parallel as the tool is articulated. Since the designers have stated that the jaws remain parallel with the control handle at all times (i.e. it is parallel mapped), it can be inferred there is no gain between the angle of the handle and grasper.

DragonFlex

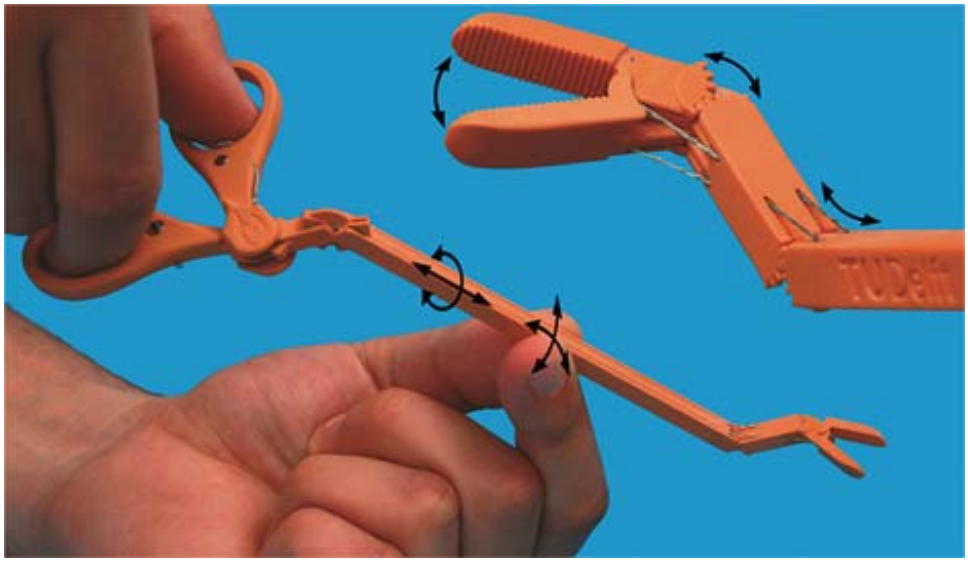

The DragonFlex is a research tool developed at Delft University by Jelinek et al. [47]. This tool is intended to be a low cost device made from just 6 primary parts. Rather than using revolute joints or flexures, the device uses a serial pair of rolling joints to achieve the 2 DOF of both the proximal and distal wrists. This tool has parallel mapping with no gain.

FlexDex

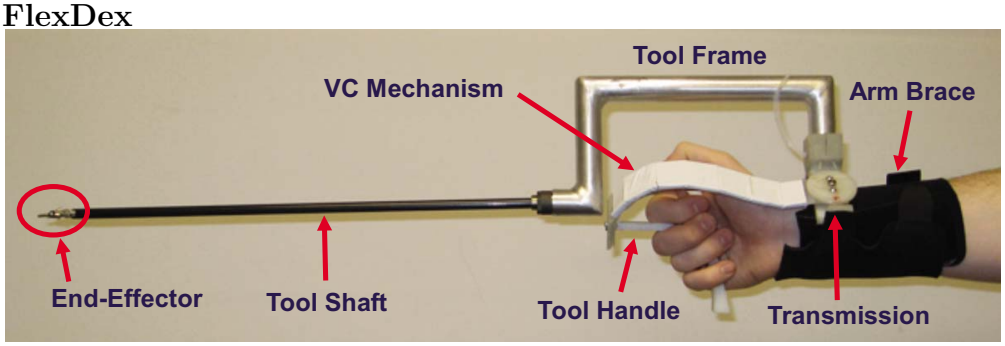

The FlexDex is a research tool developed by Awtar et al. [8]. It uses a gimbal-type wrist and a unique user control. The main shaft of the tool is attached to the operator's forearm. The control wrist is co-located with the operator's wrist thus the operator's hand controls the position of the grasper while the operator's

forearm positions the tool's main shaft. This tool has parallel mapping with no gain.

Daum Endohand

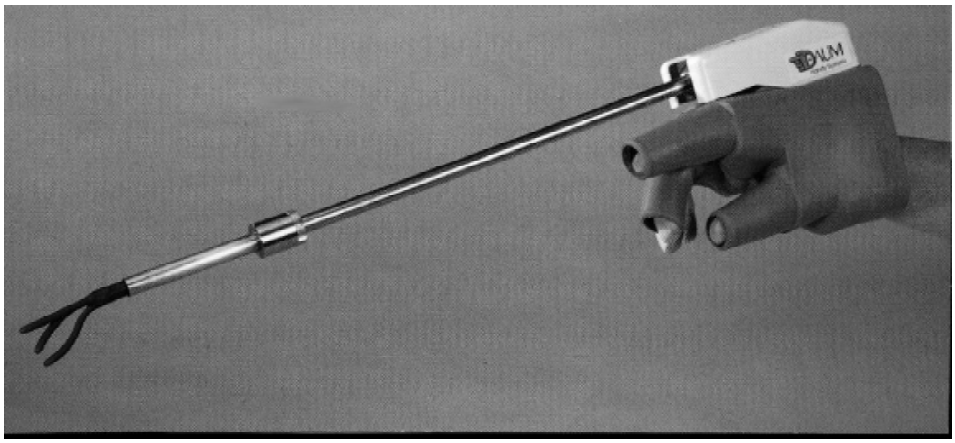

The Daum Endohand [63] is a 3 "fingered" manipulator. As with the FlexDex, the device is "worn" by the surgeon, this time as a glove rather than around the wrist. Movement of the surgeon's fingers are translated into movements of the tool's fingers. This tool is intended for laparoscopic tissue palpation, rather than for tasks such as needle driving.

3.2.2 General Tool Concept

The tools above suggest a general consensus in the layout of manual dexterous tools. The consensus is a control handle of some form attached to a proximal wrist. The deflection of the 2 DOF proximal wrist is coupled to the distal wrist inside of the body via cables or rods/links. The consensus does not extend to the location of the proximal wrist with respect to the handle nor the mapping (parallel, anti-parallel) between the proximal and distal wrists.

The exception to this consensus is the Tuebingen Scientific Radius tool. This tool

uses a gears and rotary shafts to transmit power to the wrist. The control input features rotary knobs. It is possible that such a configuration could be optimized for a specific surgical task but coordinating multiple grasper DOF requires the movement of multiple input knobs. As a general dexterity tool the knob type interface does not fit within the framework of the other devices.

For the remainder of the tools, and the investigation of a metric to guide the development of a natural user interface, we will consider questions of layout related to the handle and proximal wrist joint and the mapping between movements of the proximal and distal wrist joints.

3.3 A Definition of "Natural Motion"

As the starting point for a natural motion metric the authors have started with the supposition that one's hand has a natural local coordinate frame which is located within the grasp area of the hand. It is also assumed that the easiest way for the hand to act as a 6 DOF control input (i.e. controlling both rotation and position) would be if the rotational reference frame for the control, the origin of the handle, is located close to the hand's natural local reference frame. This would result in tight coupling between the natural position and orientation of the hand and that of the control. This notion of a local coordinate frame in the hand is supported in research literature.

Guiard [34] offered an example of a local coordinate frame being located within the dominant hand. His research proposed a kinematic relationship between the dominant and non-dominant hands of people when performing bimanual tasks. The

relationship, a kinematic chain, suggests that one hand is operated with respect to a local coordinate frame operated by the other. The non-dominant hand typically is used to position an object of interest and thus becomes a reference coordinate frame for the dominant hand, which typically is performing the detailed task. The task of writing with one hand while holding the paper with the other is offered as an example.

Filimon's work with functional MRI [28] considered the degree to which the brain processes reaching and grasping tasks in terms of hand vs. torso vs. target vs. world coordinate frames. Filimom suggests that the brain can translate between these frames. This would intuitively make sense for example in the case of a computer mouse where the position of the mouse in the hand does not have to be physically aligned with the screen in order to perform a controlled action. Without observing the mouse in the hand one can move the control to move the cursor on the screen.

Work with visuomotor skills suggests that consistent mapping between control input and output is important for reflexive control. Saunders et al. [85] experiments with visual feedback of hand movements suggest that it is desirable to avoid combining displacing and orientation tasks. The experiments were concerned with the degree to which the body would remap a change in visual information to the movements of the hand. The author concluded that both position and observed direction and rotation of motion were feedback used for hand control during fast phase movements. This would tend to stress the importance of not coupling the rotation of and positioning of a user control. Krakauer describes the visuomotor learning process required to mentally map a known physical motion to an expected output motion. This learning curve is minimized if the expected input and output are well correlated [52].

As a starting point for developing a framework for defining natural motion, the following are postulated:

- The human mind is able to naturally manipulate a local coordinate frame with respect to the hand. That coordinate frame is located within the hand's grasp and the mind is able to readily orient and/or position a held object with respect to the hand's coordinate frame. This coordinate frame is most natural to control if it is placed between the fingers in a pinch grasp. Some support for this concept comes from the generally agreed upon "intuitiveness" of the da Vinci user interface, which places the control point and coordinate frame between the user's fingers.

- A natural user interface would present a logical, simple and consistent mapping of motion between these two coordinate frames.

The above are assumptions which apply to a well designed master-slave robotic control system where there is a desire to create a natural mental mapping between the user control and the grasper at the working end of the tool. For this study, the da Vinci mapping is considered to have an ideal input to output relationship where a rotation of the operator's hand about a grasped item results in an equal rotation of the surgical grasper about its grasped item.

The nature of a 6 DOF laparoscopic tool based on the general configurations illustrated in Section 3.2.1 makes a da Vinci-like mapping impractical. For example the 6 DOF laparoscopic tools, like traditional 4 DOF tools, reverse the lateral movements of the surgeon's hands. The computer interface of the da Vinci system, in contrast,

duplicates the lateral motions of the surgeon's hand. Instead the design goals for a practical, natural interface should attempt to decouple rotational and linear movements as suggested by Saunders as well as retain a consistent relationship between input action to the control and output result as observed at the tool end effector.

3.4 Jacobian-Based User Interface Metrics

In robotics, the manipulator Jacobian relates the velocity of a robot's individual joints to the velocity of its end effector [68]. In this section a Jacobian-based method is proposed to measure, compare and optimize the mapping of the user interface to the grasper of a manual tool, based on a variation of the manipulator Jacobian. The input "joint angle velocities" will be an input linear and angular velocity applied to the handle's base frame. In the interest of minimizing cross coupling discussed in Section 3.3, the ideal mapping is defined as one in which rotational input velocities at the handle result in no linear velocities at the handle.

3.4.1 A Jacobian-Based Coupling Metric

Several assumptions were made in Section 3.3 regarding what makes the control and movements of a tool natural for the user. The movements of the grasper were broken down into linear and rotational movements. These ideally would be commanded by linear and rotational movements of the control handle. If the inputs in the handle frame (h) and outputs in the grasper frame (g) of the devices are thought of as a 6 DOF twist coordinate vectors, $\begin{bmatrix} \boldsymbol{v} \\ \boldsymbol{\omega} \end{bmatrix}$, then the input and output relationship of the

handle and grasper can be related by a Jacobian, $\boldsymbol{J}$. This relationship can be written as:

$$\dot{\boldsymbol{x}}_g = \boldsymbol{J}\dot{\boldsymbol{x}}_h \tag{3.1}$$

The components of the above equation are expanded below:

$$\begin{bmatrix} \boldsymbol{v}_g \\ \boldsymbol{\omega}_g \end{bmatrix} = \begin{bmatrix} \boldsymbol{J}_1 & \boldsymbol{J}_2 \\ \boldsymbol{J}_3 & \boldsymbol{J}_4 \end{bmatrix} \begin{bmatrix} \boldsymbol{v}_h \\ \boldsymbol{\omega}_h \end{bmatrix} \tag{3.2}$$

This Jacobian is a 6×6 matrix. If $\boldsymbol{J}_2$ and $\boldsymbol{J}_3$ were zero matrices, one would have an ideal tool, namely one where any single input rotation or displacement velocity applied to the handle results in corresponding (possibly scaled) output at the grasper with no coupling between displacements and rotations.

The method outlined below directly measures the magnitude of the linear output of the grasper for a rotational input to the handle. The outputs can be compared directly and the relative performance of each tool can be compared without concerns for scaling rotational vs linear displacements. This is done by using the portion of the Jacobian which relates rotational inputs to linear outputs. The magnitude to which the Jacobian can magnify a rotational input as a linear output can be used to directly compare tool performance.

The off diagonal sub-matrices $\boldsymbol{J}_2$ and $\boldsymbol{J}_3$ relate input rotation velocities with output linear velocities and input linear velocities with output rotational rotations respectively. We will refer to these matrices as the "Cross Correlation" matrices. The magnitude of these relationships, the degree to which an input rotational velocity

creates an output linear velocity, can be measured using a 2-Norm. The result is used as a basis for comparison and optimization. The 2-Norm of a matrix defines the maximum stretch a matrix could apply to any vector [101]. Section 3.3 identified the undesirable relationship between rotational vs. linear input and output velocities. The magnitude of 2-Norm of the Cross Correlation matrices ($\boldsymbol{J}_2$ and $\boldsymbol{J}_3$) quantify these relationship where the ideal value is zero.

When comparing rotational and linear terms of the Jacobian scaling is a concern. Sub-matrix $\boldsymbol{J}_3$ considers the rotation of the grasper for a linear input motion. However, the long main-shaft with a roughly central pivot characteristic of laparoscopic tools results in relatively small angular changes for a linear input, making analysis of $\boldsymbol{J}_3$ not very instructive for comparative purposes. A focus on Sub-matrix $\boldsymbol{J}_2$, which considers the linear displacement of the grasper for a rotation input, yields productive results. A comparison of Cross Correlation values of the tools described in Section 3.2.1 shows significant differences between tools. The relative values are shown in Table 3.1.

3.4.2 Cross Correlation Matrix Derivation

This section will describe the process used to determine the Jacobian of a tool. The process is illustrated using the tool detailed in Chapter 4. It starts with establishing the forward kinematics of the grasper and the handle, with respect to the world frame located at the tool's pivot point, typically a surgical trocar. This also includes assigning the frames which define the locations of the grasper frame (the working point of the end effector) and the handle frame (the frame about which the user's hand

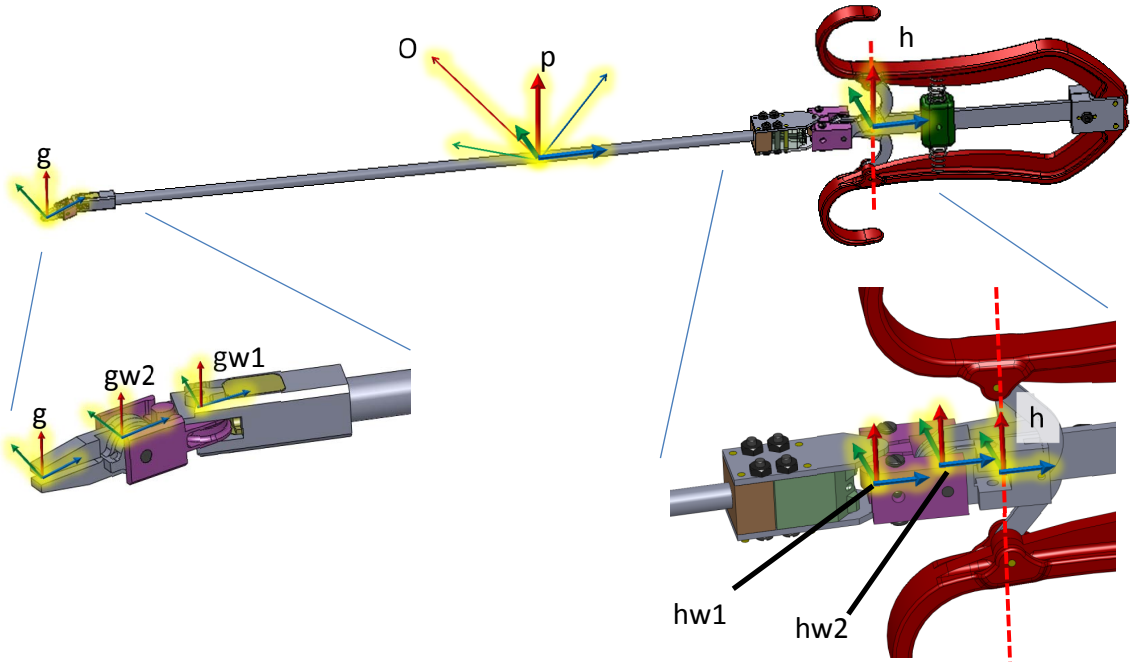

Figure 3.5: Coordinate frames of the prototype tool shown as an indicative of tool origins. The four primary frames are, the grasper frame (g), the world frame/origin (O), the pivot frame (p), and the handle frame (h). Frames gw1, gw2, hw1, and hw1 are frames for the grasper wrist joints 1 and 2 and handle wrist joint 1 and 2. The pivot frame is collocated with the origin but rotated to align with the axis of the tool. Also noted are the intermediate frames of the grasper wrist and handle wrist.

moves). Next, the relationship between grasper and handle joint angles is defined (e.g. for a 15° deflection of the handle's wrist joint the grasper wrist defects X°). With the joint angle relationships defined, the movement of the grasper for a given movement of the handle can be calculated thus a Jacobian relating the movements of the handle to the movements of the grasper can be defined. The Cross Correlation measure is calculated from this Jacobian.

Step 1: Defining the Kinematics

The first step in calculating the Cross Correlation measure is defining the handle to grasper kinematics with respect to the tool's pivot point at the trocar. The kinematics

of the internal/grasper side and external/handle side of the tools are defined with respect to the world origin O. Figure 3.5 illustrates the three origins of interest to this analysis; the origin of the grasper, handle and world frame. The world frame origin is the defined as the point where the tool passes through the trocar. It is understood that movements of the tool in and out of the body will move this point with respect to the tool's main shaft. This is accounted for in the kinematics (See Figure 3.6).

The assignment of the handle origin is not precise. For tools operated with a pinching grasp (pliers or tweezer like handles) the origin should be placed between the pinched thumb and forefinger. For pistol grip tools an origin placed within the loop formed by the first finger and thumb was used (See Figure 3.11). Note that for all tools the location of the handle origin may vary depending on the exact way the user grasps the tool. For example if two users grasp a cylindrical handle at different locations the exact handle origin will change.

Like the handle frame, the grasper frame must be assigned based with some level of assumption. The location should be at the point where the grasper would interact with the working environment (the point where a needle would be grasped for example). Figure 3.5 illustrates the locations of the grasper, handle and origin frames for a sample tool.

With the assignment of the origin, grasper frame and handle frame the kinematics of the tool is derived. The tool is conceptually divided into two kinematic chains that can be thought of as two serial robotic arms, one extending from the trocar (the origin of the system) to the handle and one from the trocar to the grasper. The basic

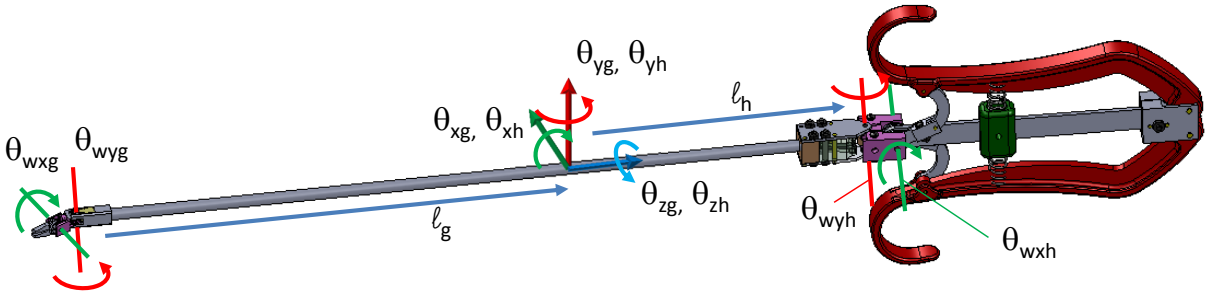

Figure 3.6: The 12 joint angles used to describe the position of the tool handle and grasper. Note the three Euler rotations about the origin are the same with respect to both the handle and grasper kinematics.

form of the serial chains will be be that of a spherical joint followed by a prismatic joint and finally the joints of the wrist mechanism. Figure 3.6 illustrates the 12 joint variables of the grasper and handle sides of the sample device. The pairs of wrist angles, one pair for the 2 DOF grasper wrist and one for the 2 DOF handle wrist, are coupled by the internal mechanism of the tool. The exact joint variables would will depend on the kinematics of the particular tool.

The next kinematic step is creating the general homogeneous transforms between the origin and the grasper and origin and the handle. Thus the handle frame and grasper frame should both be expressed with respect to the common origin frame located at the trocar pivot point. For the example device these transforms are shown below. The super and subscript labels refer to the origins in Figure 3.5.

$$ {}^{o}_{g}\boldsymbol{T} = {}^{o}_{p}\boldsymbol{T}\ {}^{p}_{gw1}\boldsymbol{T}\ {}^{gw1}_{gw2}\boldsymbol{T}\ {}^{gw2}_{g}\boldsymbol{T} \tag{3.3} $$

$$ {}^{o}_{h}\boldsymbol{T} = {}^{o}_{p}\boldsymbol{T}\ {}^{p}_{hw1}\boldsymbol{T}\ {}^{hw1}_{hw2}\boldsymbol{T}\ {}^{hw2}_{h}\boldsymbol{T} \tag{3.4} $$

Where 'g' and 'h' refer to the grasper and handle side joints respectively.

The specific chain for a given tool will depend on the specific structure of the tool. For example a wrist joint comprised of more than one pair of orthogonal sub-joints such as that used on the RealHand would have a series of transforms representing the 2 DOF wrist joint rather than just the pair indicated above. The end effector jaw degree of freedom is not included in this kinematic chain.

The final step to create the kinematic chains for a device is establishing the joint relationships between the handle joints (θ_{wxh} and θ_{wyh} in Figure 3.6) and the grasper joints (θ_{wxg} and θ_{wyg} in Figure 3.6). In the example tool the position of the grasper and handle are defined by the following joint variables:

$$\boldsymbol{q}_g = \begin{bmatrix} \theta_{xg} \; \theta_{yg} \; \theta_{zg} \; l_g \; \theta_{\omega yg} \; \theta_{\omega xg} \end{bmatrix}^T \tag{3.5}$$

$$\boldsymbol{q}_h = \begin{bmatrix} \theta_{xh} \; \theta_{yh} \; \theta_{zh} l_h \; \theta_{\omega yh} \; \theta_{\omega xh} \end{bmatrix}^T \tag{3.6}$$

The relationship between the variables of $\boldsymbol{q}_g$ and $\boldsymbol{q}_h$ and their respective derivatives is typically linear for this sort of device. For example a 5° rotation of the handle wrist joint will result in an $m(5°) + b$ rotation of the corresponding grasper joint where m and b are scalars. Theoretically the use of cams or other mechanisms could result in a non-linear input-output relationship between $\boldsymbol{q}_g$ and $\boldsymbol{q}_h$. As this is not the case for any of the tools listed in Section 3.2.1 a non-coupled, linear relationship will be used in this analysis. In matrix form the relationship between $\boldsymbol{q}_g$ and $\boldsymbol{q}_h$ is expressed below where $\boldsymbol{M}$ is a diagonal matrix and $\boldsymbol{b}$ is a vector of offsets:

$$\boldsymbol{q}_g = \boldsymbol{M}\boldsymbol{q}_h + \boldsymbol{b} \; . \tag{3.7}$$

The derivative of 3.7 is:

$$\dot{\boldsymbol{q}}_g = \boldsymbol{M}\dot{\boldsymbol{q}}_h \tag{3.8}$$

Step 2: Calculate the Jacobian

In the previous step equations for the homogeneous transformations from the origin at the trocar to the grasper frame and the handle frame were derived. These transforms were be based on a series of joint variables (Equations 3.5 and 3.6 in this example). A pair of Jacobians relating the a fore mentioned joint variables with the velocities of the grasper and handle (Equations 3.9 and 3.10) can be derived using the method described by Murray et al. [67].

To perform the motion analysis the relationship between input and output is expressed as in Equation 3.1, namely $\dot{\boldsymbol{x}}_g = J\dot{\boldsymbol{x}}_h$. To relate $\boldsymbol{J}$ to $\boldsymbol{M}$ we can define individual Jacobians for the grasper and handle as:

$$\dot{\boldsymbol{x}}_g = \boldsymbol{J}_g\dot{\boldsymbol{q}}_g \tag{3.9}$$

$$\dot{\boldsymbol{x}}_h = \boldsymbol{J}_h\dot{\boldsymbol{q}}_h \tag{3.10}$$

Substituting 3.8 into 3.9 and applying 3.10 to replace $\dot{\boldsymbol{q}}_h$ results in:

$$\dot{\boldsymbol{x}}_g = \boldsymbol{J}_g\boldsymbol{M}\boldsymbol{J}_h^{-1}\dot{\boldsymbol{x}}_h. \tag{3.11}$$

Thus the Jacobian relating the grasper and handle is:

$$\boldsymbol{J} = \boldsymbol{J}_g \boldsymbol{M} \boldsymbol{J}_h^{-1} \tag{3.12}$$

It should be noted, because this analysis is based on the body frame Jacobian, components of the joint vectors $\boldsymbol{q}_h$ and $\boldsymbol{q}_g$ which do not affect the body frame Jacobian can be ignored. The homogeneous transform of the grasper with respect to the handle can be written from Equations 3.3 and 3.4, as:

$$^{h}_{g}\boldsymbol{T} = ^{h}_{O}\boldsymbol{T}\ ^{O}_{g}\boldsymbol{T} \tag{3.13}$$

which expands to:

$$^{h}_{g}\boldsymbol{T} = ^{h}_{hw2}\boldsymbol{T}\ ^{hw2}_{hw1}\boldsymbol{T}\ ^{hw1}_{p}\boldsymbol{T}\ ^{p}_{O}\boldsymbol{T}\ ^{O}_{p}\boldsymbol{T}\ ^{p}_{gw1}\boldsymbol{T}\ ^{gw1}_{gw2}\boldsymbol{T}\ ^{gw2}_{g}\boldsymbol{T} \tag{3.14}$$

The transforms $^{O}_{p}\boldsymbol{T}$ and $^{p}_{O}\boldsymbol{T}$ reduce to identity. Three of the six terms of $\boldsymbol{q}_g$ appear only in $^{O}_{p}\boldsymbol{T}$. The remaining three terms are related to the terms of $\boldsymbol{q}_h$ by equation 3.7. This means the body frame Jacobian relating the grasper and handle frames has only 3 DOF. This will be true for all laparoscopic tools which have a rigid shaft connecting the grasper and handle wrists.

Step 3: Calculate the Cross Correlation Mean

In this final step the Jacobian will be calculated over a range of workspace poses. The Cross Correlation mean will then be calculated at each pose and the largest value (or

the average value if preferred) can be used for comparison or optimization. In the previous steps the tool joint variables were identified (Equations 3.5 and 3.6). As was shown in Step 2, only the two joint variables associated with the tool wrist affect the Cross Correlation mean thus the span of the workspace can be tested via permutations of those two variables. In this example the grasper wrist variables are θ_{wxg} and θ_{wyg}. The analogous handle variables are simply functions of the wrist variables. For each Jacobian matrix the 2-norm can be calculated as described in Section 3.4.1. Either the largest or the average Cross Correlation value can be used for comparison or optimization purposes.

Frame Dependence

It should be noted that the Cross Correlation measure is dependent on the assigned location of the user handle frame and the frame where the grasper is said to act; thus the measure is frame independent. As a example, Figure 3.7 illustrates two tools which are kinematically identical save for the length of the working jaws. If the location of the point of grasp frame is located at the tips of the jaws then the kinematic relationship between the handle and point of grasp of the two tools will be different despite mechanical structures which are nearly identical. If the point of grasp of both tools are assigned to a point at a given distance from the base of the jaws (e.g. 10 mm from the base of the jaws regardless of the jaw length) then the tools will have identical Cross Correlation measures. Thus this example illustrate the effect of the placement of the grasp frame on the comparison of two similar tools.

Given that the placement of the grasp frame is to some extent arbitrary, the

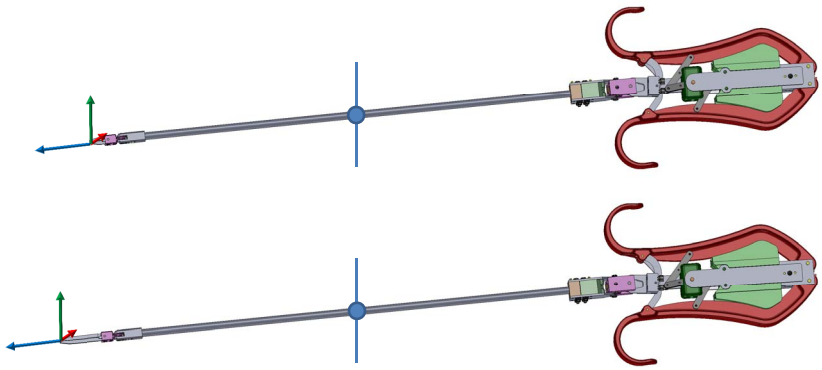

Figure 3.7: Illustration of the frame dependence of the Cross Correlation measure based on the location of the grasping frame. The two tools illustrated are identical with the exception of the length of the grasping jaws. When the point of grasp frame is placed at the tip of the jaws, the longer jaws of the lower model result in a different kinematic relationship between the handle and grasper tip movements. If the point of grasp of the two tools is defined as the same distance from the base of the jaws for both tools (e.g. the point of grasp is 10 mm from the base of the jaw for both tools) then the Cross Correlation measure will be the same for both tools regardless of the difference in jaw length.

nearly identical design of these two example tools it is reasonable to consider a metric which is frame independent. A frame independent measure would result in identical performance of the two example tools. However, this might not be desirable. The change in jaw length of the two tool, like other mechanical changes which result in kinematic differences between compared tools, can result in changes in the user perception and feel. That said, further investigation of frame independence may result in additional usability insights which were not investigated in this thesis.

3.4.3 Theory of Jacobian Inversion

In Section 3.3 it was postulated that a feature of a natural interface is consistent mapping between input and output actions. In terms of a body Jacobian relating input to output consistency would be a Jacobian that remained unchanged over the

span of the workspace. In this case consistency refers to an input movement of the user handle vs the resulting output movement of the tool's grasper.

In a robotic master-slave system a controller can enforce a constant input-output relationship between an input in the local frame of the user control and and output in the local frame of the end effector. In terms of the Jacobians discussed in this chapter this represents a Jacobian which is fixed over the complete workspace. The diagonal terms of the Jacobian relating input to output movements are those which relate primary movements of the input to output (e.g. movement of the user control in the handle's z-axis vs movement of the end effector along its z-axis). The off diagonal terms are typically minimized as they represent a movement of the end effector that is not perfectly mapped to the input (e.g., a movement of the input along the x-axis resulting in output movement along the x-axis plus a smaller movement along the y-axis).

In the case of a mechanical manipulators the relationship between input and output changes over the tool's workspace. The degree to which the relationship chances can affect the naturalness of the tool's interface. The variation in the relationship comes in two forms; changes in the primary diagonal elements and changes in the secondary off diagonal elements. Of particular interest are changes in the diagonal terms of the Jacobian. An inversion of a diagonal term represents a case where the control mapping has significantly changed. For example, a forward movement of the user control along the handle's z-axis results in a rearward z-axis movement of the end effector in one part of the workspace but a forward movement in another. This inversion of one or more diagonal terms represents a significant change in the mapping

between the user control and the end effector.

The off diagonal terms of the input-output Jacobian represent secondary movements of the output. While the off diagonal terms represent an "error" in the input-output relationship, the diagonal terms represent the desired outcomes. That is, an input movement along the z-axis should result in an output movement along the z-axis and ideally no output movements along the other axes.

Some manual tools exhibit a trait where the diagonal elements of the Jacobian invert over the workspace resulting in a change in user control over the workspace. Figure 3.8 illustrates such an inversion by comparing two similar tools with a single change to the way tools are mapped. When either tool is in a straight configuration a forward movement of the handle results in a forward movement of the end effector. With the anti-parallel mapped tool deflected to 45° the forward movement of the handle (along the handle's axis) results in a diagonal movement of the grasper (forward and to the side in the grasper frame). In both cases a forward movement of the handle resulted in some forward movement of the end effector.

Figure 3.8 also illustrates a parallel mapped tool. While the parallel and anti-parallel behavior is identical in the straight configuration, the parallel mapped tool shows an inversion in the 45° case. A forward movement of the handle results in the end effector moving laterally and rearward. At some point in the workspace a pure z-axis movement of the handle would result in no z-axis movement of the end effector. Thus the user perception and understanding of the control must constantly change over the workspace.

Figure 3.9 contains examples of the minimum and maximum values for each ele-

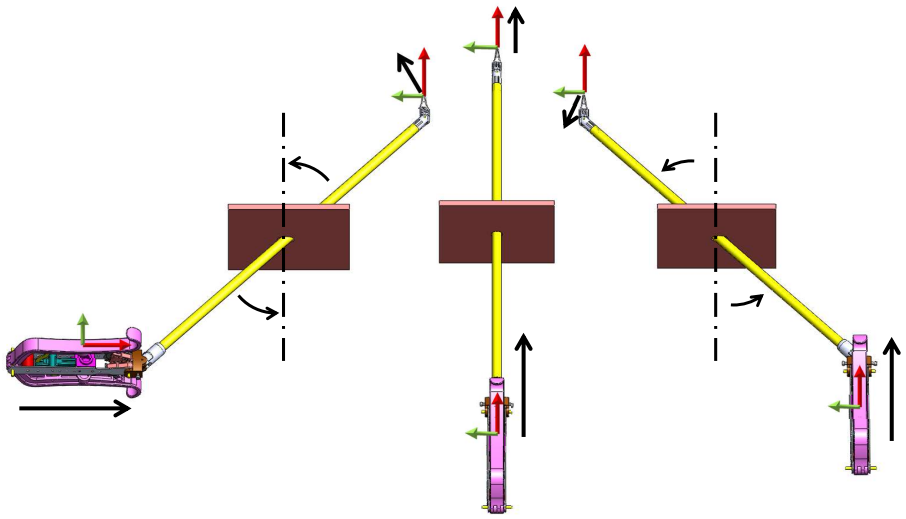

Figure 3.8: Illustration of the inversion of diagonal terms of a Jacobian. The figure shows posses of two tools. The left figure is an anti-parallel mapped tool articulated to 45°. The right figure is a parallel mapped tool also articulated to 45°. As both tools look identical when in the straight configuration, the center figure represents both tools. Local coordinate frames (Red-Green arrows) are shown for both the handle and grasper in all three figures. In all three figures the handle is moved along the axis of the handle coordinate frame (black arrow). The resulting movement of the grasper tip In the case of the left and center tools the handle movement results in a forward movement of the grasper. The grasper of the parallel mapped tool on the left moved backwards in the articulated configuration.

Prototype Tool - Parallel Mapping							Prototype Tool - Anti-Parallel Mapping						
-1.89425	-1.03589	-1.45266	Minumum Jacobian Values Linear Terms (left)			υ	-2.17387	-0.34985	-0.64536	Minumum Jacobian Values Linear Terms (left)		
-1.39018	-1.75044	-1.22591					-0.43941	-1.98211	-0.51393			
-1.44391	-1.55457	-1.31458					-0.4538	-1.00897	0.659642			
Minumum Jacobian Values Rotational Terms (right)			1.615138	-0.40162	-0.56321	ω	Minumum Jacobian Values Rotational Terms (right)			-1.74909	-0.31676	-0.50168
			-1.62E-14	0.88975	-0.45645					-0.03422	-1.28565	-0.43459
			-2.32E-14	-0.45645	0.88975					-0.07941	-0.68681	0.894675
υ			ω				υ			ω		
0.133053	1.035888	1.452657	Maximum Jacobian Values Linear Terms (left)			υ	-0.8522	0.349854	0.645365	Maximum Jacobian Values Linear Terms (left)		
1.390179	0.525809	1.225913					0.434421	-0.79017	0.513931			
1.443913	1.554573	0.963873					0.453801	1.008975	1.484457			
Maximum Jacobian Values Rotational Terms (right)			1.647455	0.401622	0.563207	ω	Maximum Jacobian Values Rotational Terms (right)			-1.65475	0.392259	0.501676
			1.62E-14	0.998613	0.456449					0.034223	-0.86891	0.434586
			2.19E-14	0.456449	0.998613					0.079406	0.686807	1.011927

Figure 3.9: Minimum and maximum values taken from the range of Jacobians for the parallel and anti-parallel mapped prototype tools described in Table 3.1. Each of the four blocks of values (upper-left, lower-left, upper-right, lower-right) represents the locations of a 6×6 Jacobian with the off diagonal sub-matrices removed. The values in each block are not a single Jacobian but the maximum or minimum value for each location of the Jacobian over the articulation range of the tool. Note that the sign of the diagonal velocity elements of the parallel mapped tool invert (highlighted values). This indicates that at some point in the tool's workspace the relationship between the direction of movement of the handle and grasper reverse.

ment of the on diagonal, sub-matrices of two example tools over their ranges of motion. The inversion of the values relating linear velocities of the handle to the grasper can be seen in the parallel mapped tool but not in the anti-parallel mapped tool. Note that the diagonal values relating input and output velocities of the parallel mapped tool (highlighted values) change sign over the workspace. It is therefor assumed that a parallel mapped tool will be more difficult to operate over the workspace.

3.4.4 Cross Correlation Tool Comparison

A comparison of tools identified in the existing literature as well as that of the proposed prototype was conducted. Not all tools were available for measurement and inspection. Where exact dimensions of tool link lengths were unknown estimations were used. All tools were normalized to have a working shaft length similar to that of

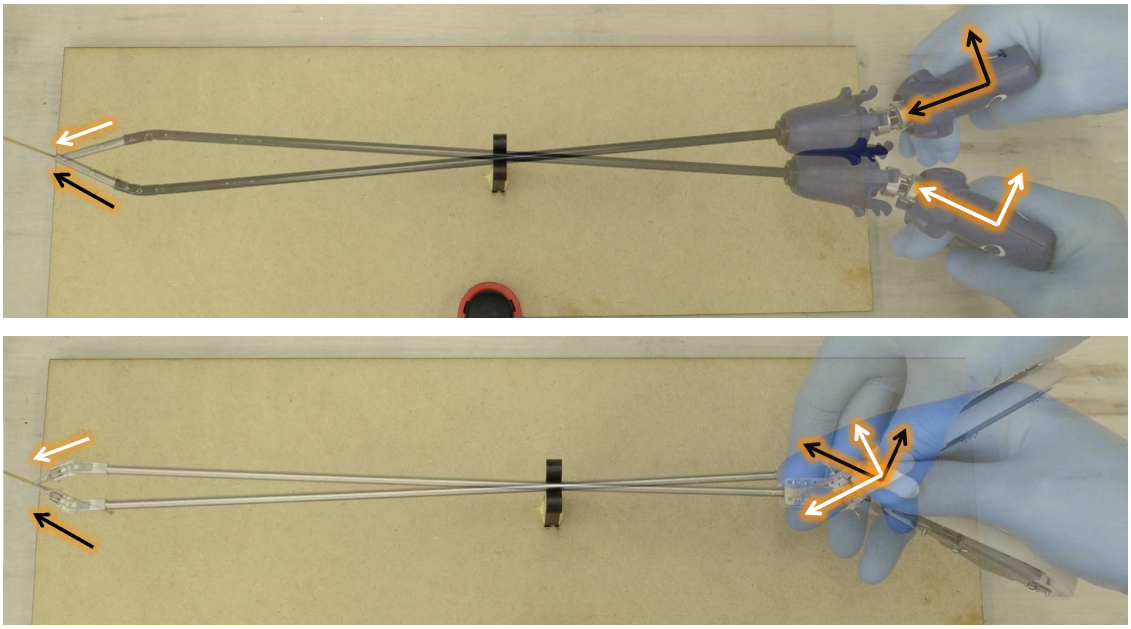

Figure 3.10: Double exposure images illustrating the relative movement of the user control required to rotate the tool tip about a fixed point (Top:RealHand, Bottom:Prototype (Chapter 4)).

the RealHand, 350 mm between grasper and handle wrist joints, except in the case of the FlexDex. The location of the FlexDex's external wrist, physically behind the operator's hand, required an assumption of a longer effective working shaft. Additional length was added to account for the space between the actual handle wrist joint and the end of the main shaft located in front of the operator's hand. The location of the handle origin is not an exact point and thus was estimated as follows. For tools with finger loops, the origin was assumed to be in at the center of a line connecting the two loop centers. For the tools using a pistol the origin is estimated to be within the grasp of the middle finger and aligned with the central plane of the tool (Figure 3.11). The results of the tool cross correlation are shown in Table 3.1. Figure 3.10 illustrates the difference in hand movement.

Figure 3.11: The designated location of the RealHand's origin. This location is shown as representative of the origin location for devices using a pistol style grip.

Tool	**Joint Mapping**	**Data Source**	**Notes**	**Average Cross Correlation**
Prototype	Parallel	CAD model	Diagonal Elements of the Jacobian Invert.	18.13 mm/rad
Prototype	Anti-Parallel	CAD model		41.34 mm/rad
EasyGrasp	Parallel	Estimated based on published images	Linear dimensions were estimated. The 1:1 ratio of handle to grasper rotation is stated in published papers. Diagonal Elements of the Jacobian Invert.	61.88 mm/rad
FlexDex	Parallel	Estimated based on published images	Main shaft was extended by 170 mm to account for the location of the operator's hand forward of the handle wrist joint. Diagonal Elements of the Jacobian Invert.	66.40 mm/rad
RealHand Needle Driver	Anti-Parallel	Physical Measurements		149.36 mm/rad
Cambridge-Endo	Anti-Parallel	Estimated based on published images	Based on photos the dimensions and ratio of handle rotation to wrist rotation were estimated to be similar to the RealHand	151.15 mm/rad
RealHand	Anti-Parallel	Physical Measurements		155.94 mm/rad

Table 3.1: Tools modeled for Cross Correlation Norm comparison

The mean Cross Correlation value was calculated for each tool over a range of poses. Each wrist axis ($\theta_{\omega yg}$, $\theta_{\omega xg}$) was articulated over $\pm 45°$. The absolute limits of the movement of the tool through the trocar, along its main shaft are when the tool is pulled out of the trocar or the handle is against the trocar. These are not practical working limits so working limits were assumed. The main tool shaft was extended through the trocar far enough to reach depths ranging from 120-200 mm. Note, a Cross Correlation value was not calculated for all of the tools listed in Section 3.2.1. The Dragonflex kinematics are similar to the EasyGrasp tool. The Radius tool does not have a 6 DOF user interface with a proximal wrist and thus an appropriate Jacobian cannot be readily calculated. The Endohand does not have an articulated proximal or distal wrist.

3.5 Test Tools and User Study

The overall objective of the study was to test the ability of the Cross Correlation value to predict relative user performance when comparing competing tool designs as well as the impact of inverting terms of the Jacobian. This test was conducted using a set of tools purpose-built for the experiment, in order to minimize tool to tool differences which could affect the outcome but were not characterized by the Cross Correlation Norm. The test tools are described in Section 3.5.3.

The objective tasks of the study were intended to meet several requirements. First, the tasks should relate to existing surgical tasks such as suturing as well as object manipulation and placement. Second, the tasks should require some level of wrist articulation to complete. The user should not be able to complete a task by

effectively locking the wrist into a pose and then proceeding to complete the task as if using a rigid tool.

As a secondary objective the desired motions needed to complete a task should be self identifying. For instance, asking a surgeon trained in laparoscopy to complete a suture with thread and needle is perfectly reasonable. Asking the same of an untrained participant would likely not yield information beyond their inability to complete the task.

3.5.1 Test Tasks

Two dexterous tasks were created for this user study. Both tasks required users to maneuver a metal ring over a rigid wire form while avoiding contacts. The first task was a ring transfer test and is similar to the pick and place tests of the Fundamentals of Laparoscopic Surgery training (Figure 3.12). The test ring is held such that the axis of the ring and the grasper are aligned (Figure 3.12). The bends in the wire posts ensures the test cannot be completed without articulating the tool wrist. The ring, starting at the base of the wire, is transferred from the left wire to the base of the right wire and the task performance metrics are recorded. The task is then reversed (right to left) and the performance is again recorded. Thus a single participant will perform two transfers with each tool.

Suturing is often cited as a task which is difficult to perform using traditional straight surgical tools. The second tasks require the participant to move a metal ring along a sinusoidal wire frame. The path enforced by the wire is intended to require the user to move the jaw over a path similar to that of placing a suture (Figure 3.13).

The longitudinal axis of the wire frame is placed at 15° and -15° off perpendicular to the entry port. A ring is held in the tool jaws as shown in Figure 3.13. Thus, when the ring is held normal to and is moved over the "W" shaped wire path, the tool moves in a path similar to that of placing a suture. For each angle, the task is conducted in the forward and reverse directions, for a total of four runs per tool, per participant.

This task was used in lieu of an actual suturing task for several reasons. First, the test participant population includes a naive user group with no previous surgical experience and are assumed to be unfamiliar with placing a suture. Thus this task provides a guide for those unfamiliar with the task without having to actually teach suturing skills to the participant. Second, the ring traverse task can be scored using the same methods as the ring transfer task allowing for more ready comparison of test data. Finally, the 3D printed test tools do not have the grasp strength required to properly control a surgical needle.

For both task types (ring transfer, traversing the sinusoidal wire), participants were told to avoid touching the rings to the wire and to avoid contact at the expense of overall task time. Leads were connected to the rings as well as the transfer wires to record contacts. A test circuit recorded the number of contacts and the cumulative duration of the contact. Contacts which occur less than 200 ms apart are considered a single contact. All three tasks were completed with a single tool before switching test tools. The order of the tasks (ring transfer task, $+15°$ sinusoidal traverse, $-15°$ sinusoidal traverse) and the order in which the tools were presented were randomized for each user. Users were allowed to practice with the tools and the tasks prior to

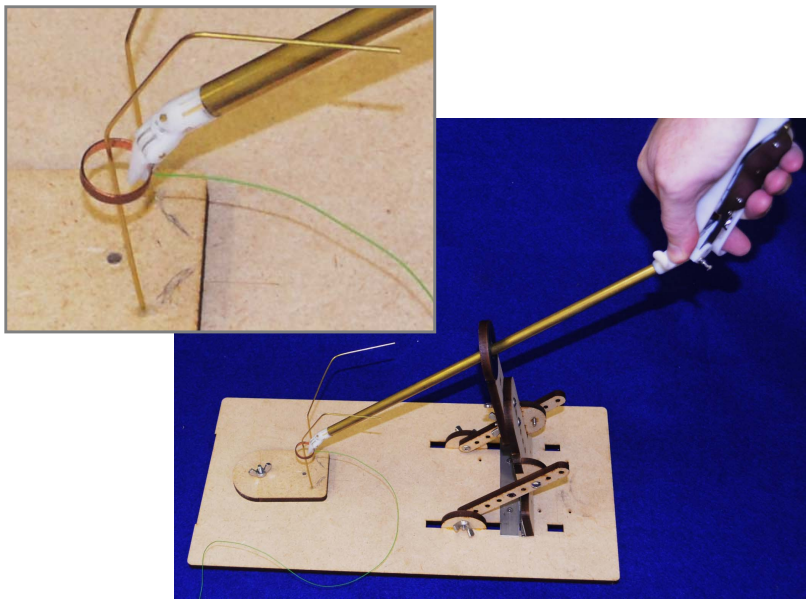

Figure 3.12: The ring transfer test is similar to the peg transfer tests used in the Fundamentals of Laparoscopic Surgery test. The ring is held as shown and transferred from the base of one wire to the base of other.

starting the scored tests.

Three metrics were recorded; time to complete task, time the ring is in contact with the wire (error time), and the number of times the wire and ring contact (number of errors). These error metrics are similar to those used in a number of previous user studies in which users were asked to use two or more tools for the purpose of comparison [5] [72].

Users were also asked subjective questions regarding their test experience. Two questions asked the users to rank the tools in terms of favorite to least favorite in terms of ease of use and learning curve. The third question was open ended asking for general feedback, impressions and comments.

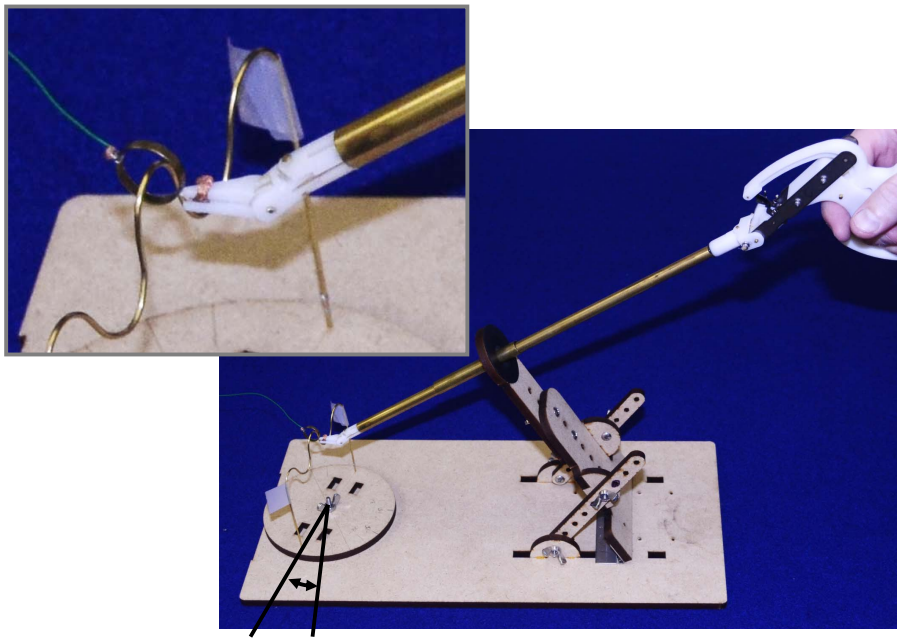

Figure 3.13: Sinusoidal traverse test. Moving the ring along the sinusoidal path simulates the trajectory needed to place a pair of in-line sutures. The longitudinal axis of the wire frame is place at $\pm 15^{\circ}$ with respect to the test stand (see indicated angle).

3.5.2 Test Participants

A total of 18 participants were recruited for this study. Test participants were evenly drawn from two sample bodies, practicing surgeons and a naive user group with no surgical training. The training of the surgeon population means they are expected to be more familiar with the general skills needed to perform these tasks. The naive group with no prior training are expected to be slower at each task but have no inherent experiential bias.

3.5.3 Test Tools

A set of four tools were constructed for this user study. The tools, pictured in Figure 3.15, are intended to represent three user control designs and two wrist control

mappings. Based on the survey of existing tools (Section 3.2.1) a pistol grip and hemostat grip were obvious test choices. All of the research tools used a parallel mapping and two of the three used a hemostat type interface. The hemostat based tool (A) is parallel mapped and meant to represent these tools. Two of the three commercial tools use anti-parallel mapped pistol grips. This layout is represented in the pistol grip tool (C) with an anti-parallel mapping.

The remaining two tools are based on a new user interface (Figure 3.14). Section 3.3 postulated that a natural handle design would enable the user to readily isolate rotational and translational movements. The Cross Correlation values are an attempt to quantify this effect. The close relationship between the center of the user grasp and the handle joints which control the distal wrist minimizes the Cross Correlation and is expected to produce superior naturalness as compared to the other test tools. Two versions of the prototype tool were created, the parallel mapped version (tool B) and the anti-parallel mapped version (tool D). The details of the mechanical design of this interface will be described in greater detail in Chapter 4.

With the four tools, the relative performance of both the handles and parallel vs anti-parallel mappings can be considered. The prototype tools (B and D) are identical other than the parallel and anti-parallel mapping. They offer a direct comparison of the wrist mapping. The hemostat tool (A) and the prototype parallel mapped tool (B) have the same wrist control mapping but different handles. The pistol grip tool (C) and the anti-parallel prototype tool (D) offer a similar comparison. Thus the performance of the hemostat vs. prototype handle and pistol grip vs. prototype handle can be compared directly. Comparisons of tool A (hemostat) vs. tool C (pistol) involve

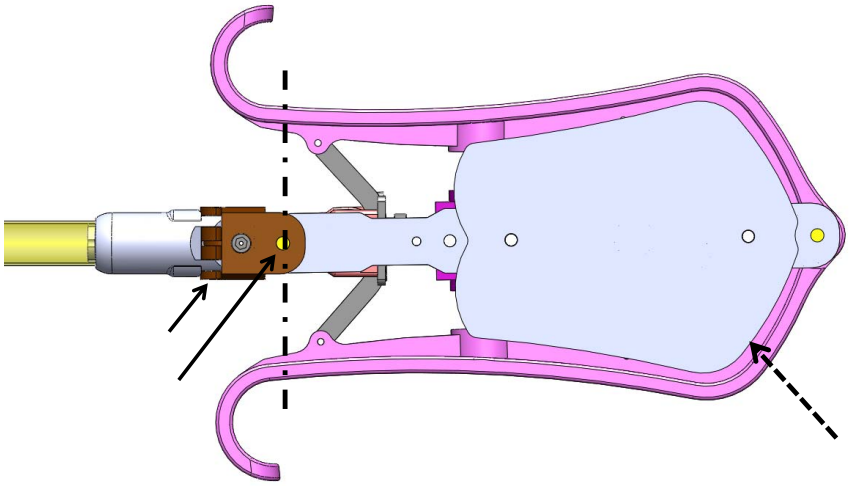

Figure 3.14: The prototype tool interface places the line of grasp of the thumb and forefinger (indicated by the dashed line) around the handle's wrist joint. The two wrist axes are indicated by the solid arrows. The grasper jaws are closed by squeezing the opposed handles. The flat side plates (dashed arrow) allow the user to stabilize the base of the handle between the palm and 3rd and 4th fingers.

Tool	**Joint Mapping**	**Average Cross Correlation values**
A - Hemostat	Parallel	65.60 mm/rad
B - Prototype	Parallel	25.11 mm/rad
C - Pistol	Anti-Parallel	132.5 mm/rad
D - Prototype	Anti-Parallel	36.57 mm/rad

Table 3.2: Test Tool Cross Correlation values. The tools are listed in the order pictured in Figure 3.15.

the changing of two variables. However, inferences regarding the relative performance of the two can still be made via the two prototype tools (B and D) due to the common handle design.

The Cross Correlation Norm was calculated for each example tool and the results are shown in Table 3.2. Note that tools B and D differ due to the parallel vs anti-parallel mapping.

Figure 3.15: Pictured are the tools constructed for the user study. The tools are described from top to bottom. **Hemostat tool (A)**: Parallel mapped with a hemostat type interface. This test tool is similar to the EasyGrasp and DragonFlex research tools. **Prototype tool B**: Parallel mapped with a user handle intended to co-locate the proximal wrist control joint and the virtual reference frame of the hand (the point of grasp of the first finger and thumb). **Pistol grip tool (C)**: Anti-parallel mapped tool with pistol grip type interface. This test tool is similar to the commercial RealHand and CambridgeEndo tools. **Prototype tool D**: Anti-parallel mapped version of tool B.

Tool	Relative Performance, All Metrics	Average Placement in User Preference	Cross Correlation	Jacobian Inversion
D:Prototype, anti-paral.	74.8%	1.41	36.57	No
B: Prototype, Parallel	85.4%	2.06	25.11	Yes
A: Hemostat	101.9%	3.19	65.60	Yes
C: Pistol	137.9%	3.34	135.50	No

Figure 3.16: Result of user study sorted by qualitative user study performance (best to worst). The average placement in the user study is the subjective ranking of the tools by the test participants. Tools are ranked 1 to 4. The average ranking for each tool is reported in the table.

3.5.4 Test Results

The prototype tool with the anti-parallel mapping had the overall best performance. The parallel mapped tool was second overall. The hemostat based tool ranked third and the pistol grip design had the lowest performance. The consolidated results can be seen in Figure 3.16. The data in this Figure is based on relative performance of each tool as compared to the performance of all tools. The difference in average performance of each tool was shown to be statistically significant. The statistical differences between the mean performance of the tools and a breakdown of mean performance for each of the three metrics recorded during the study (Time to complete task, Error time, Number of Errors) is shown in Figure 3.17. This more detailed breakdown shows a statistical performance difference in 16 of 18 tool comparisons. Two user data sets (one surgeon, one naive user) were excluded from the results because the participants were unable to complete the study due for unrelated reasons, thus the final data set has 16 participants. The overall tool rankings are unchanged when the data is separated into surgeons and naive users groups. The complete raw data set and a statistical reduction is located in Appendix A.

	All Tests, All Metric	All Tests per Metric		
Tool	% of All Metrics	% of Avg Time	% of Avg Error Time	% ofAvg # of Errors
A: Hemostat	**101.9%**	**104.7%**	**105.8%**	**95.1%**
B: Prototype, Parallel	**85.4%**	**95.4%**	**74.0%**	**94.3%**
C: Pistol	**137.9%**	**109.5%**	**159.1%**	**134.2%**
D:Prototype, anti-paral.	**74.8%**	**90.4%**	**67.0%**	**78.6%**
t-Values, Tool Comparisons				
t-A:C	7.56	4.18	3.37	6.08
t-B:C	12.52	13.30	6.60	6.40
t-D:C	15.35	19.84	7.23	9.42
t-B:A	5.51	9.02	3.05	~~0.21~~
t-D:A	9.41	15.32	3.80	4.60
t-D:B	5.93	5.92	~~1.56~~	4.85

Figure 3.17: Overall tool performance. The top half of the figure is relative performance of the various tools. The percentages indicate the performance of a specific tool vs. the average of all tools for that metric. The left half of the table shows the fully consolidated data. The right half separates data into relative measures of time to complete task, time in error (ring contacting the wire) and percentage of the average number of errors. Six t-values are shown at the bottom of each column, one for each pairing of tools (Tool A vs B for example). A t-value greater than 1.65 (or less than -1.65) indicates a 95% confidence the true mean performance of a pair of tools are different.

3.5.5 Discussion of User Study Results

The results of this user study support the merit of the Cross Correlation values as a measure of relative naturalness. The results also support the hypothesis that inversions of the diagonal elements of the handle to grasper Jacobian should be avoided when possible.

The relative performance of the prototype handle design, a design first proposed as part of this work, is illustrated by comparing the two anti-parallel mapped tools (D and C) and the two parallel map designs (A and B). In both comparisons the prototype handle design had superior performance. This was especially evident in the comparison of the prototype handle with anti-parallel mapping, the top ranked tool, vs. the last ranked pistol grip tool (anti-parallel mapped). A comparison of the parallel mapped tools (Prototype (B) and Hemostat (A)) shows a smaller difference in overall performance as well as a smaller difference in the Cross Correlation values.

The quantitative performance results were supported by the user preference rankings. The description, 'more stable' was used to describe the proposed handles (B,D) in 5 of the 20 opened ended user feedback comments.

The relative performance of the prototype tools (B and D) supports the theory that inversions of the diagonal elements of the Jacobian should be avoided. Though the Cross Correlation value of the parallel mapped tool (B) was lower, the anti-parallel tool (D), the one with the non-inverting Jacobian, tool performed better in both measured performance and user preference.

The pistol grip was noted for requiring a large range of upper body movement

since the handle design does not support multiple user hand holds as well as the other designs. Rotation of the tool about its main shaft requires full rotation of the operator's wrist as the tool can not be readily rotated within the hand. It should be noted that the RealHand and CambridgeEndo tools offer a finger controlled wheel to rotate their main shaft with respect to the handle. One surgeon commented that the hemostat grip (A), a design proposed in tools by Awtar et al. and Jelinek et al. [8] [47], offered the largest range of ways to hold the tool but found those alternative holds were not easier to control vs. the prototype handle design.

A significant finding is that despite the significantly different approaches taken by the commercial and research tools (RealHand, CambridgeEndo, Awtar et al. and Jelinek et al.) each group had partial answers for the question of natural motion. The reverse mapping of the commercial devices performed better when the two prototype tools were compared (B vs. D) but the test tool based on the research design had significantly better performance and a lower Cross Correlation value.

The overall results of the study support the validity of both the Cross Correlation value as a metric of comparison as well as the impact of inversions of the diagonal elements of the Jacobian. The relative importance of the inversion vs. the Cross Correlation has not been established based on these performance results.

3.6 Conclusions

To realize the benefits of dexterous, image-guided surgery without automation, dexterous, manual tools with a natural control interface are required. At the beginning of this work it was felt that the existing commercial and research tools could be im-

proved with a focus on the naturalness of the user interface. The results of the user study illustrate that the naturalness metric and guideline of this chapter can improve the design of the user interfaces.

The first contribution of this chapter was the proposal of a Jacobian-based metric and a deign guideline for user interface naturalness. The first theory uses the Cross Correlation value as a metric for natural motion and movement between the user interface and the grasper end of the tool. A method to calculate this metric was outlined and the Cross Correlation values of several tools in literature as well as a set of user study tools were calculated. The second Jacobian-based design guideline theorized that the diagonal elements of the tool Jacobian should not invert as the tool is moved over the workspace.

Both of these theories were applied to the design of a prototype natural user interface and mapping for a new manual, dexterous tool. This prototype interface design, the second contribution of this chapter, places the grasp of the thumb and forefinger around the wrist of the tool's handle. This reduces the Cross Correlation value of the tools design. Versions of this handle with parallel and anti-parallel mapping between the user control and grasper wrist were created to validate the theory on inverting the diagonal elements of the Jacobian.

In order to test the validity of the first contribution, a complete set of test tools were constructed. In addition to the two with the prototype handle design, one tool was made to represent high dexterity tools that have appeared in research. Yet another tool was created to represent the pistol grip based tools seen in industry. With these four tools the third contribution of this chapter, a comparative user study, was

conducted. The results of the user study confirmed that the Cross Correlation value and avoiding inversions of the diagonal elements of the Jacobian are both positively correlated with tool performance. The user study also confirmed the validity of the prototype user handle as compared to the existing designs found in the literature.

With the contributions above it is possible to create more natural manual tools, thus moving closer to the overall objective of image guided, dexterous surgery without the need for automation.

Chapter 4

Design of a Dexterous Manual Manipulator for Throat Surgery

One of the great advantages of current surgical robots is the ability to place sutures in difficult-to-access locations of the body. As discussed in Chapter 3, appropriately designed dexterous manual tools have the potential to provide similar advantages, while doing so at a low cost compared to a surgical robot. To illustrate more specifically how this can be achieved, in this chapter, the principles discussed in the previous chapter are applied to the design of an articulated manual tool for throat surgery (Figure 4.1). One important application of such a tool is suturing in the area around the larynx and vocal folds.

The current surgical practice for suturing in the upper airway including the region around the vocal folds is based on methods developed starting in the 1960s with the introduction of improved binocular microscopes and associated tools for laryngeal work [51] [29] [45]. These tools and methods, while an improvement over those prior, still had a number of limitations. Access to the surgical site is via a straight, rigid laryngoscope with rigid tools and results in a very limited range of motion (Figure 4.2).

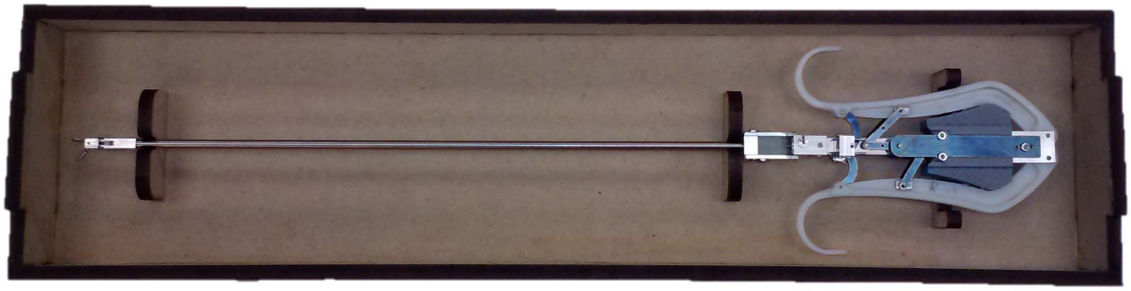

Figure 4.1: Prototype dexterous manipulator.

Figure 4.2: Examples of contemporary Kleinsessar laryngoscope and micro grasper tool.

Suturing and knot tying are particularly difficult in this area. Though the basic techniques used in current throat procedures were developed in the 1960s and 1970s, a "best practice" for suturing in the throat has arguably not been firmly established. In 1995 Woo et al. noted the critical nature of the quality of wound closure when working on the vocal folds [108]. They also described the practice of tying the surgical knot external to the laryngoscope and then sliding the knot down to the surgical site. This practice is a reflection of the difficulty of actually performing the suture inside of the throat. In 2009 Tsuji proposed another method for addressing the difficulty of suturing in the throat [102]. The contribution of Tsuji's method was a complete suture, throwing and tying, inside of the throat. Thus, four decades after the introduction of micro-surgical methods for the throat, the difficulty of suturing

is still of interest and new methods to address the limitations of access and dexterity are still being explored.

The potential benefits of reaching this surgical site with high dexterity tools have been considered by a number of medical and engineering research groups. McLeod described a test case using the da Vinci Surgical System. The da Vinci system, well suited for abdominal use, is less suited for the anatomical constraints present in otolaryngology [62]. Only one arm was used in the throat due to the fact that da Vinci arms were designed for procedures that require triangulation in the chest or abdomen. Attempts to apply the da Vinci system to the throat have been tried but with limited success [79] [71].

A robotic system specifically designed for dexterous tasks in the upper airway has been described by Hillel et al. and Simaan et al. [42] [89]. Here the large, widely spaced arms of the da Vinci robot are replaced with 4 mm flexure-based arms. This system addresses the size and arm placement issues associated with the da Vinci system and demonstrates the potential advantages of added dexterity in the upper airway.

All the above attempts to apply high dexterity manipulators to the throat have relied on some level of automation. The novel contributions of this chapter are (1) the first example of a manual dexterous tool specifically designed for throat surgery of which the author is aware, and (2) the application of the novel user interface described in the previous chapter to a tool scaled for use in the throat, and (3) this is the first example of the use of the cross correlation metric described in Chapter 3 in the design of a manual laparoscopic tool.

The chapter starts with a general description of the physical constraints associated with surgery in the throat. The general mechanical structure of the tool is then described and cable routing through the proximal and distal wrists (which does not affect the kinematics of the tool) is optimized. Next, instrument kinematics is optimized for both the workspace (which affects only distal wrist and grasper dimensions), and user interface naturalness, which will be used to optimize dimensions of the external wrist located near the user's hand.

4.1 Throat Workspace and Suturing Requirements

The fundamental difficulty with suturing in the throat is the limited access provided to the surgeon via a straight, rigid laryngoscope. The laryngoscopes typically range in length from 130 to 170 mm with openings ranging from 13.5 to 19 mm at the distal end and 15-30 mm at the proximal end (Storz Kleinsasser laryngoscopes [3]). The small diameter of the laryngoscope and its relatively long length place a premium on the diameter of the tool shaft as it passes through the laryngoscope. A large diameter tool shaft limits the range of motion of the tool as well as blocks the view of the surgical worksite from the external microscope. An ideal manual tool for this task would thus need to minimize both the size of the distal grasper and wrist and the diameter of the main tool shaft which passes through the laryngoscope.

The shape of the larynx is irregular and varies in size between individuals and sexes. Kim et al. performed a series of measurements on 9 male and 7 female cadaver samples [50]. The overall height of the thyroid cartilage for adult males was approximately 45 mm with a width of approximately 41 mm. Simaan et al. modeled the

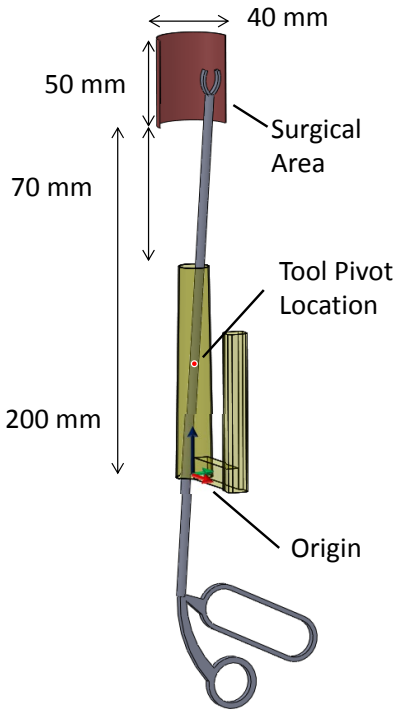

Figure 4.3: Model of the workspace. The surgical tool passes through a laryngoscope to access the surgical space. A pivot point in the laryngoscope tube provides support for the dexterous tools. The origin for plots in this chapter is located at the base of the laryngoscope.

surgical space as cylindrical with a 50 mm height and 40 mm diameter [89]. This cylinder is located 70 mm from the distal end of the laryngoscope. For the purpose of the design optimization described in Section 4.3, general laryngoscope dimensions were assumed. The proximal and distal openings of the laryngoscope were assumed to be 16 mm and 20 mm respectively. The length of the laryngoscope was assumed to be 130 mm. These dimensions are similar to the Storz Kleinsasser laryngoscope model 8590A. The general configuration of the workspace used in our modeling is illustrated in Figure 4.3.

A number of papers have investigated needle suturing. These include range of motion studies [20], and path planing for driving needles [69]. The basic surgical

needle is an circular in shape with an arc that is typically 1/2 or 3/8 of the full circle. The diameter can vary with application. For throat applications the Ethicon G-2 1/2 circle 8 mm suture needle is representative of the needles used in the throat. To reduce trauma to the surrounding tissue, a circularly curved needle should be moved in a purely circular path as it passes through the tissue. This is an established movement for robotic path planning [48] and it along with the G-2 1/2 circle 8 mm needle will be assumed in the later optimizations of the wrist and jaws.

4.2 Tool Concept and Cable Routing Strategy

The prototype tool that is the subject of this chapter is shown in Figure 4.1. It uses a cable actuated design with a 4 mm main shaft and a grasper diameter of 6 mm. The distal wrist and grasper are of the finger-wrist design (Figure 4.4). This was done to minimize the working length of the wrist and jaws. The wrist allows an articulation of $\pm 90^\circ$ about the axis of the jaws and $\pm 45^\circ$ about the perpendicular wrist axis.

Six cables are used to operate the wrist and grasper jaws. Because these cables operate capstan (pulley) driven jaws which also articulate with wrist motion, maintaining tension on the cables is critical for wrist function. The optimization of the cable routing is described in Section 4.2.1.

The handle design, illustrated in Figure 4.5, functions similar to a pair of tweezers where the grasping point of the tweezers is about the proximal wrist of the tool. It is top-bottom symmetric, which allows the handle to be rolled in the hand (along the main axis of the tool). Left-right symmetry allows the tool to be used equally effectively in either hand and negates the possible need for left and right handed

Figure 4.4: Types of Wrists: Grasper plus wrist (left), finger-wrist (right). The grasper mechanism of the grasper plus wrist design is mechanically independent of the wrist mechanism. The cables which articulate the wrist are independent of those which operate the grasp. In the finger-wrist design the coordinated movements of the fingers (both up, both down) provide a wrist DOF. The cables which open and close the grasp also operate a wrist DOF. (Intuitive Surgical EndoWrists used as examples)

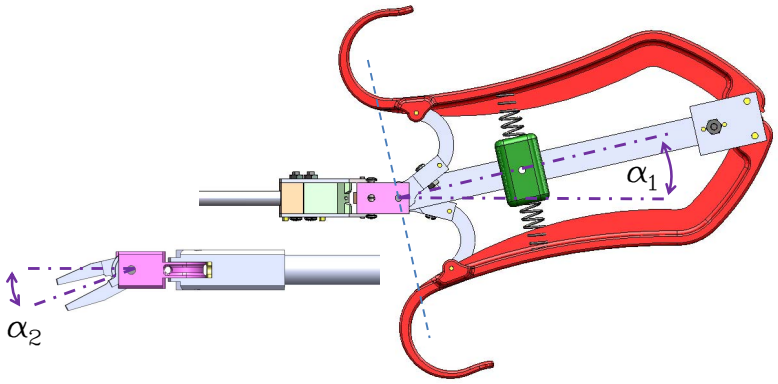

Figure 4.5: Detail of gripper and user interface. The ratio of α_1 to α_2 is 1:1.6. The forward features of the handles extend past the pivot which controls the finger joints.

versions. The motion of the wrist is parallel mapped (Chapter 3, Figure 3.3) to the proximal wrist of the tool. In the previous user study (Chapter 3, Section 3.5.5) the anti-parallel mapping was shown to be superior with this tool layout. The parallel mapping was chosen because it was felt the anti-parallel mapping would result in the control handle interfering with the surgeon's view down the laryngoscope. The design of the tool does allow for an anti-parallel configuration with minimal changes.

A design choice was also made to scale the motion of the grasper jaws with respect to the handle. This was done on account of the $\pm 90^{\circ}$ range of motion of the jaws. In some instances the wrist of the surgeon may reach the limits of comfortable articulation before the jaws reach their articulation limit. Scaling the size of the capstans which drive the distal jaws results in a motion ratio of 1:1.6 (handle:finger). Angles involved in this ratio are illustrated in Figure 4.5.

4.2.1 Cable Routing

The cables themselves were 0.46mm 7×7 stainless steal, non-coated wire rope. A 7×19 cable of the same diameter would be preferred for its extra flexibility but was not readily available.

The design and routing of the finger control cables through the wrist (Figure 4.6) requires special consideration in order to maintain tension on the cables as the wrist is articulated. To reduce the size of the wrist assembly, the cables pass from the main shaft through the wrist to the fingers via guide channels on either side of the first wrist joint. As the first wrist joint articulates, the path length of the cable through the guide channel changes (Figure 4.8). This results in a decrease in the total cable

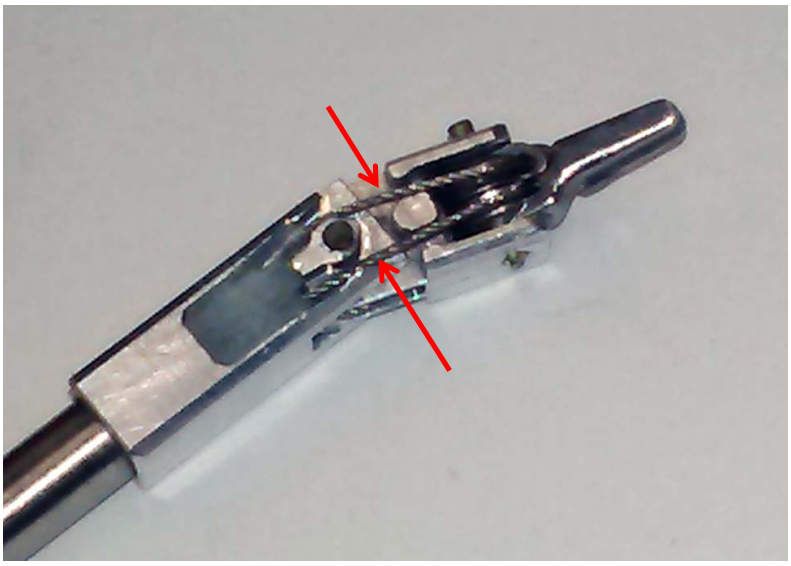

Figure 4.6: Routing of the finger control cables through the wrist. Cables are indicated by arrows.

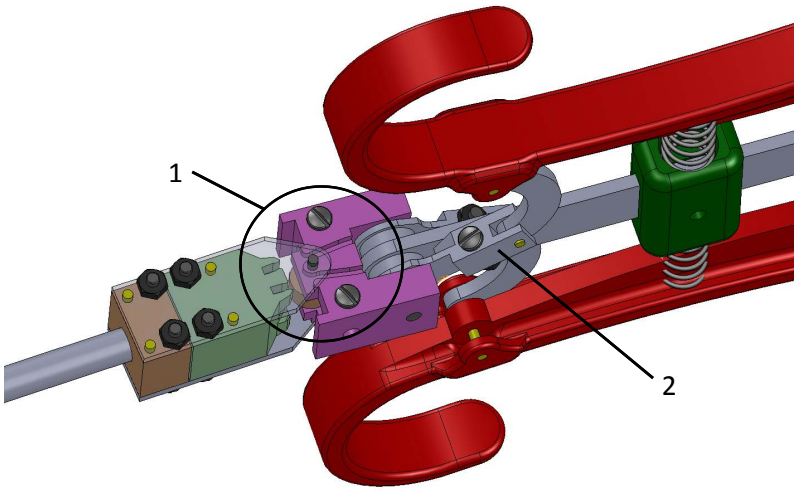

Figure 4.7: Detail of the proximal mechanism which drives the control cables. 1. Cable paths which mirror those in the distal wrist. 2. The pulley arms which drive the finger cables and are connected to the handles via an intermittent link. The cables are not shown in this CAD model.

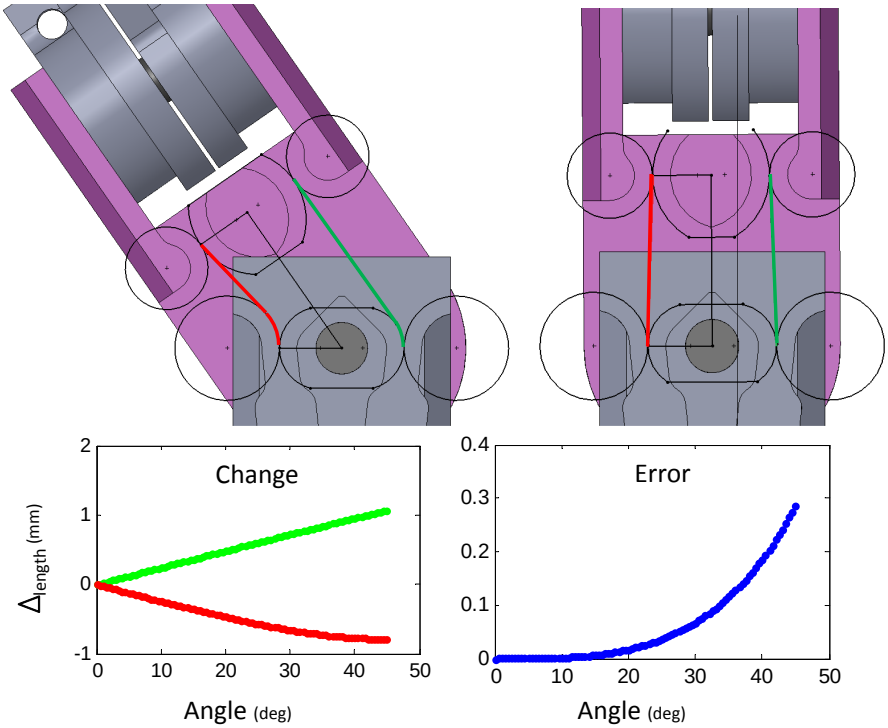

Figure 4.8: Finger control cable routing through the wrist. The red and green paths represent the center line of the finger control cables as they pass through the wrist. The black circles are projections of the curved guides which pass the cable through the wrist. The cable is sized such that the center line of the cable should remain in contact with the guide edges. During articulation the cable paths between the wrist joint and fingers changes. The 'Change' plot represents the increase or decrease in the length of the green and red cables as the joint is articulated. Ideally the change increase in length of one path matches the decrease in the other. The 'Error' plot represents the difference between the increase and decrease in lengths as a function of angle.

path length for the cable pair used to drive one finger while increasing the length for the other. A mirror image mechanism in the user control end of the tool compensates for this change in path length (Figure 4.7).

In the ideal case, the increase in length of one cable path would be equal to the decrease in the other. If the joint is designed with parallel cables when the wrist is straight the deviation from the ideal case during articulation can be significant (Figure 4.8 'Error'). This will change the cable preload tension and thus should be avoided.

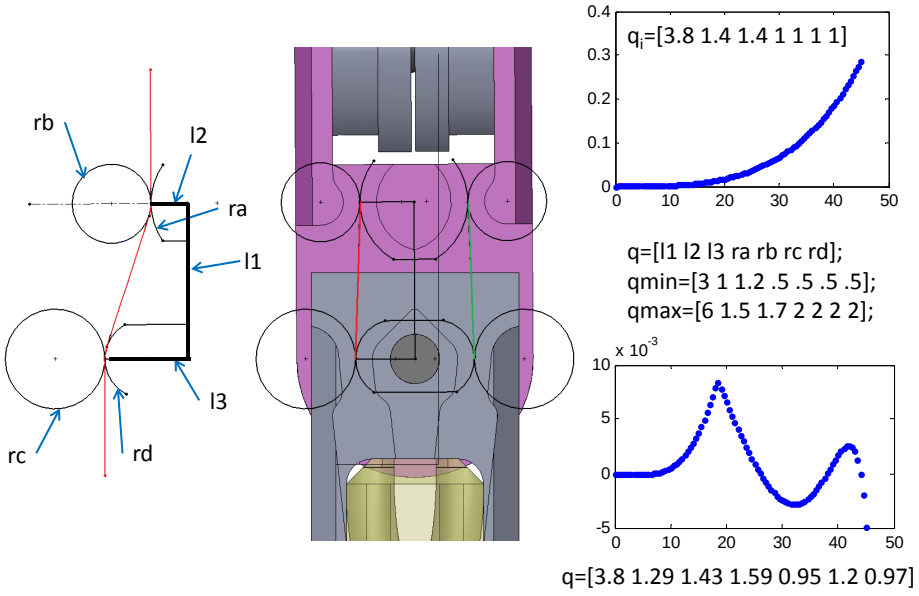

Figure 4.9: Finger control cable setup and optimization. The path length of each cable is defined by the diagram (right). The path length is controlled by 7 variables (illustrated-left, values-right). The initial guess plot (upper right) shows the error performance using the initial values of q. The location of each geometric variable in q and the upper and lower bounds are shown middle right. The final value plot (lower right) shows the error performance after optimization.

To reduce the deviation, the cable paths were optimized. The joint geometry was constructed as eight arcs representing the curved surfaces where the two cables exit the main shaft and enter the wrist. The spacing of the cables with respect to the tool center line, the distance the cables spanned and the radius of the curved surfaces were optimized using Matlab's `fmincon` function. The specific geometric variables that were optimized, their respective upper and lower bounds and the performance results of the optimization are shown in Figure 4.9. The objective function was to minimize the average difference in cable length change over 0-45°. Prior to optimization the deviation was 0.04 mm. This was reduced to a peak deviation of less than 0.01 mm.

4.3 Optimization of Grasper for Suturing in a Confined Workspace

The intended purpose of this prototype tool is placing sutures inside of the throat. The process to perform this optimization requires several items. The first is a geometric description of a suture. This description will describe the ideal path a suture needle would follow to place a single stitch (Section 4.3.1). This description of the ideal suture path will be used to define the path the grasper must follow in order to place a suture.

In order for the tool to follow a needle path, a relationship between the grasper and needle, a grasping pose, is created as the third step in this process (Section 4.3.2). With the relationship between grasper pose and needle path established, the workspace can be discretized into a finite number of needle paths which the tool will try to follow (Section 4.3.3).

Not every desired grasper pose will be reachable with the actual surgical tool.

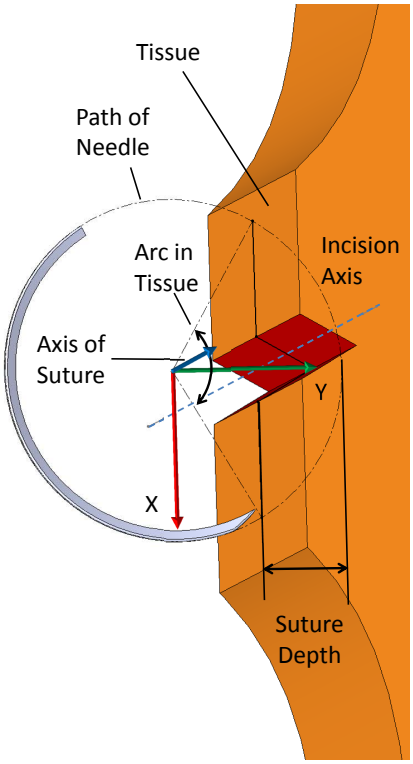

Figure 4.10: Geometry of the suture with respect to the incision.

Some poses can only be reached if the tool exceeds its joint limits or has a collision with a workspace boundary. Thus a method for identifying suture paths which can or cannot be reached by the tool is the fourth step of the optimization (Section 4.3.4). The final step of the optimization is creating an objective function based on minimizing the number of suture paths the tool was unable to complete vs the total family of target sutures (Section 4.3.5).

4.3.1 Description of the Suture Path

In Section 4.1 the surgical workspace and suturing task were described. An ideal suture path should follow the curvature of the needle, be perpendicular to the axis of the incision and have a consistent suture depth. Because the ideal suture path

is circular, the depth of the stitch and the angle of the needle arc in the tissue will be related. Figure 4.10 illustrates the needle path with respect to an incision. The needle diameter used for this optimization will be 8 mm.

Based on the above, the circular arc traced by the needle in space as it is rotated about its central axis is the suture path. Figure 4.10 illustrates a coordinate frame located at the center of the needle's arc. The axis around which the needle will rotate is indicated. Thus the path of the needle can be described by the center of its arc and a rotational axis.

4.3.2 Suture Path to Grasper Pose

In order to test the ability of the grasper to throw sutures over the surgical space a method for defining the location and orientation of a particular suture path must be established. This will allow a large number of suture paths to be discretized in the workspace. From one of these suture paths a series of target grasp poses can also be discretized.

Using the requirements for a circular suture path that is oriented with respect to an incision axis, the path through which the tool must move the needle in space is defined. For an individual incision, the suture path will have a starting point (the pose of the grasper at the start of the suture), and an end point (the pose of the grasper upon completion of the suture), and portion of the suture path through which the grasper will not pass (the portion of the suture path in tissue). This suggests the need to explicitly define a start point and an end point for the movement of the grasper around the suture path.

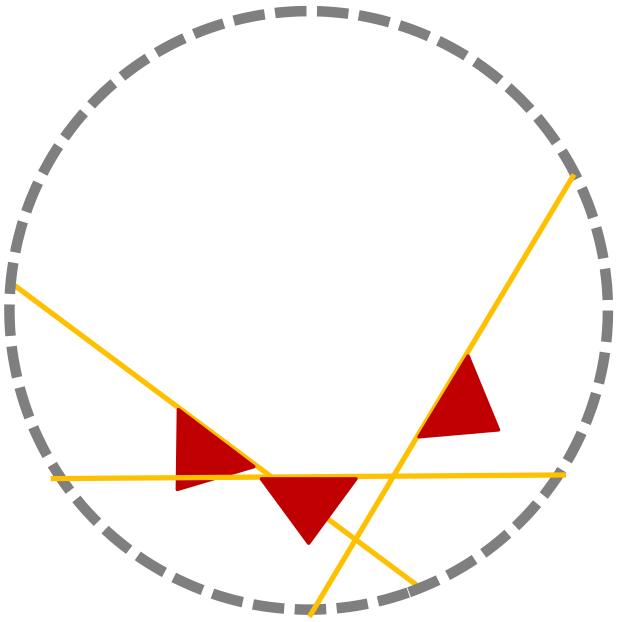

Figure 4.11: Illustration of a family of incisions sharing a common suture path. A suture path is indicated by the dashed circle. Three possible incisions that could be closed by the suture path are indicated.

However, a single suture path represents a family of possible incisions which all share a common suture axis (Figure 4.11). These possible incisions are located 360° around the suture axis. The ability to move the grasper through a series of poses around the suture path indicates an ability to suture the family of incisions that would share a common suture axis. Thus a specific starting and finish location for a given incision location will overlap with the path the tool must traverse to place a suture for another incision that shares the common suture path associated with the same suture axis.

From here it is a small logical step to the idea that rather than discretizing in terms of possible incisions, the workspace can be discretized in terms of suture paths. The orientation of the suture path thus can be used to express the orientation of the incision itself and will later be the basis for testing the limits of a tools workspace.

The orientation of any needle path in the workspace can be expressed as a coordinate frame located at the center of the needle's arc with the Z axis of the frame normal to the plane of the arc. Thus the Z-axis is parallel to the incision axis and the positive Y axis is normal to and pointed towards the incision axis (Figure 4.11). If a tool can trace the path needed to move a needle through the suture arc, then that particular suture configuration is part of the tool's usable task space.

It is necessary to express the orientation of the needle arc in terms of the workspace. This is done by defining the center of the needle arc (Figure 4.10) and expressing its orientation using a series of frame transforms similar to the kinematic chain of the surgical grasper. This chain starts with a vector from the tool's entry point to the workspace rather than in terms of the workspace's Cartesian frame. To orient the needle, a reference coordinate frame is placed at the center of the needle arc (Figure 4.12). Its Z-axis is aligned with a vector from the entry point of the tool, a pivot point in the laryngoscope body, to the needle center. The transform from the pivot point to the frame of the vector is as follows: A Z,Y fixed angle rotation followed by a projection along the local Z axis to the needle arc center. A further set of Z,X,Y Euler rotations, the suture angles, orient the suture arc into its final orientation.

With the path of the needle though space defined, the relationship of the needle to the grasper must also be defined. Figure 4.13 illustrates the relationship between the grasper, needle, and suture path. For this work it is assumed there is one ideal needle grasp. The Z-axis of the grasper is aligned with the long axis of the tool's main shaft. The Y-axis of the grasper is normal to the grasping surface. The Z-axis of the grasper is constrained to be parallel to the axis of the suture and the suture

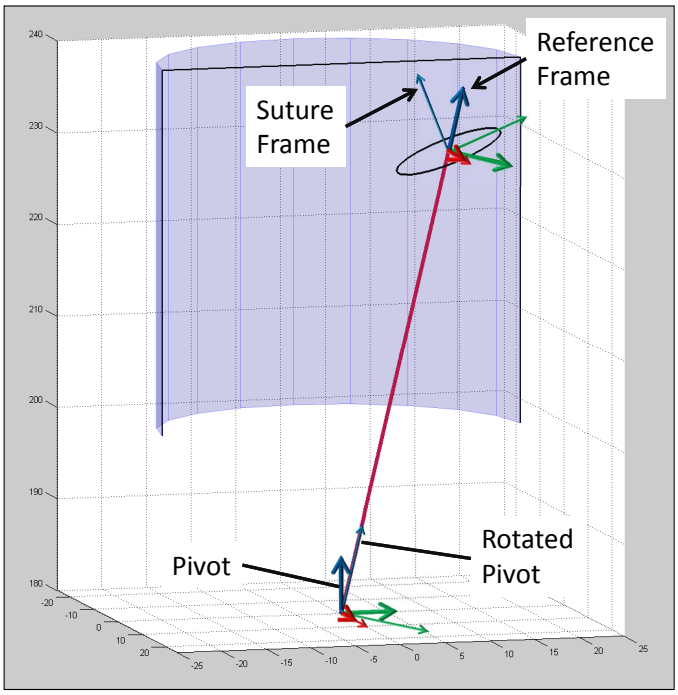

Figure 4.12: Suture orientation inside surgical volume. The half cylinder represents the surgical workspace. The tool would enter from the bottom of the workspace. (Note pivot location is shown closer to the surgical site for illustration purposes. Frame axes are color coded; X red, Y green, Z blue.)

axis. The Y-axis of the grasper is normal to the needle arc and always intersects the suture axis. Thus to throw a stitch the grasper handle revolves about the axis of the needle.

It is understood that limiting the grasper to only a single possible pose between grasper and needle is a restrictive assumption. In actual practice the surgeon can select different needle grasps. Like the assumption of an ideal needle path through tissue this assumption will result in reporting less than actual tool capability.

Because the orientation of the needle to graspers was explicitly defined, the ability of the tool, absent boundary constraints, to throw a suture is fundamentally limited by the ability of the tool to articulate about the needle path. This in turn means

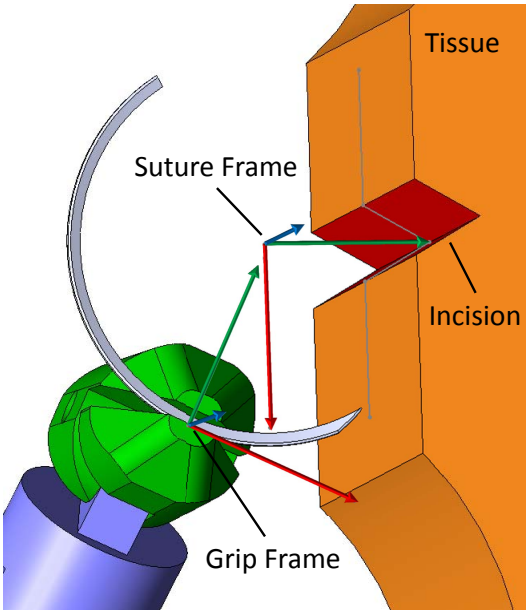

Figure 4.13: An ideal suture grasp. Grasper jaws are normal to the needle arc. Coordinate frames of the needle and grasper are shown. The colors, red, green, and blue correspond to the local frame X, Y and Z axes respectively

that the suture dexterity of the tool can be expressed solely in terms of the range of suture orientation angles the tool can reach at each suture origin.

4.3.3 Discretizing the Working Space

The position and orientation of a suture path in the work space is discretized via four variables. For this analysis the throat is assumed to be cylindrical [89]. This means the workspace is radially symmetric about the Z axis, the axis extending from the laryngoscope into the larynx. The grasper tools are free to rotate about their main shaft axis inside of the laryngoscope. Thus, for any radial plane of the workspace the tool has an equal workspace.

With this radially symmetric assumption, any point in 3D space [X Y Z] can be expressed as a [Y Z] pair. Because this analysis is general, an even distribution of

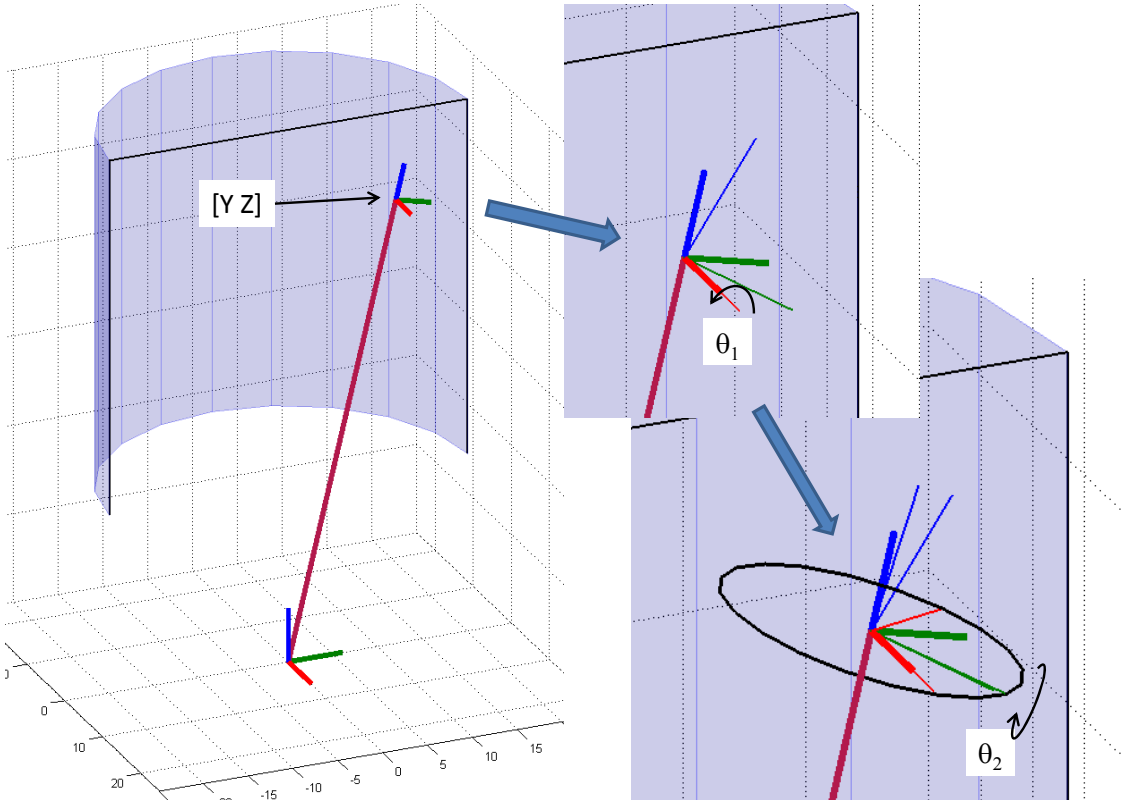

Figure 4.14: Variables used to discretize suture path positions and orientations. The origin of the suture path is located in [Y Z] space. A local reference frame is created at the [Y Z] point. The Z axis of the local frame is aligned with a vector from the tool pivot point (bottom of frame) and the reference frame X axis is parallel to the X axis of the workspace. An XY Euler rotation starting from the reference frame orients the suture path. The X and Y rotations are labeled θ_1 and θ_2 respectively. (Axis colors: X-Red, Y-Green, Z-Blue)

points across the [Y Z] space is used. If a specific portion of the surgical volume is more task critical a weighted or uneven distribution of test points could be used.

With a series of [Y Z] points defining the location of the suture paths established, the possible orientations of the suture paths is discretized as follows. Section 4.3.2 describes the location of a suture path in reference to the pivot point of the surgical tool. The orientation of a suture path is defined by an XY Euler rotations starting from the reference frame (the frame located at the [Y Z] point). Thus the range of possible orientations is discretized by two location variables [Y Z] and two rotation

variables [θ_1 θ_2] (Figure 4.14).

4.3.4 Inverse Kinematics and Collision Detection

With the discretization of the surgical space completed, a large number of individual target poses have been defined. The ability of the tool to reach these poses is now tested using the method below. This method has two parts. First, using the inverse kinematics of the tool, the grasper is fitted to the discretized grasp positions around the path of the needle. Second, the resulting tool pose is tested for intersections with the workspace boundaries as well as exceeding the tool's joint limits.

The inverse kinematic solution was found using a resolved rates method [24]. The resolved rates method is sensitive to an initial guess pose. The grasper pose is defined by a set of transforms starting at the same origin as the surgical tool (the pivot in Figure 4.12). The series of rotations used to define the suture axis and grasper pose are defined in a method that is similar to the physical structure of the tool. For a given desired pose, the initial guess of tool joint angles can be derived from the suture pose angles.

The relationship between suture pose and guessed joint angles of the grasper, $\hat{\boldsymbol{q}}$, is expressed in Equation 4.1. The first 3 terms represent the 3 DOF rotations of the tool's main shaft. The 4th term is the projection of the tool into the body. The last two are the wrist angles. Figure 4.15 illustrates both the family of poses for a tool

following a needle path as well as the associated family of guess poses.

n_s : Vector normal to the suture arc

θ : Angle between n_s and the world Z-axis

ϕ : Rotation of n_s in the world X-Y plane

γ_z : The location of the grip about the suture's Z axis

z_{ws} : The Z height of the lower edge of the surgical space

$$\begin{aligned}
\hat{\boldsymbol{q}}(1) &= \theta_z \\
\hat{\boldsymbol{q}}(2) &= 0 \\
\hat{\boldsymbol{q}}(3) &= 0 \\
\hat{\boldsymbol{q}}(4) &= z_{ws} \\
\hat{\boldsymbol{q}}(5) &= \sin(\phi + \gamma_z)\theta \\
\hat{\boldsymbol{q}}(6) &= \cos(\phi + \gamma_z)\theta
\end{aligned} \tag{4.1}$$

Once the inverse kinematics has placed the tool at the target pose, the joint angles are checked against the limits of the proposed design. If any joint limits are exceeded the tool fails that particular grasp pose.

The method for checking for boundary collisions between the tool and the workspace consists of two sub tasks. The first is to check for collisions between the main shaft of the tool and the laryngoscope. The second is to check for collisions with the surgical space.

The test for a collision with the laryngoscope starts with the assumption that for

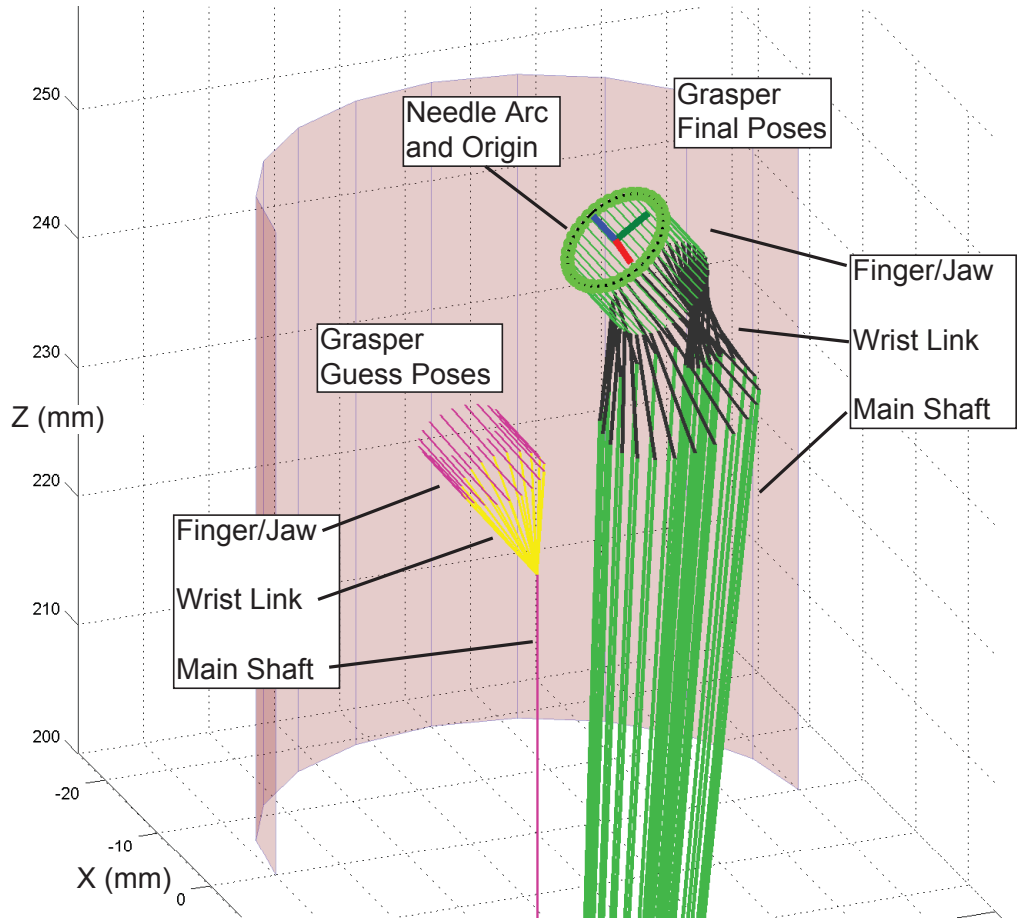

Figure 4.15: Guess and Final Poses: The final poses of a prototype tool as it traces around a needle path. The local orientation of the suture axis is shown with the red, green and blue axes indicating the local X, Y, and Z. The lavender and yellow lines represent the family of guess poses corresponding to the family of final poses shown. All units are in mm. The half cylinder represents the surgical space boundary split along the world.

our task only the main shaft of the tool will be within the laryngoscope during use. Given the known geometry of the main shaft and laryngoscope, collision detection is reduced to an inequality test.

- Using the equation of a circle in a plane, equations describing the entry and exit ports of the laryngoscope are created. If we assume the entry port is centered along the task space's central axis and we compensate for the diameter of the tool shaft, r is reduced by 1/2 the tool shaft's diameter:

$$ax^2 + ay^2 = (r - \frac{d}{2})^2 \tag{4.2}$$

- The 3D parametric equation of a line along the main shaft can be found from the known locations of the tool pivot and the location of the first joint from the inverse kinematic solution. Using the equation of the X and Y values of a point along the line of the tool shaft and the Z-axis position of the laryngoscope opening, a point on the line at the plane of the laryngoscope opening is found. When substituted into equation 4.2 it can be determined if the point is within the opening.

  It is noted that this method assumes the tool shaft is close enough to aligned with the laryngoscope to make a small angle assumption needed to make equation 4.2 true. Given the long, narrow shape of the laryngoscope this is a reasonable assumption. Figure 4.16 illustrates this approximation and its associated error.

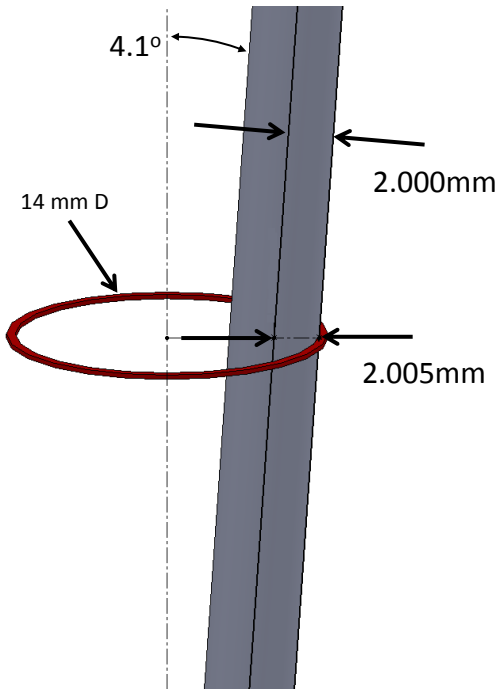

Figure 4.16: Example of the small angle approximation used during the tool shaft boundary check. The opening of the laryngoscope is represented by the ring. The tool's main shaft can be at an angle with respect to the opening. The indicated 4.1° is a realistic angle given a 14 mm opening in a 150 mm long laryngoscope. The described interference test assumes contact between the tool shaft and scope opening occurs when the center line of the scope is exactly 2 mm from the edge of the scope opening. Due to the small angle between the scope and tool shaft the actual contact point in this case would be 2.005 mm. The small angle approximation assumes that the tool shaft is actually aligned with the scope axis rather than up to a few degrees off vertical.

A similar method is used for detecting collisions between the tool and the walls of the surgical space. Because the surgical space is assumed to be cylindrical in shape with smooth walls and the tool links are straight, it is only necessary to check for collisions at the actual joints of the tool. It is impossible for a line segment to pass through a cylindrical surface without one end of the line segment being outside of the cylinder. If both ends of the line segment are within the cylinder the complete line must lie within the cylinder. For this reason, it is impossible for a portion of the tool between two joints to collide with the cylindrical boundary of the workspace without a least one joint colliding or being outside of the workspace. For this reason the workspace collision detection can consider just joint (the endpoints of a line segment) collisions rather than joint and line collisions. The exact shape of the tool joints will vary with design. A characteristic radius is used as a simplified representation of the physical size of the joint. In physical terms, this radius is the distance from the kinematic center of the joint to the physical edge of the tool (Figure 4.17).

- Using the Z value of the location of the joint to be tested, the equation of the circle representing the diameter of the cylindrical surgical space at that Z height of the joint to be tested is determined.

- The characteristic radius of the joint is subtracted from the radius of the surgical space.

- The X-Y location of the joint is tested to see if it lies within the reduced diameter.

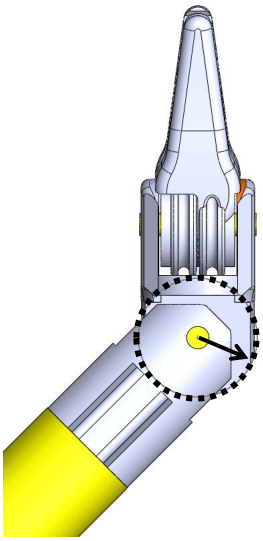

Figure 4.17: Characteristic radius of a joint indicated by arrow and dashed circle.

4.3.5 Objective Functions

Two means for evaluating the success rate for a given tool design at a given suture location are proposed below. Each suture location is the [Y Z] location in the world frame. At that one location a family of suture orientations can be defined as described in Section 4.3.2. Each of the functions below can evaluate the success rate at a single location. The overall success of the tool can be considered over the range of locations in the workspace.

Percent Passed

This performance metric is the ratio of grasper poses attempted at a given location vs. the number of successful poses (poses where tool joint limits were not exceeded and no inferences occurred). Figure 4.18 illustrates forty attempted grasper poses around a suture path. Three of the forty attempted grasp poses failed. This represents a

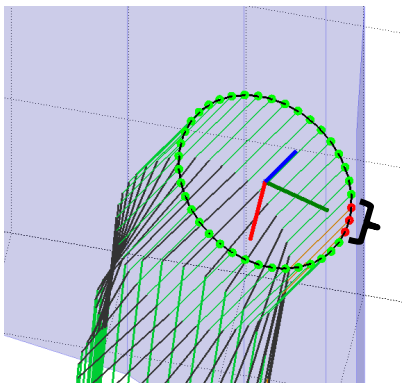

Figure 4.18: 40 grasper poses tested around a suture path. Of the 40 poses, 3 resulted in either the tool exceeding its joint limits or failing a boundary check. This results in a success rate of 92.5%.

success rate of 92.5%. An average success rate for all possible poses can be scored. Alternatively a score based on success rates at a particular [Y Z] location can be used to create a plot of performance over the range of the workspace (Figure 4.23).

Partial Arc

The previously described scoring method discretized the suture arc into a number of discrete poses and then rated the success of the tool based on the ratio of poses it could reach vs total poses in that arc. That method will tend to over score the tool's ability to reach poses. For example if the tool can reach 10 out of 100 discretized points that particular suture pass will have a score of 0.10. However, if the grasper is required to strictly adhere to the needle graps and circular arc defined in Section 4.3.2 then it would be impossible to complete a stitch while only reaching 10% of the poses around the suture path. The Partial Arc scoring method addresses this case by calculating the conditions where the tool can traverse a sufficient portion of the suture path to place a stitch in some orientations but not others. Figure 4.19 illustrates the

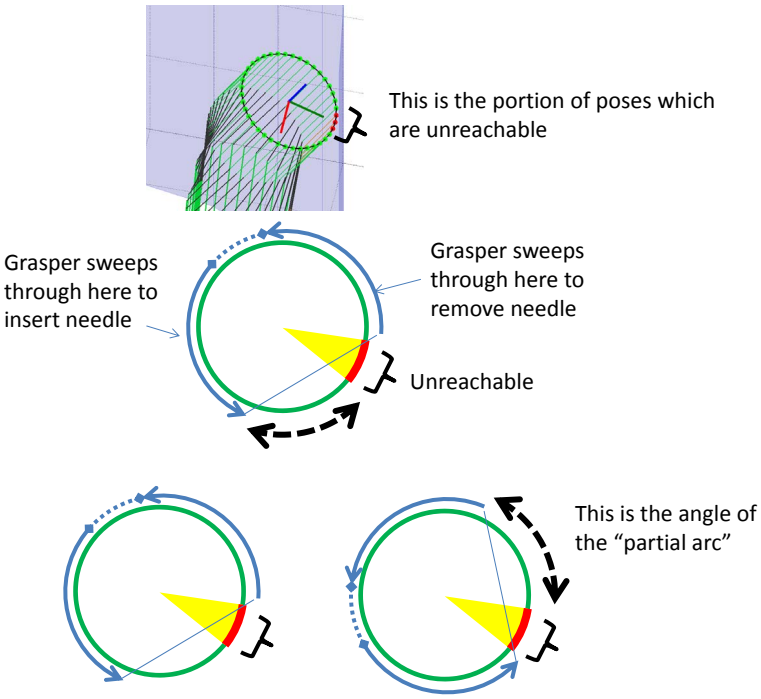

Figure 4.19: Illustration of the range of possible wound locations given an unreachable portion of the suture path. The red-yellow sector represents the portion of the suture path which is unreachable with the tool. The middle figure illustrates the portions of the total suture path through which the grasper will sweep to place a suture at a single wound location. The straight line joining the insertion and removal arcs is the portion of the needle path within tissue. The bottom two figures show the range over which the location of the wound can be moved while still keeping the unreachable portion within the the "tissue" portion of the suture arc. The dashed, black arrow illustrates the range of possible successful wound locations given the unreachable portion of the path. The angle represented by the dashed, black arrow is the fraction of the total 360° of the circle over which the grasper could successfully place a suture.

way in which a family of sutures can be placed around an unreachable portion of the suture arc. Figure 4.20 illustrates the portions of the suture path through which the grasper must move in order to place a single stitch.

To decide A suture placed at a given location will pass through a circular arc. The grasper holding the suture needle thus must sweep over a portion of that circular arc as the needle is inserted into the tissue. During needle retraction the grasper

again must sweep over a portion of the needle's arc (Figure 4.20). However, to place a stitch, it is not nessisary for the grasper to pass through the full 360° of needle arc. It is obvious that the grasper can not travel through the portion of the suture arc which is within the tissue. It is unnecessary for the grasper to travel through the top portion of the suture arc (the portion located approximately 180° from the wound). Thus even if the graserp were unable to traverse the portion of the suture within the tissue or the very top of the suture arc there still exists a subset of possible wound locations around the arc in question which are reachable. The objective of the partial arc method for calculating performance is to ensure a success is only recorded when the grasper can traverse a portion of the arc sufficient to place a stitch when constrained to a perfect circular path and ideal grasp.

If a suture path has a portion which is unreachable by the grasper the performance measure for that path may be zero or may be some fraction of the total path. Figure 4.20 illustrates the portion of the suture path through which the grasper must pass to place a needle. Of note is the angle of the suture path located within the tissue (α_3). Figure 4.19 shows an unreachable region which covers a small angle of the total suture path. This unreachable angle is illustrated as smaller than α_3. The difference between α_3 and the unreachable angle is the range of angles over which sutures could be thrown. The difference divided by 360° results in the partial pass measure for that particular suture arc.

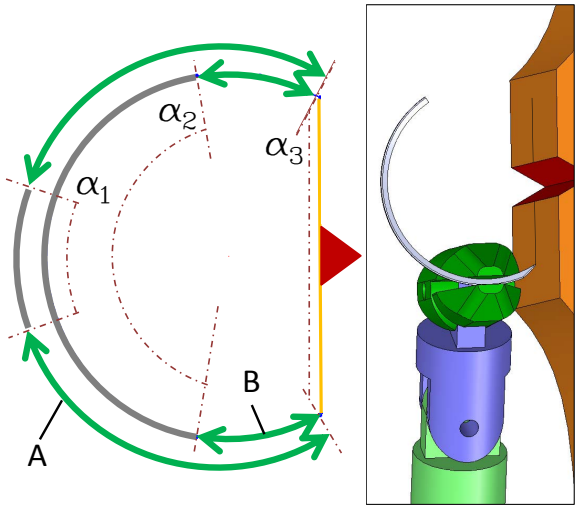

Figure 4.20: Required grasper sweep with regrasp: A regrasp of the needle reduces the total sweep required of the grasper. **A** represents the range of grasper motion required to drive a 1/2 arc needle through the illustrated section of tissue with a single regrasp each during insertion and extraction. **B** represents the same with approximately 10 regrasps per insertion and extraction step. α_1 is a range of needle sweep through which the grasper multi-regrasp case. α_3 is the portion of the needle sweep through the tissueis not required to travel with a single regrasp. α_2 is the same for the multi-regrasp case. α_3 is the portion of the needle sweep through the tissue. The grasper would not enter this area.

4.3.6 Device Optimization

The distances from wrist to finger joint axis (wrist length, Figure 4.21) and the distance from finger axis to grasp (finger length) were optimized using the Percent Pass and Partial Arc methods. Matlab's `fminsearch` function was used to find the combination of lengths which maximized the mean pass rate. `fminsearch` is an unbounded minimization function. To prevent a solution which is out of the realm of mechanical possibilities, a pair of sigmoid functions based on mechanical design limits for the two lengths being optimized are used to bound the search. The wrist and finger length bounds were 6.8-12 mm and 4-12 mm. The lower bounds were limited by the minimum lengths needed for the joint types selected for the prototype

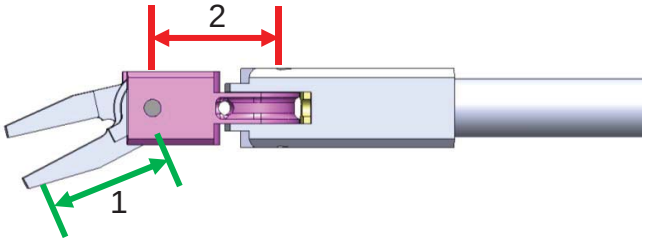

Figure 4.21: Grasper Dimensions for Optimization: Grasper jaw length to the point of grasp(1), Wrist length (2)

device. The upper limits were soft limits. The device joints are operated by opposed cables. The tension on a cable acting at the radius of the drive capstan yields the torque available to the joint. This torque results in a force acting at a distance from the joint. The longer that distance the lower the force the joint can apply. Thus to increase the force which can be applied by a given cable tension the length of grasper extending beyond the joint should be minimized. The optimized values for the finger and wrist lengths for the Percent Passed were 7.45 mm and 4.64 mm respectively. An optimization using the Partial Arc method yielded similar results.

4.3.7 Device Comparison

Using the above methods the prototype device design is compared with a 5 mm EndoWrist grasper and the 5 mm RealHand needle driver. These two tools were selected because their distal ends are the most similar to the prototype tool in both size and function. However, neither is specifically designed for use in the throat. The 5 mm EndoWrist tool has a $\pm 60°$ range in both wrist axes. The RealHand needle driver has an articulation range of $\pm 45°$ in either axis. The prototype tool is limited to $\pm 90°$ in the finger axis and $\pm 45°$ in the wrist axis.

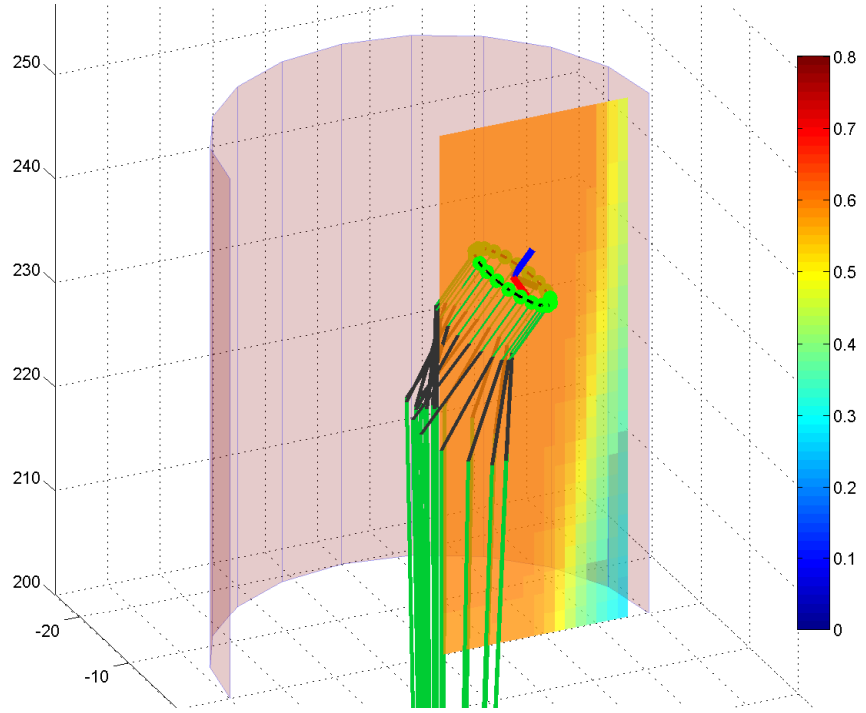

Figure 4.22: Overly of a performance map on the surgical workspace: The performance map is a way to represent the performance of a tool at any given [Y,Z] point in the workspace. In the figure a needle path is shown centered at [7 235]. The color of the map at that point indicates that the tool can reach 55% of the possible grasp points for all the tested orientation at that [Y Z] location. The colors of the map can give an indication of where a tool is most and least dexterous in the workspace.

To graphically represent the results of the comparison a performance map is used. The details of the map and its location in the workspace are shown in Figure 4.22. A value of 1 at any location would indicate the tool was able to complete 100% of the suture orientations tested at that location. The relative performance of the tools can be compared using the average performance over the workspace. If more detailed spatial information is desired, the performance map can be used to visualize tool performance within the workspace. One might choose to use this information to design a tool with as close to uniform performance as possible. Alternatively, if a particular subset of the workspace is considered more critical, the local performance of the design cam be visualized on the performance map.

The results of the tool comparisons can been seen in Figures 4.23 and 4.24. The limited wrist articulation of the prototype tool resulted in a lower success rate using the Partial Arc objective function. Thanks to the ability to articulate to 60° in both wrist axes the 5mm EndoWrist showed better performance than the other tools when evaluated using the Partial Arc test. This test places a premium on wrist articulation in all directions. However the negative impact of a long grasper and large wrist bend radius can also be seen in the performance of the EndoWrist. The lower, center of the work space (Figure 4.23 - right) shows reduction in performance. This is because the edges of the tool collide with the opening of the laryngoscope when trying to reach this portion of the workspace. This illustrates the advantages of a relatively short wrist design. The RealHand's performance was limited by the combination of only 45° of wrist articulation and the same relatively long wrist and grasper as seen on the 5mm EndoWrist.

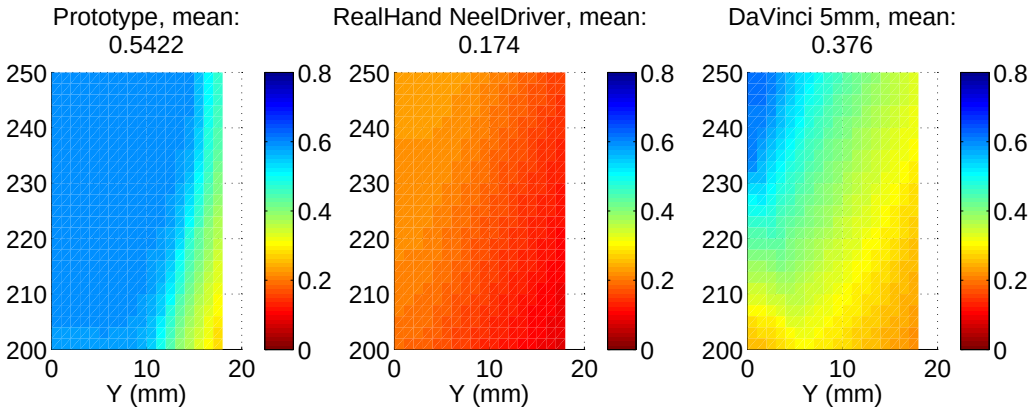

Figure 4.23: Simulation results comparing the prototype tool to the RealHand needle driver and the 5mm Intuitive Surgical EndoWrists using the Percent Passed objective function.

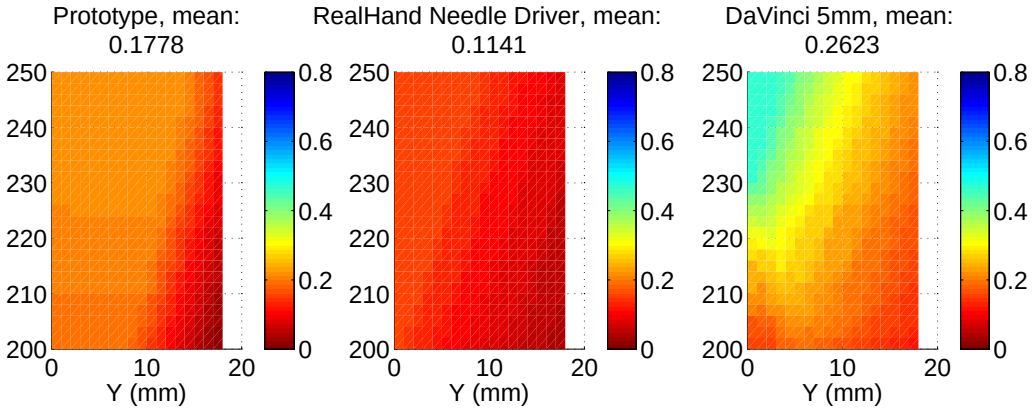

Figure 4.24: Simulation results comparing the prototype tool to the RealHand needle driver and the 5mm Intuitive Surgical EndoWrists using the Partial Arc objective function.

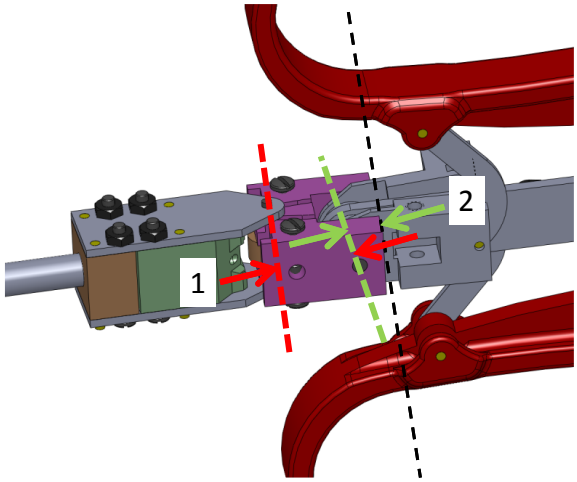

Figure 4.25: Proximal wrist optimized dimensions: Length of the wrist link (1), Distance from the proximal finger/jaw pivot to the line of grasp (2).

4.4 Proximal Wrist Optimization

The handle optimization was performed after the workspace optimization. Two of the dimensions driving the design of the user interface of the prototype tool (shown in Figure 4.25) were not set by other design requirements and thus were candidates for performance optimization. Both of the dimensions had an impact on the measure of naturalness as described by the Cross Correlation values from Chapter 3.

The Cross Correlation value is used as objective function because the ideal value is zero and any non-ideal value will be positive. Thus a simple minimization over the range of input variables can be performed.

The tool was placed in a series of poses. For each combination of handle position and wrist link length the mean Cross Correlation value was calculated and returned as the objective function. A surface plot of mean Cross Correlation value vs. the optimized values is shown in Figure 4.26. Due to mechanical limitations, the wrist

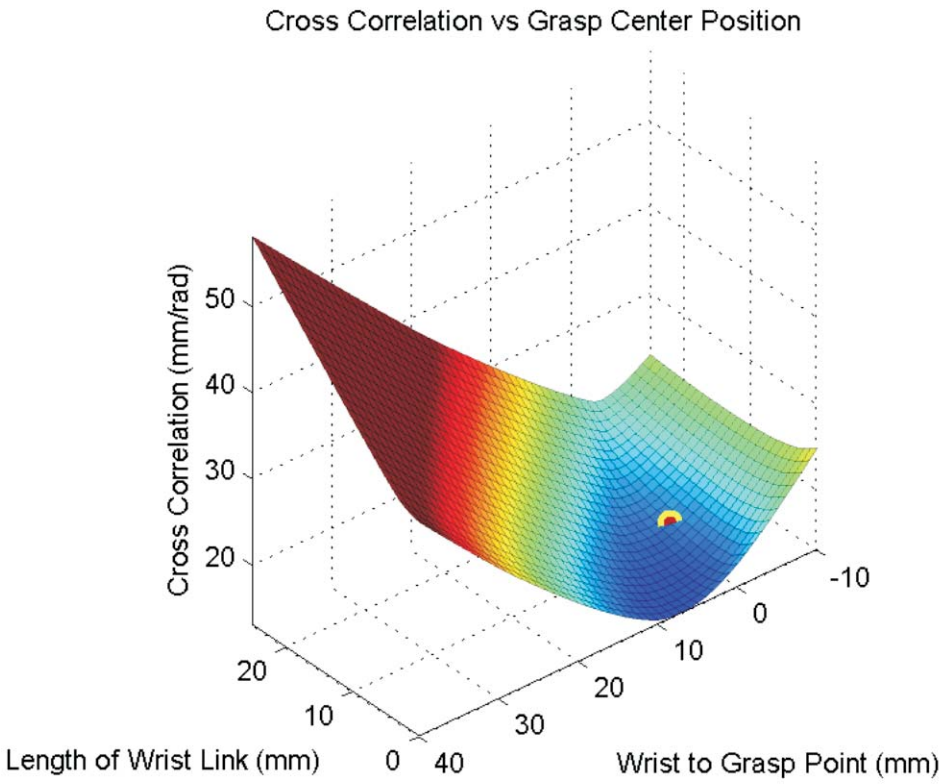

Figure 4.26: Cross Correlation value as a function of wrist link length and wrist to handle grasp location. The red point represents the values of the prototype tool design.

link length cannot be decreased to the calculated ideal value. The actual values of the prototype tool are indicated on the surface plot.

4.5 Conclusion

Chapter 3 described metrics and guiding principles for the development of user interface for a novel dexterous, manual laparoscopic tools. In this chapter the naturalness metric was used to optimize the geometry of a dexterous tool for suturing in the throat. Additionally, the prototype user interface, first described in Chapter 3, was applied to this dexterous tool.

The prototype dexterous tool described in this chapter offers the potential for enhanced dexterity in the upper airway without the need for automation. The design lessons of this prototype tool are currently being applied in the creation of a second generation of wristed dexterous tools. Both the test tools of Chapter 3 and this throat tool are partially supported by a telescoping pivot location along the tool's main shaft. This pivot location is typically the trocar used in laparoscopic surgery. Since a trocar is not typically part of a throat procedure a support within the laryngoscope must be provided.

Chapter 5

Static Balance of a Continuum Structure

Biologically inspired continuum structures are an active area of robotics research with respect to minimally invasive procedures. Continuum robots are defined by a continuously bending structure with an infinite number of degrees of freedom i.e., a flexible, elastic section [106]. Closely related, and thus of interest here, are hyperredundant joints which used a finite number of structural elements connected with discrete joints or elastic members. These two related structures have greatly impacted the area of minimally invasive surgery.

Continuum structures have advantages over traditional mechanical joints. A continuum "joint" at minimum requires only a flexible central structure and some tension elements to deflect the structure. This simplicity allows for two significant advantages over structures comprised of fully actuated revolute joints and links. These related advantages are the ease of fabrication (no complex joints or routing of cables to operate serial joints) and compact size (thanks to the simple nature of the structures). The deflection of the joint results from balancing the tension along the length of the backbone. In most cases this results in a circular curvature but more complex cases are possible with selective tendon routing [82]. The reliance on a flexible structure can also make them inherently compliant, which can be important when used around delicate anatomical structures.

The fabrication of such structures is simpler than structures using fully actuated revolute joints and serial links for two reasons. First, the central structure can be made

from a continuous element rather than an assembly of rigid, vertebrae-like structures and joints. This simplicity is an enabler with regards to reducing the diameter of such structures. Second, without an elastic element balancing the deflection of a serial chain of revolute joints, a traditional, fully actuated joint requires control cables or links for every element in the series to ensure each deflects correctly. This can quickly become an enormously complex structure.

The continuous curvature of a continuum structures is another advantage. Typically some sort of end effector must operate distal to the joint. This end effector might be a camera, laser, or even a mechanical tool. The gentle, continuous curve of the continuum joint is a more suitable conduit for the electrical wires, fiber optics, or mechanical rods and cables which might operate an end effector. Revolute joints can create sharp bends which pinch or crimp force transmission cables.

5.1 Continuum Structures in Medical Applications

There are a number of existing examples of continuum structures in medical applications. The examples described below are a sampling of uses and not meant to represent an exhaustive survey of the field. The examples are meant to cover a range of structural designs including flexible backbone, multi-backbone and hyper-redundant examples.

Continuum actuators are frequently found on catheters and colonoscopes as a means for steering the end of the device. A number of these designs are based on the concept of two or more tension wires deflecting a backbone structure. Tension on the wires results in a deflection of the joint and thus steering of the device. Breedveld

describes such structures as well as showing a variation on the concept using a series of "ring springs". Uneven compression of the "ring springs" allows for significantly tighter bend radii than with more conventional steerable scopes [14]. Camarillo et al. used the tension wire structure in a steerable cardiac catheter [16]. The inherent flexibility of the structure allows it to flex and displace as it works around the beating heart.

Hyper-redundant structures are similar to continuum structures but include a serial chain of rigid "vertebrae" sections and joints. The joints can either be flexible sections or more conventional revolute joints. In cases where revolute joints are used an elastic element is also incorporated into the joint.

Van Meer et al. used a semi-continuum joint as a substitute for a more traditional wrist joint such as those seen on tools in Chapter 3 Section 3.2. The structure illustrates a simplified 2 DOF wrist joint for a surgical grasper [104]. The use of a hyper redundant joint enabled the creation of a low cost, plastic joint with bend radius sufficiently large to enable the passing of cables needed to operate a distal joint without the use of pulleys or other complex transmissions. This joint used elastic rods, running the length of the structure, to equalize the deflection of the component joints that comprise the total structure.

Multi-backbone designs combine the functions of structure and tension wires by replacing the wires with flexible rods or tubes. The rods can apply both tension (pull) and compression (push) to deform the structure. The multi-backbone concept has advantages over a traditional single backbone plus tension wire structure. In simplified terms the multi-backbone structure is stiffer for a given diameter and length

as compared to central backbone structures [88].

The manually actuated Seeker steerable biopsy needle (PneumRx Inc, Mountain View, CA) is an example of a manually actuated, multi-backbone continuum structure in a medical device. The Seeker needle is bent using solid, flat, push-pull rods on either side of a flexible core. This mechanical design allows the continuum structure to be no larger than a traditional needle (21 gage, 0.82 mm diameter) yet rigid enough to deflect a thin wall hypodermic tube.

A larger scale example of a multi-backbone continuum design is described by Simaan et al. [89] has shown potential for a 4 mm structure to function as the arms of a dexterous manipulator in the upper airway [49] as well as in the twin arms of a single port surgical system [109]. Multi-backbone structures of this scale (3-8 mm diameter) are of interest because they are similar in diameter to conventional laparoscopic surgical tools and could support similar end effectors.

5.2 Bending Forces

As discussed above, continuum structures are highly versatile. However, such joints have a significant limitation when used in manually actuated systems. Continuum joints by definition are elastic, and thus the deflection of a continuum joint results in the storage or release of energy. If the amount of energy is relatively low, such as that needed to steer a catheter, the actuation forces required by the operator may be low enough to go unnoticed. Friction inherent in the mechanism may provide sufficient force to hold a given pose against the strain energy of the joint.

At some level, depending on application, the strain energy in the system can no

longer be masked from the user with simple friction. The energy required to displace the continuum joint is felt by the operator in the form of a restorative force trying to return the structure to a low energy, typically straight, configuration. This creates a potential use hazard since the device will spring back to the low energy state if the control handle is released during use.

Another area of concern is force transparency. The loads felt by the operator are a combination of the forces applied to the end effector (mechanically transmitted through the mechanism) plus the force required to act against the strain energy stored in the joints. Judging contact forces is further complicated because the force of the continuum mechanism varies with displacement. The force required to balance the spring energy can easily exceed the contact forces of interest.

High forces required to control the device may result in changes to how the user control must be held. The use of a power grasp vs. a dexterous grasp may be required [70]. The reaction forces of the tool against its surroundings must also be taken into consideration. The force applied to the user control may result in unacceptably high reaction forces at the trocar or port where the tool enters the body.

When used as part of a robotic system, the above concerns are muted. The servo actuators can resist the elastic loads with no impact on the user. The high reaction forces can be contained within the device rather than imparting forces on the trocar or entry port.

To address these problems in a non-automated system, this thesis proposes the application of static balance theory to create counter balance mechanisms for use in

the design of tension wire and multi-backbone continuum actuators. The addition of a spring based mechanisms can be used to balance the energy needed to actuate the continuum joints, thus enabling the operator to manually operate continuum joints whose inherent stiffness would render them otherwise impractical for a manual application.

The contribution of this chapter is the description of three possible mechanisms for use in the balancing of continuum joints. A multi-backbone joint of the design described by Simaan et al. [89] will be used as an example structure in this chapter though the principles can apply to a larger range of continuum joints.

This chapter will start with a introduction to the general concept of static balance. This will provide a framework for the later balance mechanisms (Section 5.3). These first two sections provide the backdrop needed to develop the balance mechanisms of Sections B.1 to B.3. In these sections two cam-based based and a family of linkage-based balance mechanisms are described.

5.3 Static Balance Mechanisms

Static balance mechanisms, a class of what Herder referred to as Energy Free Systems [39], are mechanisms that exist in an energy neutral state over a range of motion. The most common example is the simple balance beam where masses on opposite sides of a pivot are balanced (Figure 5.1-right). The simple balanced beam can be thought of as two pendulum arms attached to one another. As individual arms the pendulums have two static equilibrium positions. A stable position at the bottom of the pendulum's swing and an unstable one at the top (Figure 5.1). When rigidly joined, this pair

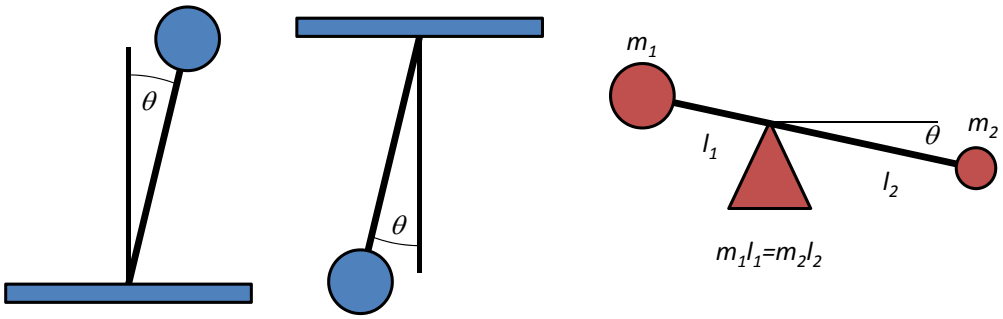

Figure 5.1: Pendulums and a simple balance. The traditional pendulum is in equilibrium in only two positions, the unstable inverted state when the arm is purely vertical (left) and the stable state when the arm is vertical under the pivot (center). Two pendulums can be combined to create a balanced pair of masses where the sum of the potential energy of the system remains constant regardless of angle (right).

of pendulums shares the common property of all static balance systems, the sum of the potential energies of the system remains constant throughout its range of motion. Energy is transferred from one storage medium to another, potential energy of one pendulum arm into the other, but not in or out of the system. The most common energy storage means are gravitational (weights and counterweights) and strain energy typically in the form of springs.

By maintaining a constant energy level, no force beyond that to overcome friction and inertia is needed to move the components of the system. If frictional losses are minimized a relatively small amount of energy can command a system which contains a significant amount of energy. To intuitively understand this, one need only think of two heavy masses on a balance beam. The masses can be moved with relative ease because the only energy added to the system is to overcome friction and inertia.

In addition to reducing the amount of force needed to move a system, the balancing of forces can result in a system which remains in place when moved. The balanced

arms used to support movable operating room lights and microscopes are examples of such systems. The unwanted force of gravity is counter balanced and the light can be moved with greater precision.

Force information can be exchanged more readily across a balanced system. Consider masses attached to the end of a balance beam as shown in Figure 5.1. Absent the balance beam a person would have difficulty noticing a 5% increase in mass, say 21 kg from 20 kg. However, if the illustrated mechanism perfectly balanced a 20 kg m_1 then an increase of 1 kg would feel like a change from 0 to 1 kg for a user lifting at m_1. In this way the balance mechanism increases the transparency of a mass change to the user as the small difference in the two masses becomes readily apparent. This same principle applies to balances of spring energy as well as gravitational energy. It should be noted that both perfect balance and approximate balance mechanisms exist. A perfect balance mechanism should mathematically balance all forces with no error. An approximate balance mechanism reduces the balance error to an acceptable level.

5.3.1 Medical Applications

Static balance mechanisms have been used in a number of medical applications beyond simply canceling the weight of lights and surgical microscopes. Tolou et al. addressed the issues associated with elasticity in the cosmetic glove covering of a prosthetic hand. The energy used to elastically deform the glove consumed approximately half of the force available to the grasp [100]. The static balance mechanism made more force available to the actual grasp while also allowing the mechanism to be held in a

pose with little static force being applied by the operator.

At least three prototype surgical graspers have been designed around the concept of using a static balance mechanism. Powell et al. developed a micro grasper using a compliant grasper design [75] with a target diameter of 0.5mm. Drenth et al. [25] proposed an endoscopic grasper using a static balance system to remove system backlash. The balance mechanism was used to avoid the friction normally associated with cable/rod actuated graspers. The expected results were better force transparency allowing the surgeon to better gauge the grasping force applied to the tissue at the distal end of the device. Stapel et al. have proposed a 5mm diameter flexure based grasper [95]. Again the objective is force transparency and reduction/elimination of the grasper's natural tendency to return to an open state without an operator-applied closing force.

5.4 Continuum Structure Application

While the above are all medical examples of a static balance mechanisms, no examples specifically addressing the energy balance needs of a tension wire (pull) or multi-backbone (push-pull) continuum actuator were found in the literature. To address this application, a model of the continuum structure and its energy vs. displacement is required.

It should be noted that a there are a large number of continuum structure types and this work seeks only to balance a small subset used in some medical devices. Several review papers have covered the range of continuum structure in greater detail [44] [81] [106]. This work will consider specifically two types of structures due to

their similar energy vs. displacement properties. The first is the tendon-actuated, incompressible backbone structure. This is a common type and described in greater detail by many authors. Once recent example is the work of Rucker and Webster [82]. The second type is the multi-backbone push-pull type comprising of a series of parallel rods or tubes arranged around a perimeter and an optional central rod, with all constrained to an end plate. Described in detail by Simaan et al. [89], the structure of this joint is deflected by selectively pulling and pushing on the rods around the perimeter. This type is of particular interest since it will be put into practice in Chapter 6.

This process will start with an assumption of a controlling mechanism. The continuum joint is not directly actuated by the user but instead via an intermediate mechanism such as a pivoting lever which translates movements of the lever into displacements of the continuum joint via manipulations of the tension wires or push-pull rods. For the purpose of developing a balance mechanism, it is assumed that this is an ideal controlling mechanism with no friction, backlash or energy storage. Thus energy can freely flow through this control mechanism between the continuum structure and the balance mechanism attached to the user control. In a physical realization of a balanced structure, this intermediate mechanism would allow the balance mechanism to be located remotely from the continuum structure, while still operating as an effective system.

For convenience, it is assumed that the angular deflection of the user control is equal to the angular displacement of the tip of the continuum structure (Figure 5.2). In practice this relationship is will be inherent in the actuation mechanism

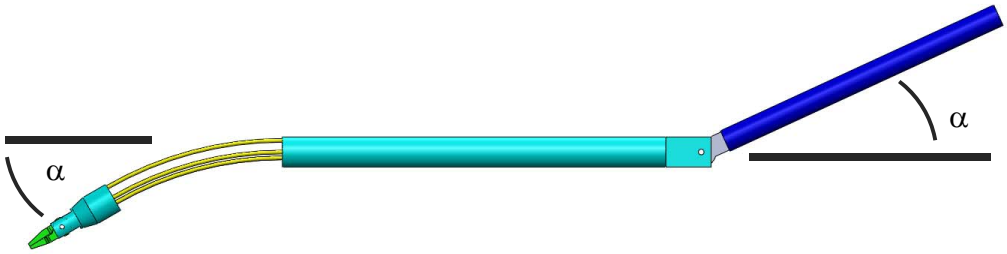

Figure 5.2: Basic conceptual layout of the continuum structure (left) and control handle (right). A mechanism is assumed to deflect the continuum structure based on the displaced angle of the control handle.

and the relative angular movement can be designed to be other than 1:1. With this assumption, the energy required to deflect the continuum structure can be considered in terms of the energy required to rotate the control handle. The forces applied to the control wires or push-pull rods of the structure can be translated into an effective torque applied to the control handle and felt by an operator.

5.4.1 Energy of Deflection: Single Backbone Joint

Gravagne and Walker described kinematic and energetic models of a tension wire actuated, flexible backbone, continuum section [32]. In the case of no external loading the deflected continuum section will be circular in section. The equation of deflection energy is follows the form of a linear rate, torsional spring. That is,

$$U_c = \frac{1}{2} k_c \alpha^2 \tag{5.1}$$

where U_c is the energy absorbed in the deflection of the continuum structure, k_c is an effective torsional spring constant of the structure and α is the tip bend angle.

5.4.2 Energy of a Deflected: Multi-Backbone Joint

The multi-backbone, push-pull continuum structure is comprised of multiple individual bent tubes or rods and was described and characterized by Simaan et al. [89]. As with the single backbone structure, the multi-backbone structure, absent external loading, is also assumed to be circular [110].

The sum of the energy required to deflect the structure is the sum of the energies required to bend the individual tubes, each with a circular deflection. It is noted that the stiffness of the continuum structure mildly increases as the structure is deflected. When the structure is deflected a tube on the inside of the structure decrease in length and thus increase in stiffness according to $k \sim \frac{1}{l^2}$. The tubes along the outside increase in length and thus decrease in stiffness according to the same equation. Because the change in stiffness goes with $1/l^2$ the increase in stiffness of the inner tube is always slightly greater than the corresponding decrease in stiffness of the outer tube thus the stiffness of the joint increases. In most practical applications, such as the tool design of Chapter 6, this small change in stiffness is inconsequential and masked by the manufacturing tolerances of typical springs ($\pm 5\%$ for the balance springs in the Chapter 6 tool) as well as system friction.

The change in stiffness is thus a function of the continuum structure length and diameter of the circle formed by the placement of the outside tubes. As an example consider a multi-tube structure with a free length of 15 mm and the outer tubes arranged around a 6 mm diameter circle (Figure 5.3). When deflected 45° the effective spring rate increases by approximately 3%. It should be noted that this example

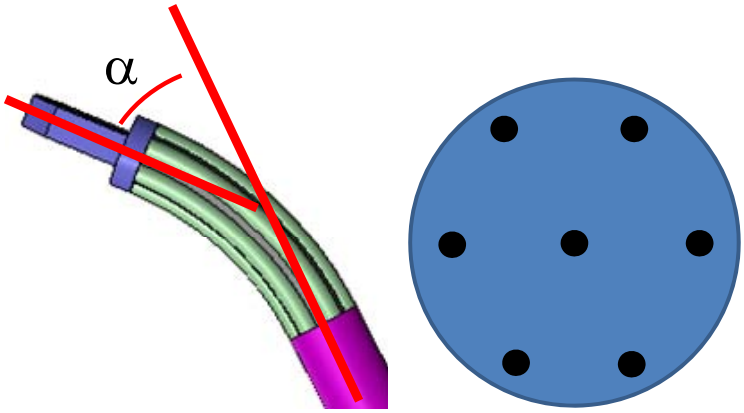

Figure 5.3: Illustration of the deflected structure (left) and the arrangement of the 6 outer tubes plus 1 center tube (right)

assumes a 15 mm long, 6 mm diameter joint, with a length to width ratio of 2.5, which is a particularly short, wide continuum structure. If the joint nominal length is increased to 60 mm (length to width ratio of 10) the change in effective spring rate between 0° and 45° drops to just 0.2%.

5.5 Balance Mechanisms

In order to balance the forces required to deflect the continuum structure with the force of a conventional spring some type of balance mechanism is needed. Three balance mechanisms have been developed to this end. The details of the mechanisms are described in Appendix B.

The first mechansim is a cam and follower (Figure 5.4). Using a pair of orthogonal cams integrated into a gimbal mechanism provides two degrees of balance (necessary for a 2 DOF structure). The second mechanism is an alternative cam design using wrapping cams (Figure 5.5). Appendix B.1 describes a method for designing a cam profile including optimization for spring tolerance.

Wrapping cams function like a capstan drive with a variable diameter pulley. A cable from the cam is connected to a spring in tension. Because the cable can only provide tension, and thus torque, in one direction a pair of opposed cams and springs are used for each degree of freedom. As with the single cam, the wrapping cam can be integrated into a gimbal to allow for balancing of two degrees of freedom. Appendix B.2 describes the creation of a pair of opposed, wrapping cam profiles.

The third mechanism type is based on variations of the over centered spring mechanism. In an over center spring mechanism a lever is pulled to either side of center by a tension spring connected across the lever and its base. Appendix B.3 describes the balance torques provided by a simple over center mechanism as shown in Figure 5.6 as well as a more complex variant using with a sliding link. The sliding link can be used to tailor the torque profile to allow for a larger range of movement as well as more precise matching of the torque required to balance the continuum structure. A 2 DOF over center mechanism with slider mechanism is shown in Appendix Figure B.18. An example of 2 DOF over center mechanism will be used in Chapter 6 to balance a continuum joint.

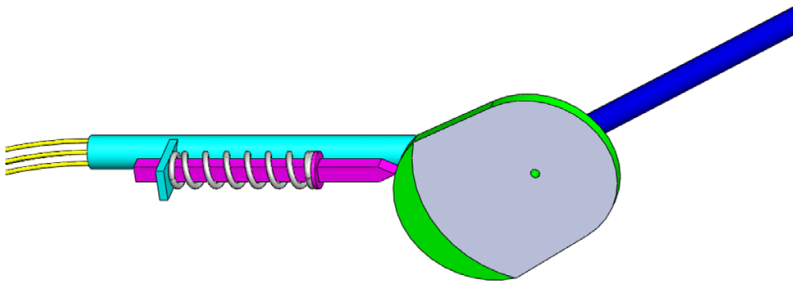

Figure 5.4: Conceptual cam balance system. Cam surface rotates with control handle (right).

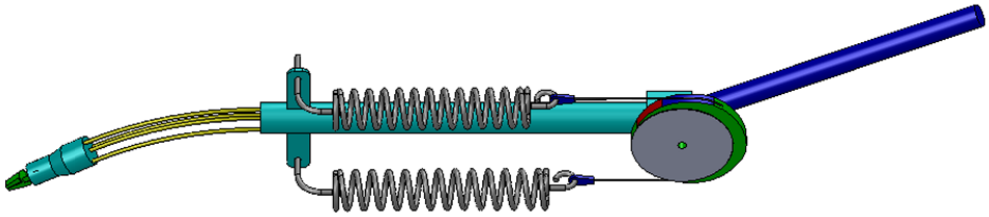

Figure 5.5: Conceptual layout of a flex joint balanced with an opposed pair of wrapping cams.

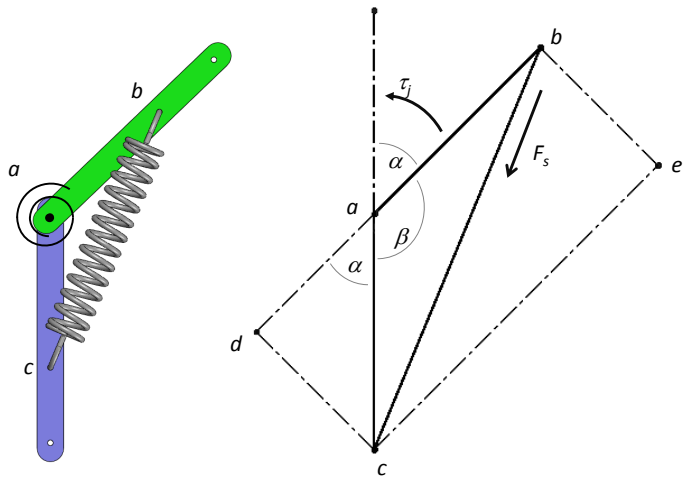

Figure 5.6: The geometry of an over center spring mechanism.

5.6 Conclusions

Though manually actuated continuum structures have existed on surgical tools prior to the advent of robotic surgery, the application of the structures was limited to relatively soft, low force applications such as catheter or colonoscope steering. The advent of robotic actuation has allowed the development of larger and more rigid continuum structures for surgical applications. Previous to this work, the force required to deflect these structures made manual actuation impractical. This chapter addressed this limitation with the creation of force balancing systems enabling larger continuum structures to be integrated into manual surgical tools.

The next application of this research will be in the construction of a surgical tool which includes a static balance system to balance the articulation of a multi-backbone continuum structure. The results of this effort will be described in Chapter 6.

Chapter 6

Dexterous Surgical Grasper with Wrist and Statically Balanced Elbow

The dexterous surgical tools previously described in this thesis have exhibited 6 DOF with 2 wrist DOF. Thus, they have 2 DOF more than a traditional laparoscopic tool inserted through a port. The need to pivot about the entry point to the surgical site can limit the total range of tool motion. For example, Chapter 4 described the construction of a surgical grasper for throat use. A significant design constraint was the need to pivot the tool within the confines of the laryngoscope which limited the workspace of the tool once in the throat (Figure 6.1).

The robotic throat surgery system described by Kapoor et al. [49] addresses this issue in part via the addition of an elbow joint operating within the area of the throat. With an elbow, the tool end effector is still allowed 6 DOF motion but the entry point must only allow for rotation and extension.

As with the robotic system of Kapoor et al., a manual grasper with elbow faces a design constraint in that the forces which operate the grasper must be transmitted through the elbow joint. As shown by Kapoor et al. with a robotic system, the smooth curvature of a continuum joint is well suited to this purpose. Channels within the joint can carry tension cables without sharp bends or the need for pulleys. However, previously, it was not possible to use a continuum joint in a manual tool. A continuum joint of sufficient stiffness requires a great deal of force to deflect. With the addition of a static balance mechanism, as described in Chapter 5, to address the issue of energy storage in the joint, a continuum joint becomes a viable elbow for a manual

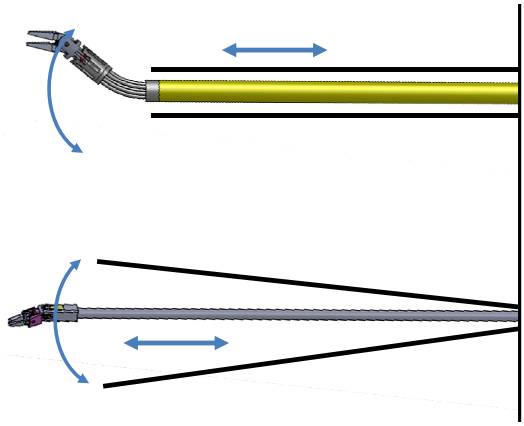

Figure 6.1: Two 6 DOF graspers. The lower tool shows the arc over which it must move in order to position the grasper. The upper tool uses an elbow to provide a similar number DOF, but requires a smaller workspace. This enables the upper tool to reach the surgical site through a more narrow channel without a loss in range of motion at the surgical site.

dexterous tool. This chapter will describe the design and construction of such a novel dexterous tool.

6.1 Tool Layout

The design of the this tool is based on the user study tools of Chapter 3 with the addition of both proximal and distal elbow joints and an energy compensation mechanism for the elbow joints (Figure 6.2). The elbow joints are of the pattern similar to that described by Simaan et al. [89] comprising of a series of push-pull tubes. Details regarding the calculation of the elastic strain energy of a joint of this type are provided in Chapter 5, Section 5.4.2. The push pull tubes are continuous between distal and proximal wrists. Six nitinol tubes (1.14 mm OD, 0.96 mm ID) are arranged around a 7 mm diameter base (diameter through centers of the component tubes). The cables that operate the distal wrist are carried inside the nitinol tubes. Three

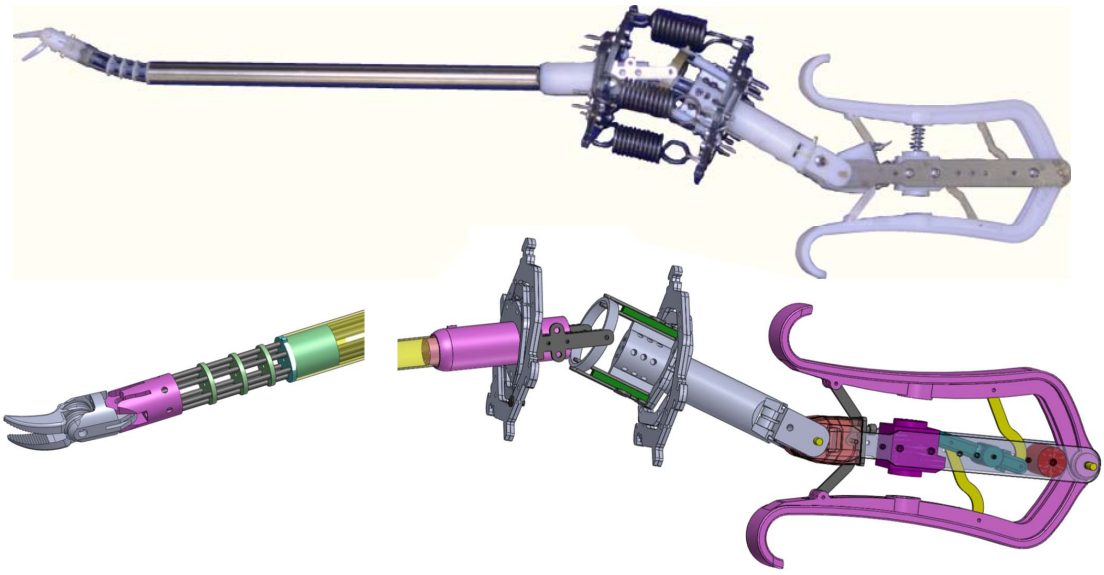

Figure 6.2: Illustration of the dexterous grasper with elbow with detail renderings. The left side of the illustration shows the distal wrist and elbow joints. Surrounding the proximal elbow joint is a gimballed spring assembly used to statically balance the deflection of the elbow joints. The renderings show the pair of gimbals which support the three balance springs. Note: Spring, pivot pins and proximal elbow tubes are not shown in the rendering.

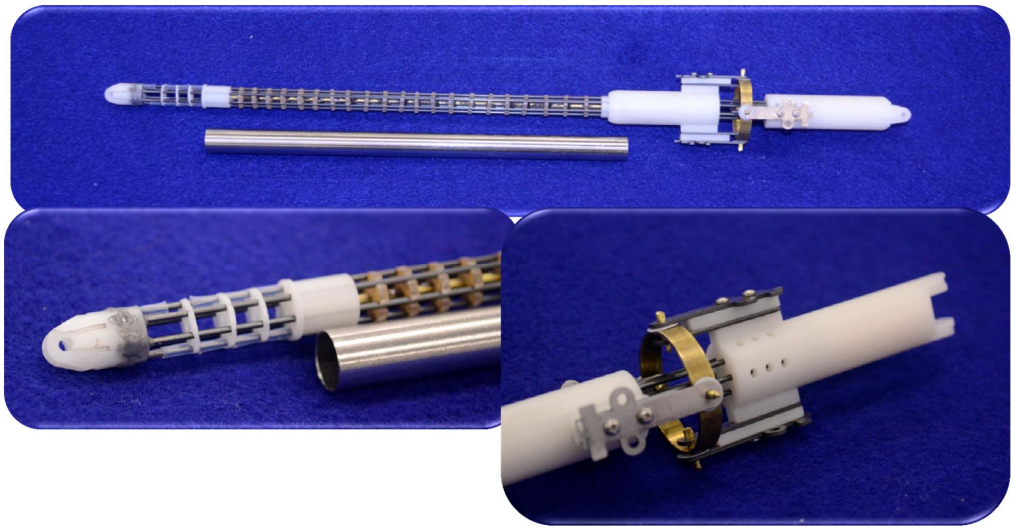

Figure 6.3: Distal (left) and proximal (right) elbow joint structures.

Delrin spacing discs are placed along the elbow joint. The spacing is maintained by 4 PTFE sleeves placed around the outside of two of the tubes. Epoxy is used to anchor the tubes into the distal wrist base (Figure 6.3). The nominal elbow joint length is 25 mm when straight. The elbow length increases during articulation for reasons described below.

The tool main shaft is 10 mm OD and contains a spacer structure which supports the nitinol tubes. Because the nitinol tubes are subject to compressive loads a series of radial discs support the tubes at 5 mm intervals for the length of the main shaft.

The proximal elbow uses the same 6 mm tube spacing as the distal elbow. The nominal length of this elbow structure is 20 mm. The energy balance structure applies a compressive load of approximately 90 N (20 lb) to this joint. To avoid applying this compressive load to the nitinol tubes a support yoke and cross type joint was place coaxially around the tubes. This structure supports all compressive as well as torsional loads applied to the proximal elbow joint. With the kinematic center

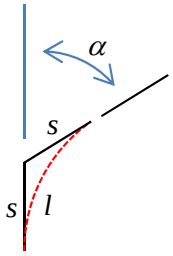

Figure 6.4: Diagram representing the proximal elbow joint of the tool. Lengths l are the length of the yoke legs, (10 mm). The circular arc has length l and represents the length of a tube in the elbow joint. α is the articulated angle. When $\alpha = 0$, l is straight and has length $l = 2s$. When deflected the length of l decreases. The change in length is given by Equation 6.3.

of the yoke and cross joint placed at the mid point of the elbow joint the tubes will be able to assume a circular arc as deflected. However, the nominal length of the joint will decrease with articulation (Figure 6.4). The change in length of the nominal tube length, the length of an arc following the centerline of the joint, is given by Equation 6.3. The reduction in length of the proximal joint is added to the nominal length of the distal joint which is allowed to expand as deflected. Though the energy balance calculations for this tool are based on a 0° to 45° range of motion, the structure of the support yoke and cross are, due to mechanical interference between component parts, limited to 35° in either of the cross's primary axes. A deflection of 35° in both of the axes results in a combined deflection of 47°.

$$u = \frac{\tan(\alpha/2)}{l_o/2} \tag{6.1}$$

$$l = \frac{\alpha}{u} \tag{6.2}$$

$$\triangle l = l_o - l \tag{6.3}$$

Where u is the curvature of the arc, l is the instant length of the arc, l_o is the initial tube length and equal to 20 mm in this case, and α is the deflection angle. At a deflection of 45° this results in a 1.04 mm decrease in length of the proximal joint and an equal increase in length of the distal joint.

The static balance mechanism, described in greater detail in Section 6.2, consists of three extension springs and a pair of 2 DOF gimbals. The gimbals are mounted 25 mm from the center of the proximal elbow (50 mm apart). They ensure the forces applied by the 3 springs act as a virtual force applied to the centerline of the tool shaft. The spacing between the three springs and the centerline of the device is to avoid interference during articulation.

The energy stored within the pair of joints is calculated as follows using the method below. The strain energy in a single deflected beam is:

$$U_i = EI \left(\frac{\alpha}{l_i} \right)^2 \tag{6.4}$$

Where U_{ei} is the elastic energy in tube i, E is the Young's modulus of the material, I is the second moment of inertia of the tube, α is the bend angle of the joint, and l_i is length of the i^{th} tube. The Youngs modulus is listed as 41 to 75 GPa on data sheets from the manufacturer, NDC, Inc. As was previously mentioned due to the use of a yoke joint around the proximal elbow, during articulation the nominal length of the proximal joint decreases per Equation 6.3. Once the nominal joint arc length is calculated, the length of each component tube is calculated. Like the total structure, the tubes of the continuum structure are assumed to form circular arcs. The arc

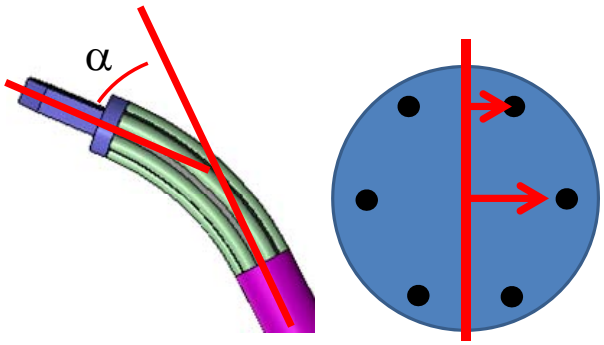

Figure 6.5: Deflected continuum joint. The red line (left) indicates the neutral axis of the deflected joint. The normal distance from the neutral axis to two of the six tubes are indicated by the arrows.

length of each tube is the nominal length plus the normal distance from the neutral axis of the bend times the bend angle (Figure 6.5). Thus the arc length of tube i is:

$$l_i = l_n + r_i\alpha \tag{6.5}$$

where l_i is the tube length of tube i, l_n is the nominal length of the joint, r_i is the normal distance from the neutral axis of the bend to the base of tube i (positive is away from the direction of bend), and α is the angle of deflection.

Because the prototype tool uses linked continuum structures to create both the distal and proximal elbow joints the total energy in the deflected joint is the sum of the energy in the pair of continuum structures.

6.2 Energy Balance Mechanism

Several balance methods were described in Chapter 5. For this device a simplified over center spring mechanism was selected (Section B.3). The primary advantage of this concept was the simplicity of implementation into a 2 DOF joint structure. It

Table 6.1: Balance Spring Properties

Property	Value
Material	302 Stainless
Rate	25.50 lbs/in
Rate Tolerance	±5%
Spring OD	0.500”
Max Extended Length	2.17 in
Max Force	18.80 lbs
Preload	1.70 lbs

required no cam followers, cables or sliding links. The entire balance assembly could be made to fit coaxially around the proximal elbow joint.

For the over center mechanism, the total change in spring length is 3.95 mm. This includes the gimbal thickness plus the 50 mm between gimbal plates (52.60 mm - 48.65 mm). The estimated total joint energy was 0.56 J. This estimate assumes a Young's modulus for nitinol of 65 GPa. Thus, with a 3 spring configuration each spring must transfer one third of this, or 0.187 J with a change in length of 3.95 mm. The springs selected for the compensator are McMaster Carr (Atlanta, GA) precision springs, catalog number 9044k365 (See Table 6.1).

At an extension of 49 mm the total elastic energy in the spring is 0.354 Nm. When the length is decreased by 3.95 mm the total energy is 0.167 Nm for a delta of 0.188 Nm or 0.563 Nm for three springs. Spring adjustability was considered in the design. Adjustments were achieved by changing the preload of the springs (the extension of the spring when the joint is at 0° of deflection) by the addition of a short link between the spring hook and the gimbal mount. This was needed due to both the rate and dimensional tolerances of the springs as well as tolerance in the Young's modulus of the nitinol tubes.

6.3 Elbow Joint Testing

In order to test the performance of the force balance mechanism, the force required to deflect the continuum elbow joint was measured prior to and after the installation of the balance mechanism. The measurements were taken with an ATI Mini 40 6 axis load cell with a resolution of 1/50 N in the Fx, Fy axes (ATI Industrial Automation, Apex, NC). The load cell was attached to a 6 DOF Mistubishi robot, which acted as a linear displacement stage. The load cell applied force to the joint via a protruding rod pushing down on the section of the device between the proximal elbow and wrist joints. As measured in the straight elbow configuration, the load cell force was applied 45.6 mm from the center of the proximal elbow yoke and cross joint. In both the compensated and uncompensated configurations the joint was tested with the load cell applying force in four orientations of the tool; X+ up, X- up, Y+ up, Y- up (Figure 6.7). The force measurements were taken every mm of load cell travel. The load cell values were converted to effective joint torque for analysis. The test setup is shown in Figure 6.6. Estimates of device performance can be seen in Figure 6.8.

The uncompensated joint tests started with the joint in a straight configuration. Force was recorded as the joint was displaced downward. Total force applied to the joint will include friction in the joint. The resulting data show a linear relationship between joint torque and displacement (Figure 6.9). The deflection of the joint was limited to 30° to avoid forcing the elbow joint past its 35° travel limit. The Young's modulus of the nitinol tubes was estimated based on the results shown in Figure 6.9. The fitted Young's modulus is 42 GPa. The expected performance curves of Figures

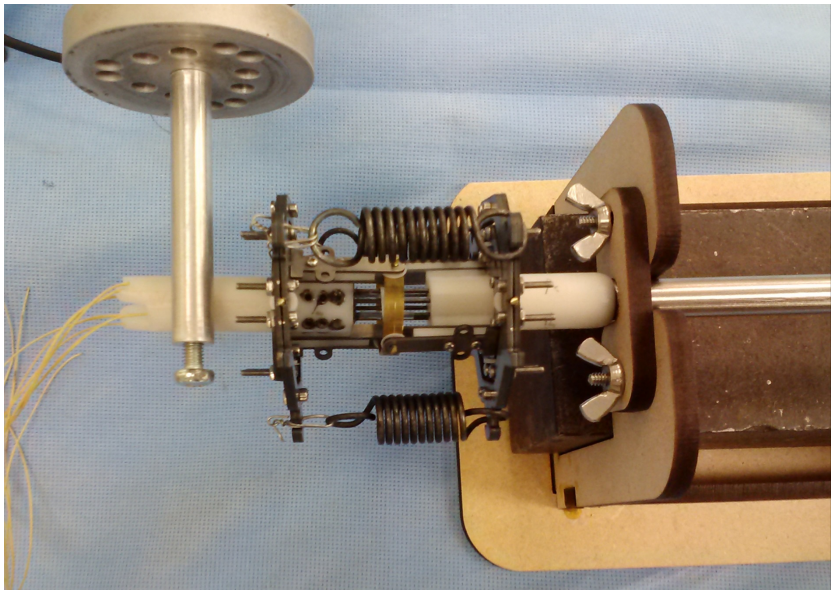

Figure 6.6: Elbow joint actuation test. A rod attached to an ATI Mini 40 load cell applies vertical force to the device handle.

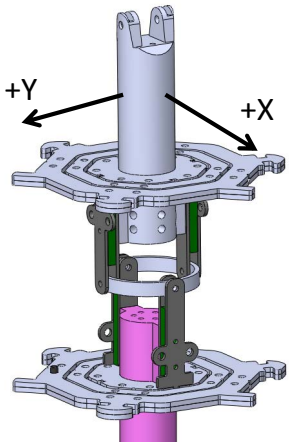

Figure 6.7: Directions of elbow joint actuation tests

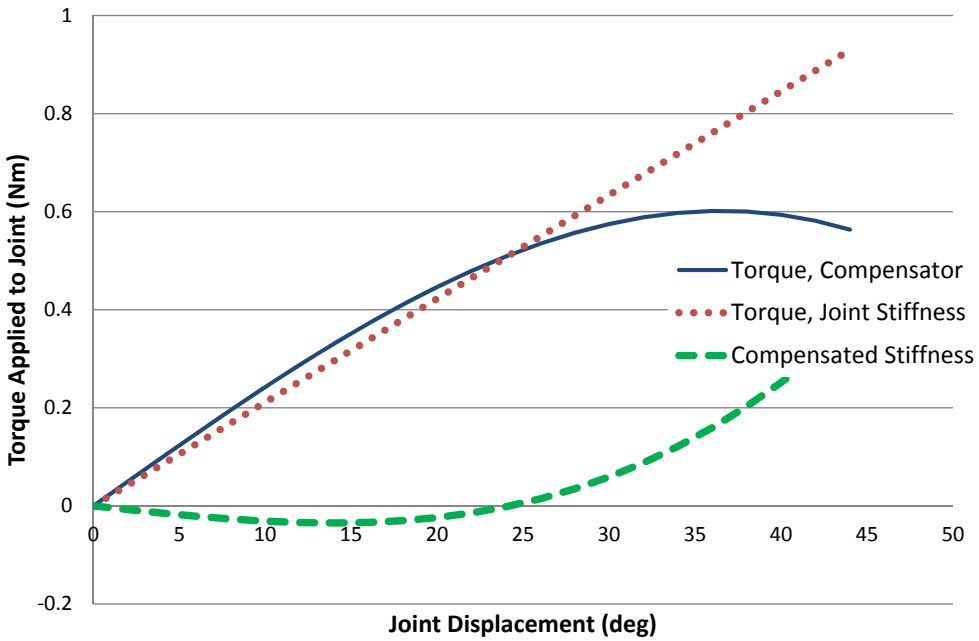

Figure 6.8: Estimated elbow joint compensation performance.

6.9 and 6.10 use this value.

A second set of measurements was taken with the static balance mechanism in place and with the spring preloads set accordingly (Figure 6.10). The combination of friction in the system and the balance mechanism are sufficient to allow the elbow joint to remain statically deflected. Thus the balanced displacement tests were started with 25° deflection of the elbow upward through to 30° deflection downward. The compensated joint shows a steady frictional torque of approximately 0.10-0.15 Nm. The average displacement torque increases to approximately 0.20 Nm at 30° of displacement vs. 0.60 N with the uncompensated model. One run shows a torque spike at 5° of displacement. This corresponds to a small mechanical "pop" in the spring support gimbal due to a slightly misaligned drill hole.

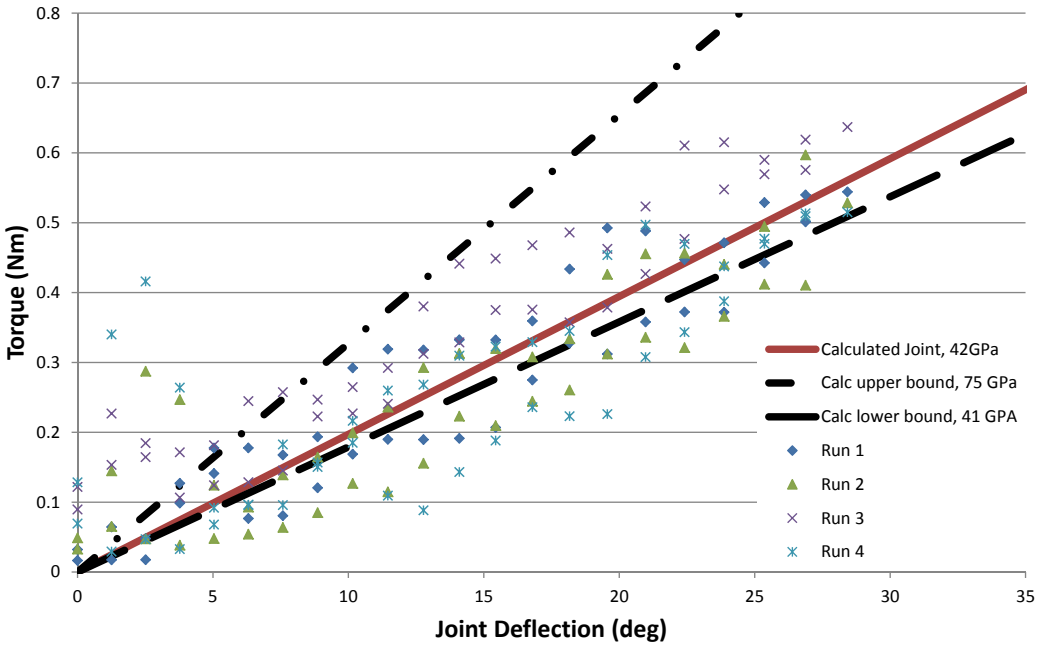

Figure 6.9: Elbow torque vs displacement without energy balance compensation mechanism. Calculated Joint, 45 GPa represents the expected performance of the joint. Based on the results of this test the estimation of the Young's modulus of the nitinol used in the construction of the device joints was revised down from 65 GPa to 42 GPa. The dashed lines represent the estimated joint performance using the minimum and maximum manufacturer's value for Young's modulus.

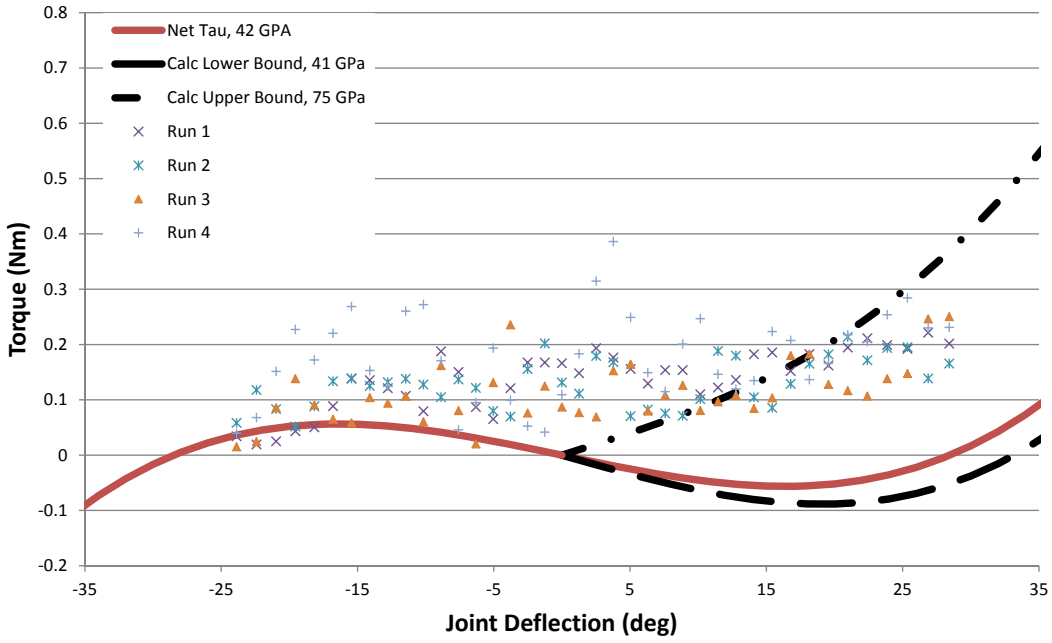

Figure 6.10: Elbow joint actuation test with balance mechanism in place. The force required to actuate the joint is relatively constant from -25° to 30°. The predicted compensation performance (disregarding friction) is shown as a solid line. The upper and lower performance bounds based on the Young's modulus of nitinol are shown by the dashed lines.

6.4 Conclusions and Future Work

The experiment has demonstrated a novel dexterous grasper prototype based on the concept of using a statically balanced continuum joint as a working elbow. This prototype is novel for being a practical manual actuator which could be deployed down a fixed rather than a pivoting trocar or other access port. The prototype is also novel for being the first example of a manually actuated, multi-backbone continuum section used in a surgical tool.

Having completed a proof of concept, the potential of manual surgical tools using statically balanced, multi-backbone continuum joints will be further explored in future work. The demonstrated spring and gimbal balance mechanism, while sufficient for proof of concept, is bulky and too exposed. A wrapping cam based mechanism designed around the layout described in Chapter 5 could provide significantly improved packaging via routing tension cables from the joint to a remotely actuated or placed cam. This would further have the advantage that the energy profile could be more accurately balanced vs. the simplified over center spring illustrated in this chapter.

The prototype was patterned on the wristed grasper tools shown previously in this thesis. A class of reduced size, non-wristed devices may have practical value in transnasal surgery. Existing tools for transnasal surgery are rigid and predominately straight. A tool with an adjustable radius, curved section, such as could be provided by a multi-backbone continuum section, would offer the ability to reach areas of the surgical field which currently can only be reached with a time consuming change of tools. The addition of a balance mechanism would be needed to provide a balance

between section stiffness and user control force.

A device with a long continuum section may have applications in throat-based procedures as well. A pair of continuum section based arms could be attached to a laryngoscope. As compared to the tool of Chapter 4 a pair of continuum arms may result in a larger range of motion as well as reducing interference between tools. By reducing the operating forces needed to articulate a multi-backbone, continuum section to a realm which can be readily operated without automation, the work described in this chapter will open the possibility for a new wave of dexterous surgical instruments.

Chapter 7

Conclusions and Future Work

The benefits of image guided, robotic surgery are compelling and the focus of a great deal of recent research. Image guided navigation has provided a surgical "global positioning system" allowing real time location of surgical tools in the operating room with respect to registered preoperative imaging. These systems offer surgeons "X-ray" vision into the surgical field.

At the same time, the use of high dexterity robotic systems such as the Intuitive Surgical da Vinci Surgical System have given surgeons unprecedented dexterity through minimally invasive surgical ports. Further advances with next generation surgical robots such as single port surgical systems promise the ability to deliver comparable dexterity in new locations yet unavailable to the da Vinci system.

Yet these systems have literally come with a high price at a time when cost effectiveness and cost reduction are becoming increasingly important in medicine. It has been the aim of this dissertation to offer ways to deliver the be benefits of image guided, robotic surgery with out the costs associated with automation. To this end, a laparoscopic surface scanner intended for use in image registration was developed. This system used off-the-shelf industrial hardware to minimize cost and complexity while delivering scanning accuracy comparable to and slightly better than the current standard, laser range scanning. This system has been used in the operating room to gather live human data.

This dissertation has also proposed removing automation from surgical manip-

ulators while maintaining much of the dexterity, natural movement and range of movement associated with automated tools. Removing automation saves the cost of actuators, sensors and their controllers from the cost of these dexterous tools. The first step in this process was the creation of a metric and a guideline which could be used to evaluate the "naturalness" of the motion of a manual surgical tool. This offers some level of guidance in the creation of not only dexterous end effectors but also in the creation of the user interfaces the operator must interact with and through which the operator will attempt to command the desired movements of the end effector.

The metric and guideline were validated with a user study comparing four custom designed prototype tools in a series of laparoscopic-like tasks. The design of the test tools included two representing the prevailing thoughts in both commercial and academic user interface designs as well as two related interfaces based on a user interface concept developed as part of this research. That interface concept, consistent with the metric and guideline proposed in this research, suggests a positioning of the hand with respect to the tool and a user design interface not previously seen in a manual dexterous manipulator. The prototype interface control also shows a significant performance advantages over the established interface concepts.

This work also approached the problem of removing automation from tension wire and multi-backbone continuum actuators. Relatively large diameter (4+ mm) and relatively stiff continuum actuators have been shown in robotic applications such as single port surgery, throat and cardiac surgical systems. Though impressive in capability, these structures had been previously impractical in a manually actuated device due to the high levels of elastic energy stored in the deflected structure. This

stored energy tended to return the joint to a neutral, unloaded state. This inherent mechanical stiffness would mask forces applied to the end effector, and would result in significant actuation forces felt by the surgeon if applied in a manual device without the static balance results presented in this dissertation.

Means to statically balance these forces were described. This included describing the energy stored in a deflected, continuum structure, and descriptions of force balancing three mechanisms. For manually actuated tools, these balance mechanisms make available many more options for high stiffness continuum joints which were previously impractical for use in manual tools. To demonstrate the potential of a high stiffness continuum joint used in a manual laparoscopic manipulator, a prototype manual manipulator with a dexterous wrist and multi-backbone, statically balanced elbow was designed and constructed.

7.1 Future Work

The research described in this thesis will continue both in the research space as well as, it is hoped, in commercial applications. The conoscope surface scanner is being used in current research in the Vanderbilt's Biomedical Modeling Laboratory and Surgical Navigation Apparatus Research Laboratory. These laboratories have taken the system forward into first use on live patients after the initial feasibility studies described in this dissertation. Areas of future work include both applications of the system in the operating room and further refinement of the surgical based hardware (sterility control, attachments needed for laparoscopic use).

The research regarding interface "naturalness" and the new user control scheme

for a wristed laparoscopic tool is ongoing. A second generation tool has already been developed and will be produced shortly (Figure 7.1). The objective of the second generation tool is to demonstrate a protoytpe which will look and feel like a production ready surgical instrument. In addition to some conceptually minor design enhancements and refinements, the user interfaces will gain a lock for the grasp action. This was a feature desired by a number of surgeons who tested the previous prototypes during the user studies described in this dissertation.

Another area of future work is investigating the impact of tool port placement with respect to the user on the use of these wristed tools. The user study was conducted with what might be considered ideal port placement. That is the participant was able to position his or her body as desired with respect to the test fixture and tool. Actual surgical cases are more likely to have limited or less than ideal placement options. The second generation tools will be tested in box-trainer like setups that simulate the more difficult access and port placements often associated with real surgical cases.

The pairing of statically balanced continuum joints and manual tools is an exciting area with at least four general areas for future research. The first area is in terms of balance mechanism packaging and refinement. While the three gimbal supported springs of the prototype tool is effective, it is not elegant and does not provide the best performance of the mechanisms considered in Chapter 5. The cam and slider mechanisms described in Chapter 5 have the potential to provide better overall performance but will require packaging creativity if they are to be paired with a two degree of freedom, joystick-like control as was used in the elbow tool prototype. Even the packaging of the simple over center spring mechanism as used on the elbow tool

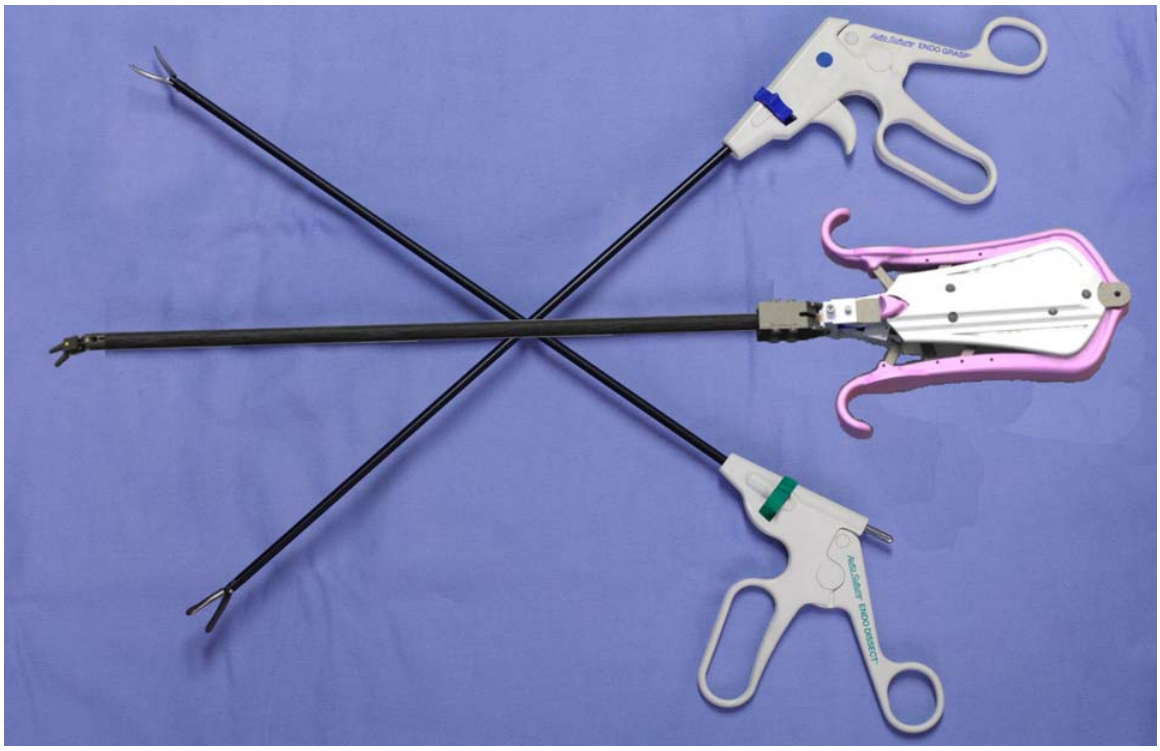

Figure 7.1: Rendering of second generation, wristed surgical tool with traditional laparoscopic tools

would need to be refined for use in a production product. Work on new packaging arrangements has already been started as of the time of this writing, but no prototypes have yet been completed.

A second area of research will be alternative tools and applications which might benefit from a manually controlled, multi-backbone continuum actuators. The high stiffness of a multi-backbone continuum structure (vs. the tension wire, single backbone structures) is appealing for use where relatively high forces are expected. Skull base surgery, or surgery in the throat or at the base of the tongue are areas where a small diameter, manual, flexible device may be of particular value. This class of tool could have a distal wrist as was shown in the Chapter 6 prototype or may use a less complex grasper or other tool. With a statically balanced mechanism, the continuum joint could move as freely as a traditional joint yet also smoothly curve around obstacles.

The above concepts considered continuum joints which are straight in their low energy state. For example, a tool designed for use in the throat could be constructed with a precurved continuum joint following the base of the tongue down to the larynx. Balance energy would not be needed to balance the base shape of the tool as it passed through the throat. Only a small additional amount of energy would be needed to balance the tip deflections. The complications of balancing a precurved continuum structure may present interesting new challenges.

Finally, the prototype wrist-elbow tool described in this dissertation showed that it is possible to build such a tool. Refinement of the design into a more production ready tool would be the next step. This might include large scale changes to fit a pair

of such tools into a single port surgery system. Alternatively, the system may retain the existing layout but incorporate a longer main shaft, thus enabling a surgeon far greater reach than is currently afforded by laparoscopic tools which must pivot at the body entry port.

In conclusion this dissertation has demonstrated the potential means by which the benefits of robotic image guided, dexterous, minimally invasive surgery can be accomplished without automation and automation's associated costs. The next steps are to move from proof-of-principle to commercial realization.

Appendix A

User Study Data and Reduction

A.1 User Study Data Reduction

The user study of Chapter 3 compares the relative performance of four test tools. The tools are compared using three test tasks (Following a sinusoidal wire path at +15° to the entry port, following a sinusoidal wire path at -15° to the entry port, and the ring transfer).

Each task is run in a forward and reverse direction (for example left to right and returning right to left). This results in 6 task trials per tool per participant. Finally three metrics are recorded for each trial. The result is 72 data points per participant.

The final objective of the data reduction is to, with statistical confidence, compare any two tools to one another and asses if there is a statistical difference in the mean performance of the two tools.

As part of the statistical process sets of data may be grouped and analyzed together. For example, the average time needed to complete the ring transfer could be considered alone or the average time needed to complete any of the 3 tasks could be considered as an aggregate group. Because the average time needed to perform the ring transfer is significantly longer than that needed to perform the sinusoidal wire path test the values are normalized prior to grouping data.

A set of data is normalized for the combination of: a given user (participant n), a

given task (ring transfer), and a given metric (time to complete). For this combination, the performance of all four tools (A-D) is averaged. The relative performance of an individual tool, for example Tool B, is the performance of the individual tool divided by the mean of the four tools. sec:TTCompare

The data reduction will start by normalizing the performance data for a given participant. This is done to remove the large scale differences in participant skill levels. An example of normalization is shown in Figure A.1.

Once the data is reduced to relative performance of an individual tool vs the average for all tools the data has become a series of percentage values. This allows grouping of otherwise unrelated data. For example, as raw data the number of errors a user makes with Tool A vs B and the time needed to complete the task with Tool A vs B could not be grouped as the data types are different. With the normalization of the data, data from dissimilar metrics becomes a percent representing the performance of a given tool with respect to the average of the 4 tools performing that same task. Because the normalized data represents relative performances of tools, the data can be group as comparative samples. This will be used to group the data into a single overall performance ranking.

A.1.1 Raw User Study Data

The complete data set is shown in Figures A.2 and A.2.

Participant	Tools				
	A	B	C	D	Avg/Prtc
1	309	239	243	218	252.3
2	203	205	96	94	149.5
3	359	306	330	225	305.0
4	205	206	292	262	241.3
5	156	153	165	156	157.5
6	300	419	129	166	253.5
7	107	99	160	170	134.0
8	150	92	107	84	108.3
9	161	256	187	158	190.5
10	303	228	308	307	286.5
Avg	225	220	202	184	
Std	81.2	92.0	81.5	66.4	

A			n=	10
B	~~-0.001~~		df=	18
C	~~-0.005~~	~~-0.005~~		
D	~~-0.016~~	~~-0.012~~	~~-0.007~~	
	A	B	C	D
t (sig)=		-1.71	1.71	

Participant	Tool % vs Avg for Participant			
	A	B	C	D
1	122%	95%	96%	86%
2	136%	137%	64%	63%
3	118%	100%	108%	74%
4	85%	85%	121%	109%
5	99%	97%	105%	99%
6	118%	165%	51%	65%
7	80%	74%	119%	127%
8	139%	85%	99%	78%
9	85%	134%	98%	83%
10	106%	80%	108%	107%
Avg	109%	105%	97%	89%
Std	20%	28%	21%	20%

A			n=	10
B	~~-1.19~~		df=	18
C	6.07	-2.83		
D	-11.02	-5.69	-4.13	
	A	B	C	D
t (sig)=		-1.71	1.71	

Figure A.1: Normalizing Data: Sample data of a single performance metric (time to complete task in 10ths of seconds) for a single task (+15° sinusoidal traverse, forward) for all 4 tool (A-D) designs and a subset of data with 10 participants. The left table is raw data while the data on the right is normalized per the participant's average time. The average value for each tool is indicated in the colored boxes. The colors indicate relative performance with red indicating the worse (longest time) and green the best. The standard deviation of each tool is shown under the averages. Note the large variances of the raw values (left) vs the normalized values (right). At the bottom of each table is a matrix of Two Sample t-Test values of t. These values indicate the likelihood that there is a statistical difference between the average performance of the tools. For the illustrated sample size, a t-value of greater than 1.71 indicates a statistical difference in the means of two tools. Note that with an increase in sample size the t-value indicating a significant difference decreases to 1.65.

A.1.2 Data Normalized and Grouped by Test Metric

Figure A.4 shows the data normalized and grouped by task. The top of the figure is the normalized performance of each tool. At the bottom of each column of numbers are six tool to tool comparisons (A vs. C for example). Each tool pair is subjected to a difference of means test using a Two Sample t-Test [64]. When using the t-Test the degrees of statistical freedom is the number of samples in each of the populations means (n_1 and n_2) minus 2 (i.e. $DOF = n_1 + n_2 - 2$). Because each combination of task and metric (Ring Transfer, % of Average Time, forward and back) has 32 data points, a comparison of two tools has 62 DOF. To indicate a difference in mean performance when comparing two tools the magnitude of the calculated t-value must be greater 1.67. This is the t-value indicating a 95% confidence for a comparison with 62 DOF. In Figure A.4, comparisons which fail to meet the threshold for statistical significance are marked with a strike through and red highlight.

The performance of the trained surgeons and naive users was separated and is shown in Figure A.5.

Participant	Surgeon 1=Yes	Test Order 1=A, 2=B, 3=C, 4=D				Tool: A																	
						15						-15						W					
		1st	2nd	3rd	4th	1	2	3	4	5	6	7	8	9	10	11	12	13	14	15	16	17	18
1	0	1	3	4	2	309	31	14	299	17	14	378	89	18	315	69	14	524	33	12	555	22	12
2	0	3	2	1	4	203	67	17	129	35	12	153	33	17	146	41	14	264	26	7	575	71	18
3	0	4	2	1	3	359	1	1	387	7	4	317	2	5	311	1	1	442	0	2	305	2	1
4	0	1	2	4	3	205	23	11	317	26	9	275	0	2	248	15	6	501	5	5	317	7	5
5	0	1	3	4	2	156	30	7	164	61	11	148	49	7	203	87	14	296	5	9	215	42	9
6	0																						
7	0	2	3	1	4	300	34	13	317	38	13	253	35	10	274	43	18	472	118	21	298	36	6
8	1	4	1	3	2	107	15	7	174	29	10	120	8	6	119	13	4	247	0	1	159	14	4
9	1	1	3	4	2	150	3	3	132	14	2	109	1	3	77	15	5	344	71	9	240	0	0
10	1	3	2	4	1																		
11	1	2	4	3	1	161	21	6	198	38	14	218	21	5	130	60	4	353	49	15	418	11	4
12	0	1	3	2	4	303	55	23	298	24	9	180	75	11	302	97	12	323	0	0	225	8	4
13	0	1	4	3	2	323	159	20	156	63	12	296	76	11	216	114	14	686	144	17	440	96	8
14	1	3	1	2	4	113	27	7	116	54	5	169	81	11	96	37	5	752	3	5	626	88	11
15	1	1	2	3	4	117	17	2	170	38	16	207	17	5	269	52	17	278	4	6	325	18	4
16	1	2	1	3	4	117	4	3	94	4	5	115	7	4	114	19	8	187	0	0	120	1	1
17	1	3	2	1	4	117	19	6	127	23	5	178	95	8	138	57	4	286	17	4	250	26	6
18	1	1	2	4	3	102	2	2	110	8	7	140	27	9	128	31	3	357	7	3	363	0	2

Participant	Surgeon 1=Yes	Test Order 1=A, 2=B, 3=C, 4=D				Tool: B																	
						15						-15						W					
		1st	2nd	3rd	4th	1	2	3	4	5	6	7	8	9	10	11	12	13	14	15	16	17	18
1	0	1	3	4	2	239	15	7	242	22	13	331	25	14	211	39	12	270	7	5	240	33	8
2	0	3	2	1	4	205	22	13	180	26	14	140	27	13	110	42	10	419	25	14	416	22	7
3	0	4	2	1	3	306	7	4	331	3	2	284	30	14	278	18	6	342	10	4	340	0	0
4	0	1	2	4	3	206	15	4	393	35	11	319	31	13	272	5	5	359	4	19	394	17	12
5	0	1	3	4	2	153	13	7	255	30	21	212	94	9	159	84	15	332	14	8	385	82	10
6	0																						
7	0	2	3	1	4	419	38	14	466	63	20	373	70	22	334	31	14	340	7	6	485	40	22
8	1	4	1	3	2	99	8	6	98	22	5	115	25	4	113	26	6	201	0	1	200	1	3
9	1	1	3	4	2	92	10	7	87	9	8	80	2	2	59	6	5	148	13	3	116	7	13
10	1	3	2	4	1	76	12	3	164	17	5	201	39	7	335	31	9	394	11	6	226	2	1
11	1	2	4	3	1	256	40	15	208	14	5	177	12	3	122	20	12	498	39	9	518	10	7
12	0	1	3	2	4	228	42	14	267	41	15	220	30	11	221	23	6	215	0	1	233	0	1
13	0	1	4	3	2	136	58	7	105	41	7	175	62	14	137	44	13	175	12	4	255	0	1
14	1	3	1	2	4	94	21	8	97	21	8	120	6	5	118	12	3	350	9	4	379	8	3
15	1	1	2	3	4	132	7	4	113	8	4	228	12	6	189	8	5	214	3	1	218	0	0
16	1	2	1	3	4	172	6	3	108	3	2	191	14	5	124	20	10	162	16	3	117	2	2
17	1	3	2	1	4	172	63	5	141	12	3	207	76	14	177	37	6	410	7	3	335	2	4
18	1	1	2	4	3	118	3	4	126	30	6	199	21	9	171	37	8	345	0	0	325	2	1

Figure A.2: Test Raw Data, Hemostat Grip Tool (A) and Prototype with parallel mapping (B). Tools are labeled as A-D. The Tasks are labeled as "15", "-15", and "W" for the two sinusoidal tasks and the wire transfer tasks respectively. The timing system reported in 1/10th seconds so time data is in deciseconds. For a given task there are two sets of three metrics, one set for the forward run, one set for the return run. "Surgeon=1" indicates the participant is a surgeon vs naive user. Test order indicates the order the tools were presented to the user (1=A, 2=B, 3=C, 4=D). For example, participant two shows a tool order of [3 2 1 4]. This indicates the order of presentation with tool C first and tool D last.

Participant	Surgeon 1=Yes	Test Order 1=A, 2=B, 3=C, 4=D				Tool: C																	
						15						-15						W					
		1st	2nd	3rd	4th	1	2	3	4	5	6	7	8	9	10	11	12	13	14	15	16	17	18
1	0	1	3	4	2	243	94	19	295	169	23	325	58	18	299	105	29	300	14	2	342	23	29
2	0	3	2	1	4	96	41	9	205	96	18	232	46	16	276	101	22	834	154	27	843	326	19
3	0	4	2	1	3	330	21	9	366	9	8	285	10	7	568	37	10	372	5	4	510	22	11
4	0	1	2	4	3	292	65	16	306	36	6	256	67	24	274	12	5	462	10	8	472	0	1
5	0	1	3	4	2	165	83	13	132	52	18	133	69	8	179	66	13	412	12	5	357	78	16
6	0																						
7	0	2	3	1	4	129	89	7	374	226	23	328	180	17	165	134	9	463	85	16	265	12	7
8	1	4	1	3	2	160	35	12	211	56	11	185	81	11	171	38	8	246	13	4	266	13	6
9	1	1	3	4	2	107	23	11	126	26	10	110	8	5	64	27	6	210	14	6	176	16	9
10	1	3	2	4	1	172	45	12	111	24	9	141	42	10	120	49	11	524	1	3	423	15	6
11	1	2	4	3	1	187	78	7	202	50	12	241	117	17	178	48	14	412	22	16	394	96	22
12	0	1	3	2	4	308	50	15	344	22	12	261	105	13	424	91	34	258	3	4	442	77	16
13	0	1	4	3	2	272	156	17	193	102	10	128	62	10	187	79	9	284	71	15	274	52	11
14	1	3	1	2	4	201	22	9	109	29	6	320	43	20	160	26	7	675	7	1	502	0	0
15	1	1	2	3	4	211	19	7	215	36	13	199	35	16	247	2	4	310	26	7	279	10	7
16	1	2	1	3	4	99	42	8	123	17	8	85	23	6	113	20	8	98	9	3	142	22	5
17	1	3	2	1	4	181	38	8	141	43	2	176	35	12	172	48	8	305	11	4	275	56	18
18	1	1	2	4	3	178	30	8	166	9	6	195	20	10	211	14	6	365	11	4	439	5	3

Participant	Surgeon 1=Yes	Test Order 1=A, 2=B, 3=C, 4=D				Tool: D																	
						15						-15						W					
		1st	2nd	3rd	4th	1	2	3	4	5	6	7	8	9	10	11	12	13	14	15	16	17	18
1	0	1	3	4	2	218	32	16	275	61	19	267	65	15	229	24	10	215	4	5	190	6	5
2	0	3	2	1	4	94	38	14	109	47	13	146	62	18	130	45	12	387	7	8	306	25	13
3	0	4	2	1	3	225	51	11	318	10	7	310	21	9	334	30	13	672	0	0	584	0	1
4	0	1	2	4	3	262	7	6	254	20	6	267	27	12	188	14	8	421	1	2	367	0	0
5	0	1	3	4	2	156	55	11	162	39	9	209	42	10	134	51	12	236	19	6	272	22	11
6	0																						
7	0	2	3	1	4	166	37	10	194	53	11	118	69	6	244	18	12	499	43	23	282	55	12
8	1	4	1	3	2	170	7	4	174	13	6	172	4	3	159	8	5	293	6	5	169	5	4
9	1	1	3	4	2	84	0	0	113	0	2	143	3	1	129	0	1	152	9	3	170	7	2
10	1	3	2	4	1																		
11	1	2	4	3	1	158	11	8	223	9	4	121	12	7	163	12	4	306	2	3	335	22	8
12	0	1	3	2	4	307	51	15	236	34	15	282	37	14	308	29	7	247	6	6	262	3	2
13	0	1	4	3	2	226	123	19	180	100	10	129	78	7	161	77	12	279	11	6	258	16	7
14	1	3	1	2	4	109	20	6	108	13	6	116	1	1	89	2	3	307	0	1	210	0	0
15	1	1	2	3	4	140	2	3	155	7	4	124	5	3	180	6	3	250	4	3	273	2	5
16	1	2	1	3	4	74	9	4	94	4	6	80	10	4	74	15	5	182	7	4	173	3	2
17	1	3	2	1	4	172	24	7	147	7	3	198	44	6	131	16	4	336	0	0	266	0	0
18	1	1	2	4	3	140	1	2	167	7	5	121	9	3	163	1	1	262	3	1	275	0	0

Figure A.3: Test Raw Data, Pistol Grip Tool (C) and Prototype with anti-parallel mapping (D). Tools are labeled as A-D. The Tasks are labeled as "15", "-15", and "W" for the two sinusoidal tasks and the wire transfer tasks respectively. The timing system reported in 1/10th seconds so time data is in deciseconds. For a given task there are two sets of three metrics, one set for the forward run, one set for the return run. "Surgeon=1" indicates the participant is a surgeon vs naive user. Test order indicates the order the tools were presented to the user (1=A, 2=B, 3=C, 4=D). For example, participant two shows a tool order of [3 2 1 4]. This indicates the order of presentation with tool C first and tool D last.

Task:	W-Test at +15*			W-Test at -15*			Ring Transfer Test		
Tool	% of Avg Time	% of Avg Error Time	% ofAvg # of Errors	% of Avg Time	% of Avg Error Time	% ofAvg # of Errors	% of Avg Time	% of Avg Error Time	% ofAvg # of Errors
A: Hemostat	**102.2%**	**88.3%**	**96.3%**	**101.1%**	**105.7%**	**91.2%**	**111.0%**	**123.3%**	**97.8%**
B: Proposed, Parallel	**99.5%**	**67.7%**	**88.5%**	**96.5%**	**77.2%**	**97.2%**	**90.1%**	**77.2%**	**97.2%**
C: Pistol	**108.0%**	**170.2%**	**128.1%**	**112.1%**	**153.6%**	**137.2%**	**108.4%**	**153.6%**	**137.2%**
D:Propsed, anti-paral.	**90.4%**	**73.9%**	**87.1%**	**90.3%**	**63.5%**	**74.4%**	**90.5%**	**63.5%**	**74.4%**
t-Values, Tool Comparisons									
t-A:C	4.33	6.99	6.21	5.11	2.80	6.04	~~-0.97~~	~~0.58~~	1.93
t-B:C	4.43	9.30	8.82	6.85	5.63	5.35	13.31	1.82	2.00
t-D:C	14.49	7.18	9.37	9.81	6.60	8.82	11.15	2.23	3.34
t-B:A	~~1.51~~	3.54	1.73	3.31	2.55	~~-1.31~~	8.31	~~1.28~~	~~0.05~~
t-D:A	12.80	~~1.50~~	2.08	8.38	3.74	4.25	7.74	1.75	2.34
t-D:B	5.60	~~-0.71~~	~~0.36~~	4.20	3.17	6.19	~~-0.30~~	~~1.11~~	2.50

Figure A.4: First level of user test data reduction. The top half of the table includes the normalized relative performance of each tool for each task. The forward and reverse runs of each task are group. The percentages are the performance of the tool with respect to the average performance of all four tools for that particular task. The data is color scaled from red (worst performance) to green (best performance). The color is on a gradient so two similar results will have similar shading. The shading in this area of the plot does not indicate statistical significance. Bottom half of the chart indicates the t-scores for comparison between a pair of tools. The tools being compared, A vs. C for example, are indicated in the first column. With 16 participants and a forward and reverse run for each task there are 32 data points per tool for each datum type (% of Average Time, % of Average Error Time, % of Average Number of Errors). A comparison of two populations with a samples size of 32 each results in 62 statistical degrees of freedom. With 62 DOF a t-value greater than 1.67 (or less than -1.67) indicates a difference in means with confidence level of 95%. All tool comparisons which failed to meet this level are highlighted in red with a strike through the value.)

	Surgeons All Tests per Metric			Naive Users All Tests per Metric		
Tool	% of Avg Time	% of Avg Error Time	% ofAvg # of Errors	% of Avg Time	% of Avg Error Time	% ofAvg # of Errors
A: Hemostat	**102%**	**125%**	**101%**	**107%**	**89%**	**90%**
B: Prototype, Parallel	**94%**	**73%**	**93%**	**96%**	**74%**	**96%**
C: Pistol	**111%**	**170%**	**149%**	**109%**	**150%**	**121%**
D:Prototype, anti-paral.	**93%**	**37%**	**59%**	**88%**	**93%**	**96%**
t-Values, Tool Comparisons						
t-A:C	6.29	1.72	5.19	1.13	4.04	4.70
t-B:C	11.64	6.53	7.76	10.92	5.02	3.58
t-D:C	13.61	9.25	13.07	20.33	3.80	3.78
t-B:A	6.00	2.30	1.11	9.41	2.47	-1.63
t-D:A	7.81	3.98	5.99	18.34	-0.70	-2.65
t-D:B	1.27	9.61	8.49	9.67	-3.27	-0.12

Figure A.5: Tool performance based on user type. Surgeons as a group were more consistent in their performance. The overall ranking of the tools was the same for both groups.

Appendix B

Static Balance Mechanisms

B.1 Balance via Cam and Follower

The use of cams to turn rotary motion into linear displacements is perhaps most commonly associated with automobile engines. As anyone who has attempted to change the timing belt on a car can describe, the cam follower can be used to apply force to the cam lobe as well as the reverse. Hilpert [43] illustrated the use of a cam mechanism used to energy balance a pendulum through 360° of rotation. In principle the mechanism shown by Hilpert and one needed to balance a continuum joint are similar with the only difference being a mild difference in the desired output torque (linear over a limited range vs sinusoidal).

Figure B.1 illustrates a cam balancing a singe degree of freedom device. A two DOF solution can be created by the use of a pair of cams operating on orthogonal axes and interconnected via a gimbal mechanism. The sum of the energy transfered from the pair of cams would equal the elastic energy of the deflected continuum structure.

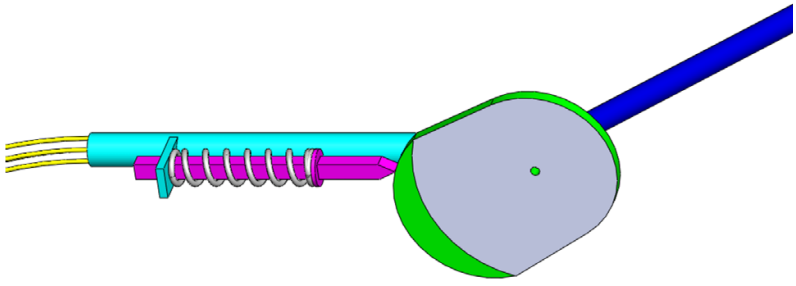

Figure B.1: Conceptual cam balance system. Cam surface rotates with control handle (right).

The cam and follower mechanism are used to translate rotation of the control joint into displacement of a follower and spring. Based on the previous assumption that the continuum joint behaves as a linear rate torsional spring, the equations for joint effective torque (the torque the continuum joint applies to the control handle) and energy stored in the continuum joint are:

$$\begin{aligned} \tau_c &= k_c \alpha \\ U_c &= \frac{1}{2} k_c \alpha^2 \end{aligned} \tag{B.1}$$

A cam profile which balances the energy of the joint must satisfy the assumption of constant energy in the system.

$$U_t = \frac{1}{2} k_c \alpha^2 + \frac{1}{2} k_s x^2 \tag{B.2}$$

The terms of the joint, k_c and α are based on the specifics of the continuum joint to be balanced. The required displacement of the balancing spring can be calculated based on assumed values of spring rate and total energy in the system, k_s and U_t. This clearly leads to a large number of possible cam profiles thus it is useful to optimize or reduce the number of potential profiles via an additional series of constraints.

B.1.1 Additional Cam Constraints

To reduce the range of possible cam profiles a series of constraints are added to the design. These constraints include design rules and assumptions regarding realistic limits on the size of the mechanism. The final series of constraints will look at the

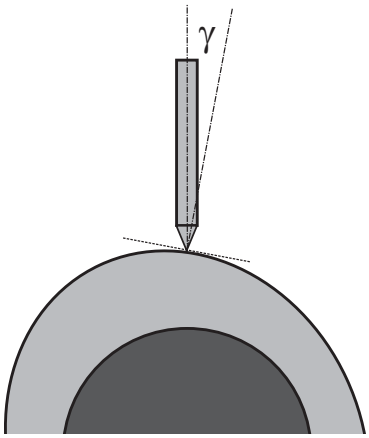

Figure B.2: Thrust angle between follower and cam, γ.

sensitivity of the design to mechanical tolerances of the parts of the system as a percentage of the total energy in the system.

First applied is a constraint on the maximum cam pressure angle. Moon suggests a maximum cam pressure angle of 30° and offers a formula relating cam torque, cam follower force and the pressure angle [66]. Thus any solution resulting in a profile with a pressure angle over 30° is discarded from consideration. The pressure angle equation, from Moon, is below.

$$\tau = rf\tan(\gamma) \tag{B.3}$$

Where τ is the torque reaction of the cam, r is the local radius of the cam, f is the force the follower applies to the cam and γ is the pressure angle or angle between the follower and a line normal to the contact surface (Figure B.2).

Solve for the maximum pressure angle based on the assumed values of k_s, U_t the

system torque equation and equation B.3. Substitute in $f = k_s x$.

$$0 = k_c \alpha + r k_s x \tan(\gamma) \tag{B.4}$$

It can be seen that the highest torque applied by the cam and follower will occur when α is at its maximum. Thus the value of γ will be calculated at the maximum joint angle α, 45° in the example case. This equation adds the radius of the cam, r, to the previously assumed values of k_s and U_t.

Given three variables a family of preferred options were found by considering the practical manufacturing constrains of the system. First the radius of the cam was set to 50 mm. As can be seen in Equation B.4 an increase in r results in a reduction in the other cam related values, k_s, x and/or the pressure angle. A reduction in spring rate or spring displacement results in a desirable drop in stored spring energy and thus total system energy. Thus r is set to its maximum practical limit based on either a maximum base diameter or peak cam diameter. In the example problem the peak base cam diameter was picked at 50 mm. This means $r = 50$mm when the cam is deflected to its maximum value, 45° in this example.

Rather than working in terms of the remaining two variables k_s and U_t, it is convenient to work in terms of initial displacement of the spring and spring rate. This puts the results in terms of physical design lengths rather than in the more abstract context of total system energy. When the cam angle, α, is 0° it can be seen

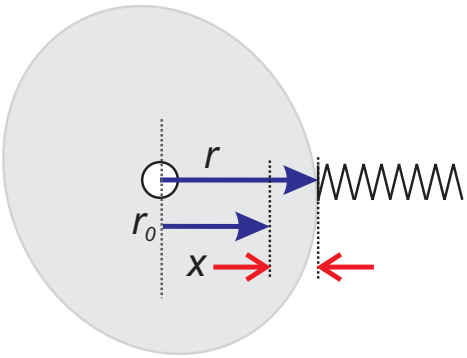

Figure B.3: Cam spring compression and the zero compression radius, r_0. If the balance spring is thought of as acting directly on the cam surface then the displacement of the spring, x, is the difference between the cam radius r and a theoretical cam radius where the spring is uncompressed r_0.

from equation B.2 that the total system energy is

$$U_t = \frac{1}{2} k_s x^2 \tag{B.5}$$

The spring displacement x can be expressed as a function of the cam radius and a theoretical cam radius r_0 where the spring would be uncompressed (Figure B.3). Note that because this radius represents only the spring's uncompressed state, not an expected configuration of the system it can have a negative value.

$$x = r - r_0 \tag{B.6}$$

The total energy in the system can be found by looking at the energy in the balance spring while the joint is in its straight, zero energy state. Thus r_0 has become our

independent variable in place of U_t.

$$U_t = \frac{1}{2}k_s(r - r_0)^2 \tag{B.7}$$

To optimize our design among the family of possible values of k_s and r_0 two things should be minimized, the total system energy and the tolerance of the system to manufacturing variations in its component parts. The typical tolerance of a manufactured spring is 10% of the stated rate. The stacked tolerance of the cam, follower and follower support is estimated to be 0.2 mm in total. These values are assumed but not based on a specific design. For a specific design, both of these estimates would be replaced with design values. The impact of these tolerances on the total system energy can be found by substituting equation B.6 into B.2 and then taking the partial derivatives with respect to k_s and r_0.

$$U_t = \frac{1}{2}k_c\alpha^2 + \frac{1}{2}k_s(r - r_0)^2 \tag{B.8}$$

Take the derivatives with respect to r_0 and k_s to get the change in system energy based on the manufacturing tolerances of the input variables.

$$U_{tolerance} = \frac{dU_t}{dr_0} + \frac{dU_t}{dk_s} = (r - r_0)k_s dr_0 + \frac{1}{2}(r - r_0)^2 dk_s \tag{B.9}$$

To select the optimum values for uncompressed spring position, r_0, and the spring rate, k_s a range of possible values for each variable were tested. The uncompressed spring position ranged from -20 mm to 45 mm ($r_0 - 5$ mm). The possible spring

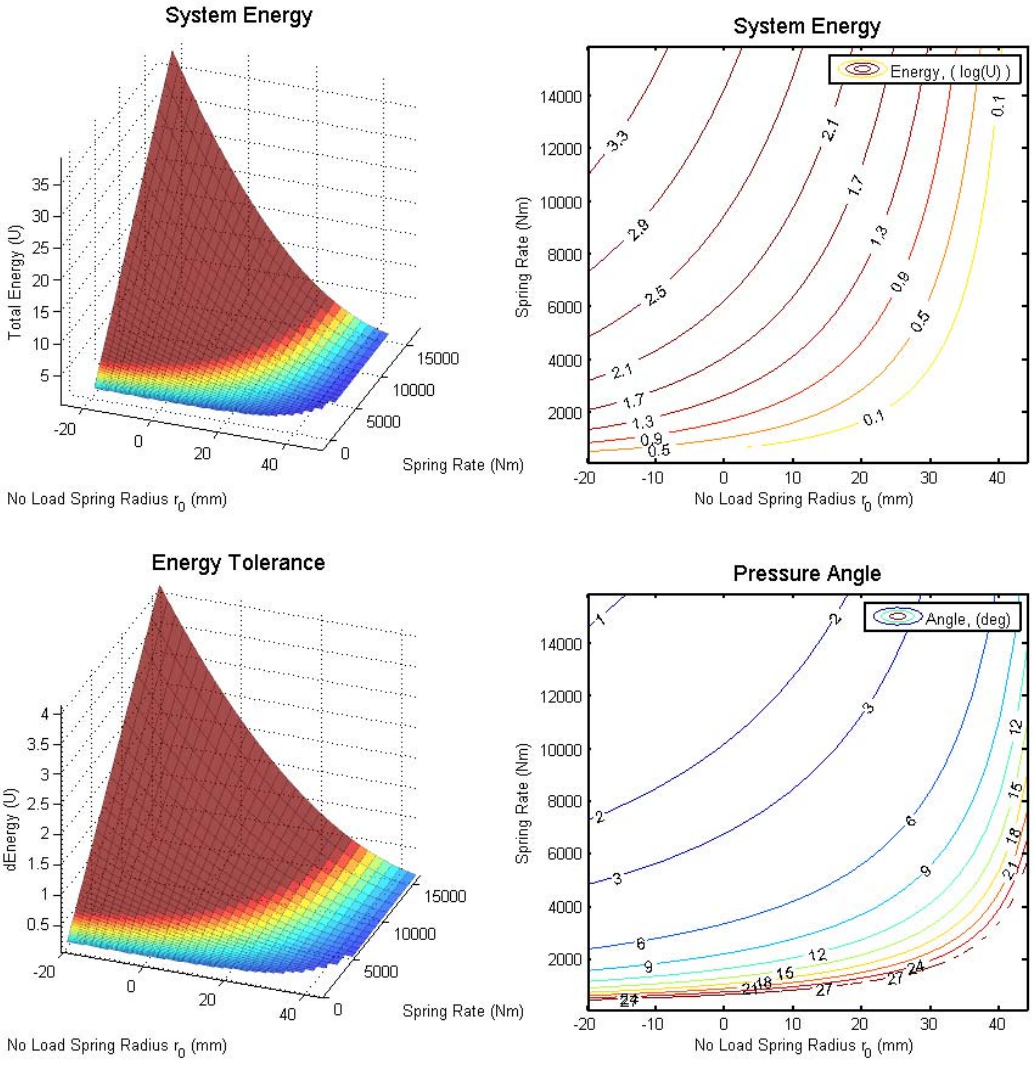

Figure B.4: System properties for a range of r_0 lengths and spring rates. System energy is shown in the upper two plots. Lower left shows the change in system energy due to manufacturing tolerance. Lower right shows the maximum cam pressure angle. Configurations requiring a pressure angle over 30° are removed from the data sets.

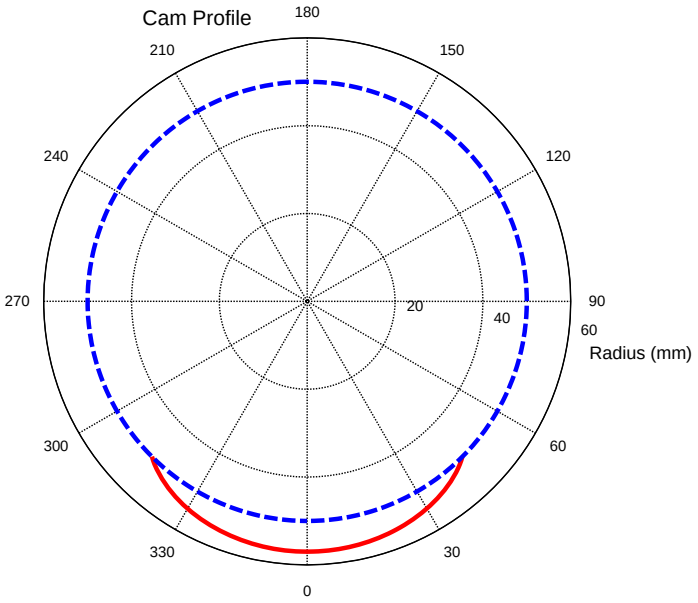

Figure B.5: A cam profile based on the optimal configuration from the data shown in Figure B.4. The dashed line represents the specified base cam diameter. The solid line illustrates the rise above the base diameter over a range of $\pm 45°$.

rates ranged from 100 to 15850 n/m (0.571 to 90.5 lb/in). The system energy, system energy tolerance and maximum cam pressure angles are shown in Figure B.4. The point where the energy tolerance is lowest occurs where the spring free radius is 44 mm and the spring rate is 5250 n/m (30 lb/in). This is also a low total energy point and is thus selected as the optimal inputs for the theoretical cam design.

With values for base cam diameter, spring preload/zero load radius and spring rate selected, a spring curve can be generated by solving equation B.8 for r over the range of cam angles, α. The resulting profile are shown in figure B.5.

B.2 Wrapping Cam

The previously described cam and follower was shown to provide theoretical, ideal balance of the continuum joint. However, high contact forces and sliding contact

can reduce the practical effectiveness of such a cam even when fitted with a roller follower. Wrapping cams are, in effect, variable radius capstan drives. They have no sliding friction and relatively low surface contact forces. As with the cam and follower example, the following example describes a single DOF cam solution. A two degree of freedom system can be created with a pair of orthogonal cams. It is noted that Kumar et al. [53] [54] used wrapping cams to show the balance of robotic arms though their cam profile derivation assumed the tension cable which wraps around the cam was anchored at a distant point thus the change in angle of the cable with an increase in cam diameter could be ignored. The method used in this work is based on that of Tidwell et al. [99] and accounts for this change in tension cable angle.

B.2.1 Wrapping Cam Requirements

The fundamental layout of the wrapper cam balance system is shown in figure B.6. As with the other candidate mechanisms the forces required to deflect the distal joint act like a linear rate torsional spring connected to the control handle. Because wrapper cams are operated in tension an opposing pair of cams and springs are situated on either side of the device with two springs to provide tension for the cam cables. When the control handle is moved away from center, for example to the right as illustrated, the spring on right decreases in length (retracts) while releasing stored energy. The opposing spring on the left increase in length (extends) while storing energy. By the definition of a free energy system the loss of energy in the right hand spring must equal the combined gains in energy in the joint and left hand spring. Thus the cam profile of the retracting spring, noted with the subscript 'r', must be shaped such that

it balances the sum of the joint torque and the opposing left hand, extending spring, noted with the subscript 'e'. The joint angle is expressed by the angle α which is 0 when the joint is straight. When $\alpha = 0$ the lengths of the two springs are identical with an extension of x_o. The subscript 'o' is also used to refer to other cam or system parameters at $\alpha = 0$.

The energy and torque balance requirements can be expressed in the following equations:

$$\sum U = U_t = U_c + U_r + U_e \tag{B.10}$$

and,

$$\sum T = 0 = T_c + T_r + T_e \tag{B.11}$$

It can be seen that when the control is to the right, effective torque of the left spring and the joint are in the same direction. Thanks to the symmetric layout when the control is moved in the opposite direction, to the left, the spring on the right is the one creating torque in the same effective direction as the joint. The result is that a single side of the cam must have two profiles, one when the balance spring is extended from its neutral state and one when it is retracted. The two profiles are indicated on the side of Figure B.6. Because the two profiles share a single cam lobe they must share a common point when the joint in undeflected, $\alpha = 0$.

Equation B.11 dictates that for the system to remain balanced the sum of torques must remain zero over the range of joint angles. The torque profile of the joint is dictated by the design of the joint to be balanced. The torque profiles and magnitudes of the two opposing cams need to be found to determine the cam profiles. Figures B.7

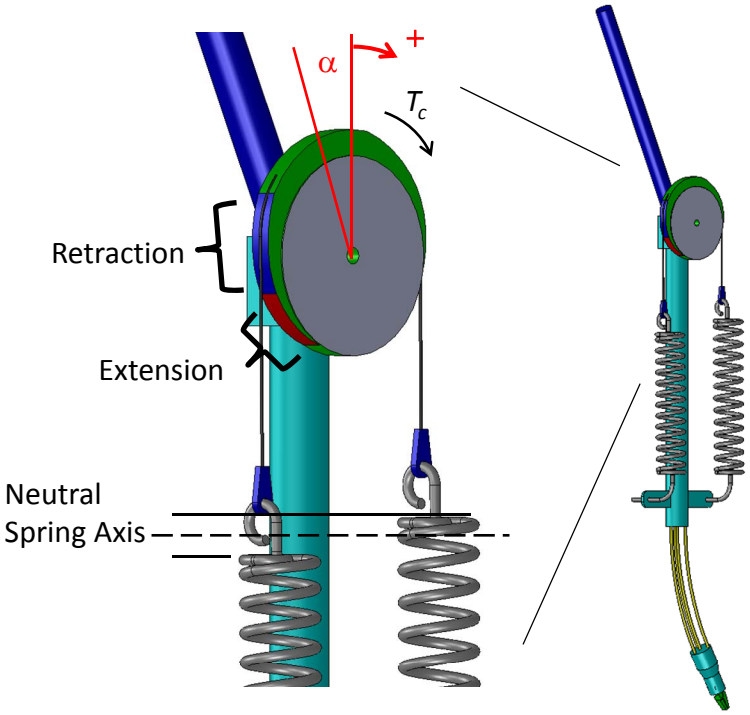

Figure B.6: Conceptual layout of a flex joint balanced with an opposed pair of wrapping cams. A mechanism (not illustrated) converts the deflection of the joint at the bottom of the tool into rotation of the control handle at the top of the tool. The restorative torque of the joint is indicated as an effective torque, T_c applied by the handle to the cam. The angle α is the deflection of the control handle and the rotation of the cam with respect to the main tool shaft. The enlargement indicates the neutral position of the springs and their extended and retracted states with respect to the neutral position. The red and blue cam surfaces indicate the portions of the cam which are active when the spring is extended or retracted with respect to the neutral state.

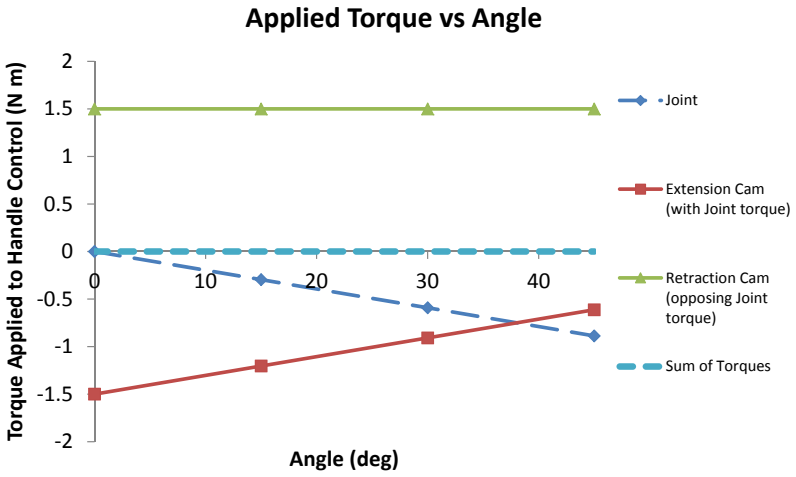

Figure B.7: Torque applied to the control joint by the joint mechanism and the two opposing wrapping cam mechanisms. As illustrated a constant torque cam is used to balance the sum of the rising joint torque and a falling torque cam.

and B.8 illustrate examples of balanced torque profiles. These are cam profiles that satisfy equation B.11 over the range of α. The family of possible cam profiles can be reduced with a few assumptions. First, since the joint torque is effectively a linear rate spring, the torque profiles of the balancing cams can be limited to linear profiles. Second, because each cam lobe consists of effectively an extension and retraction lobe, the two lobes must share a common cable tangent point when the joint is straight, $\alpha = 0$.

As with the cam and follower system, this system must be symmetric and apply a zero net torque to the joint control when the joint angle, α, is zero. In order to maintain some tension on the control cables at all times the joint springs must have some preload when $\alpha = 0$. As previously mentioned each side of the cam is considered as two profiles which must meet when $\alpha = 0$. To ensure the extension and retraction cam profiles of a given side of the device meet at $\alpha = 0$ the design of the

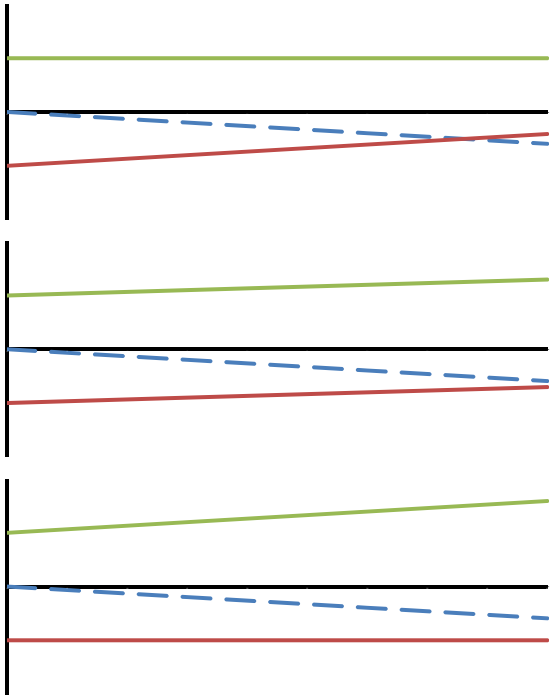

Figure B.8: Examples of three possible cam profiles which meet the sum of torques requirement. The vertical axis is torque while the horizontal is joint angle. The top profile is a cam with a constant balancing torque used to balance a the joint plus falling rate cam. The bottom profile uses a constant rate cam in the same direction as joint and a rising rate cam opposing the two. The middle profile is a balance of the other two profiles

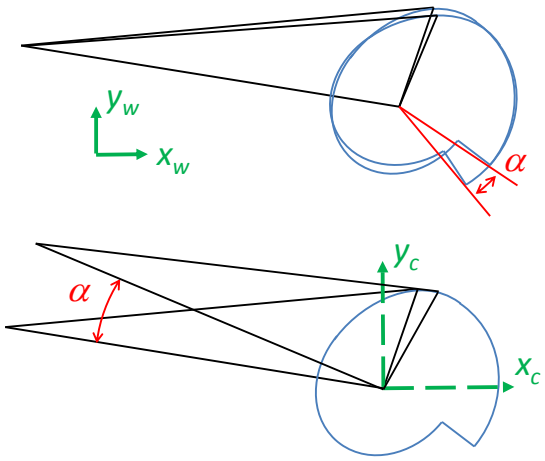

Figure B.9: Cam rotation shown with respect to the world frame and the local cam frame.

profiles and the associated parameters which determine the point where the wrapping cable contacts the cam, the tip of vector P as described in the next section, must be reviewed.

B.2.2 Cam Profile Generation

The method used to generate cam profiles is based on that presented by Tidwell et al. [99]. The relationship between a cam and an anchored, spring loaded tension wire is illustrated in figures B.10 and B.9. The rotation of the cam is expressed by the angle α. Rather than considering the cam as rotating with respect to a world frame, the cam profile is synthesized with respect to the local frame of the cam with an origin at the point of rotation. This is illustrated in figure B.9

The cam profile is found by locating the end of vector P over the working range of cam angle α. This is done following the methods outlined by Tidwell et al. [99]. The line l is always tangent to the cam at the end point of vector P. As the mechanism is

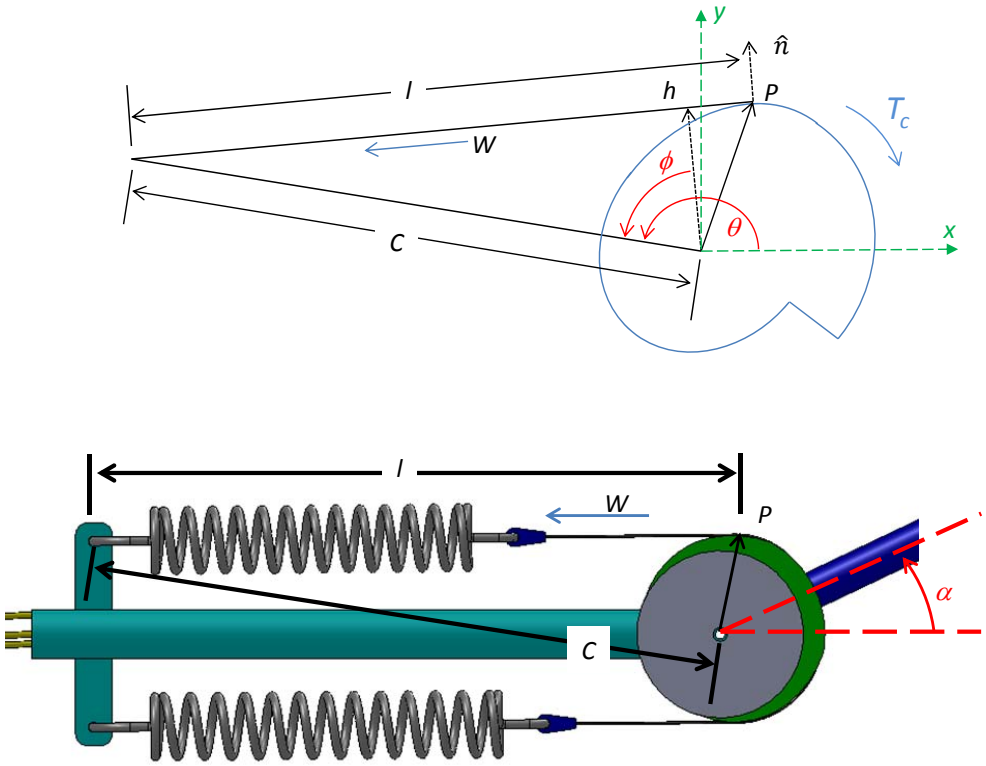

Figure B.10: The parameters of the wrapping cam. C, l are lines with a respective length. P is a vector from the cam origin to the point of contact between cam and cable. The vector h is the normal vector between the line of the cable and the cam origin while $\hat{n}$ is a unit vector in the direction of h located at P. W is the tension in the cable. Effective cam torque, T_c, is equal to Wh and is the torque applied to the cam system needed to balance the system. The angle α is the rotation of the cam with respect to the neutral position of the mechanism and $\alpha = 0$ when the joint is straight. θ is the angle of line C with respect to the cam x-axis and is related to α by $\theta = \alpha + constant$. ϕ is the angle from h to C.

rotated about the cam (Figure B.9) the tip of P travels along the surface of the cam. At any time the direction of $dP/d\theta$ must be along the line l. The vector h is normal to the line l. Since the unit vector $\hat{n}$ is in the same direction as h, the tangent vector $dP/d\theta$ is orthogonal to $\hat{n}$.

$$\frac{dP}{d\theta} \cdot \hat{n} = 0 \tag{B.12}$$

The direction of $\hat{n}$ is expressed in complex polar form..

$$\hat{n} = e^{i(\theta-\phi)} \tag{B.13}$$

The vector P can be expressed as a loop from the cam origin.

$$P = Ce^{i\theta} + le^{i(\theta-\phi-\pi/2)} \tag{B.14}$$

The unknown terms in the above equation are l and ϕ which must be found to calculate P. Differentiating equation B.14 with respect to cam rotation θ yields:

$$\frac{dP}{d\theta} = iCe^{i\theta} - i\frac{dl}{d\theta}e^{i(\theta-\phi)} + l\left(1 - \frac{d\phi}{d\theta}\right)e^{i(\theta-\phi)} \tag{B.15}$$

Substituting equations B.13 and B.15 into B.12 and solving for length l yields:

$$l = \frac{C\sin(\phi)}{1 - \frac{d\phi}{d\theta}} \tag{B.16}$$

To solve for ϕ start by defining h. The torque required of the cam at any angle can

be expressed as a function of θ, and the cam torque, $T_c(\theta)$. The tension on the cable is also expressed as a function of θ, $W(\theta)$. Because torque is a force at a distance, h can be expressed as a function of T_c and W:

$$h = \frac{T_c(\theta)}{W(\theta)} \quad \text{and} \quad \frac{dh}{h\theta} = \frac{1}{W}\frac{dT_c}{d\theta} - \frac{T_c(\theta)}{W(\theta)^2}\frac{dW}{d\theta}. \tag{B.17}$$

ϕ and its derivative are found next. From inspection of figure B.6:

$$\sin(\phi) = \frac{\sqrt{C^2 - h^2}}{C} \tag{B.18}$$

and

$$\phi = \cos^{-1}\left(\frac{h}{C}\right) \tag{B.19}$$

To solve for $d\phi/d\theta$ use the derivative of equation B.19 and equation B.28.

$$\frac{d\phi}{d\theta} = \frac{-1}{\sqrt{C^2 - h^2}}\frac{dh}{d\theta} \tag{B.20}$$

With the results of equations B.18 and B.12 substituted into B.16.

$$l = \frac{C^2 - h^2}{\sqrt{C^2 - h^2} + \frac{dh}{d\theta}} \tag{B.21}$$

With equations for $T_c(\theta)$ and $W(\theta)$ the vector P can found over the range of θ.

B.2.3 Finding the Cable Tension and Torque Profiles

Previously in Section B.2.1 it was stated that the extension and retraction cam profiles must share a common vector P when the joint is straight, $\alpha = 0$. In this section it will be shown that this constraint results in a requirement that the the slopes of the torque curves, $dT/d\theta$, must be equal at $\alpha = 0$. The middle torque vs. angle plot in Figure B.8 illustrates such a configuration. Taking this plot and extending the angle of joint rotation in the negative direction results in Figure B.11. The extension and retraction profiles associated with a single spring become one continuous profile rather than two profiles joined at a common point. While this equal slope at $\alpha = 0$ appears to be the trivial solution that results in identical P vectors, in this section the equal slope will be shown as a requirement of the solution rather than just a possible solution.

To show that $dT_e/d\theta \equiv dT_r/d\theta$, start by finding the equation for the length of the spring. For any given torque profile the force profiles of the associated springs can be found via an energy calculation. The change in energy of the spring must be equal to the change in energy of the cam profile. Thus the energy in a given spring is the sum of its energy at the initial length and the change in energy of the cam profile:

$$U_s = \frac{1}{2}k_s x_o + \int_{\alpha_o}^{\alpha_i} T_{cam}(\alpha) \tag{B.22}$$

where α_i is the current value of α. The length of a spring can be expressed as a

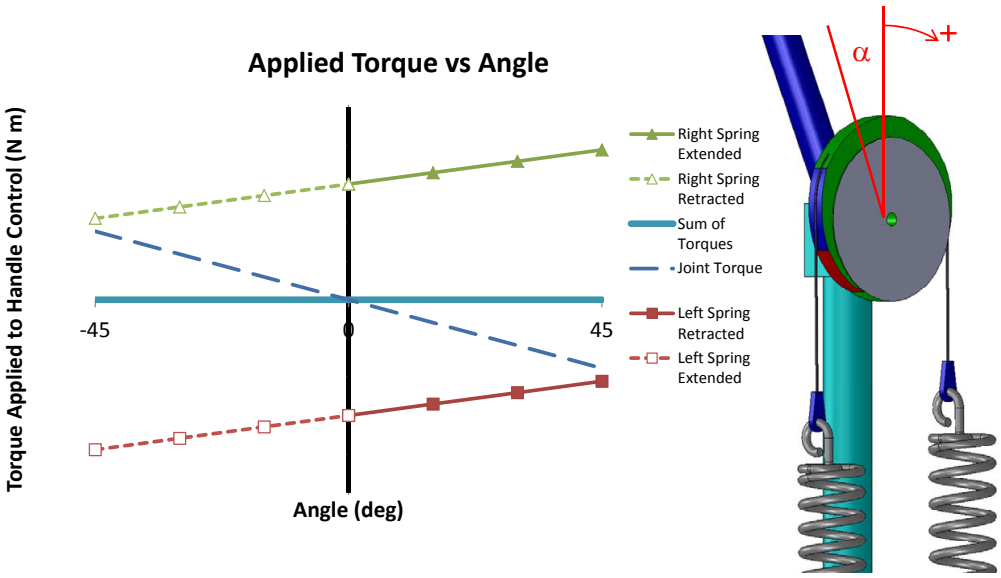

Figure B.11: A pair of continuous cam profiles balancing a joint. The slope of the cam profiles are equal and 1/2 the magnitude of the joint slope. The cam profiles represent a case where the extension and retraction profiles are part of a single continuous profile. The illustrated cam is shown with a negative angle and the right hand spring in a retracted state.

function of the joint angle.

$$x_s = \sqrt{\frac{2U_s}{k_s}} \tag{B.23}$$

For a single spring and cable to smoothly transition between the retraction and extension profiles $P_{extension} \equiv P_{retraction}$ at $\alpha = 0$.

$$\begin{aligned} P_e &= P_r \text{ at } \alpha = 0 \\ Ce^{i\theta} + l_e e^{i(\theta - \phi_e - \pi/2)} &= Ce^{i\theta} + l_r e^{i(\theta - \phi_r - \pi/2)} \end{aligned} \tag{B.24}$$

Due to symmetry at $\alpha = 0$, the values of x, C, h, T, θ and ϕ of the retraction and extension sides of equation B.24 are equal to one another. Thus the 'o' values, x_o, h_o

etc. can be substituted. After reduction, the length terms are left.

$$\begin{aligned} l_e &= l_r \text{ at } \alpha = 0 \\ \frac{C\sin(\phi_e)}{1-\frac{d\phi_e}{d\theta}} &= \frac{C\sin(\phi_r)}{1-\frac{d\phi_r}{d\theta}} \end{aligned} \tag{B.25}$$

Which again is evaluated at $\alpha = 0$ and thus can be reduced to:

$$\frac{d\phi_e}{d\theta} = \frac{d\phi_r}{d\theta} \tag{B.26}$$

Substituting equation B.12 and cancelling common terms (C, $h_e = h_r = h_o$)

$$\begin{aligned} \frac{C^2 - h_e^2}{\sqrt{C^2 - h_e^2} + \frac{dh_e}{d\theta}} &= \frac{C^2 - h_r^2}{\sqrt{C^2 - h_r^2} + \frac{dh_r}{d\theta}} \\ \frac{dh_e}{d\theta} &= \frac{dh_r}{d\theta} \end{aligned} \tag{B.27}$$

At $\alpha = 0$, $W_e(\theta) = W_r(\theta)$ and $T_e(\theta) = T_r(\theta)$. Equation B.12 is substituted into B.27. The non-derivative terms are equal and thus can be replaced with constants (Q_n).

$$\begin{aligned} \frac{1}{W}\frac{dT_c}{d\theta} - \frac{T_c(\theta)}{W(\theta)^2}\frac{dW}{d\theta} &= \frac{1}{W}\frac{dT_c}{d\theta} - \frac{T_c(\theta)}{W(\theta)^2}\frac{dW}{d\theta} \\ Q_1\frac{dT_c}{d\theta} - Q_2\frac{dW}{d\theta} &= Q_1\frac{dT_c}{d\theta} - Q_2\frac{dW}{d\theta} \end{aligned} \tag{B.28}$$

It can be seen that for the two cam profiles to have a common vector P when $\alpha = 0$ the above equation must be satisfied. The derivative $dW/d\theta$ relates cable tension and angle while $dT/d\theta$ is the slope of the designated torque curve. It can be shown that $dW_e/d\theta = dW_r/d\theta$ thus $dT_e/d\theta \equiv dT_r/d\theta$ for the two profiles to share a

common vector P when the joint is straight.

Start with Hook's law and substitute in B.23. Next set the constants common to both the retracting and expanding cams to a new constant Q_3:

$$\begin{aligned} W =& k_s\sqrt{\frac{2}{k_s}U_s} \\ W =& Q_3\sqrt{U_s} \end{aligned} \tag{B.29}$$

Taking the derivative with respect to θ:

$$\begin{aligned} \frac{dW}{d\theta} =& Q_3\frac{1}{2}U_s\frac{dU_s}{d\theta} \\ \frac{dW}{d\theta} =& Q_4\frac{dU_s}{d\theta} \end{aligned} \tag{B.30}$$

Because this is evaluated at $\alpha = 0$, the energy in the spring is that of the initial spring length, $1/2k_sx_o^2$. This allows a further consolidation of constants as U_s is identical for both springs; $Q_4 = (1/2)Q_2U_s$. The angles α and θ are offset from one another by θ_o; $\alpha = \theta + \theta_o$. From equation B.22 the $d\ U_s/d\theta$ evaluated at $\alpha = 0$ is:

$$\begin{aligned} \frac{dU_s}{d\theta}(\alpha = 0) =& \frac{d\left(\frac{1}{2}k_sx_o + \int_{\alpha_o}^{\alpha} T_{cam}(\alpha)\right)}{d\theta} \\ =& d\left(\frac{1}{2}k_sx_o\right)/d\theta + d\left(\int_0^0 T_{cam}\right)/d\theta \\ =& 0 + 0 \end{aligned} \tag{B.31}$$

The first terms are constants and thus drop out. The second term is an integral evaluated from $\alpha_o = 0$ to $\alpha = 0$ and is 0, thus $dU_s/d\theta = 0$ and from equation B.30,

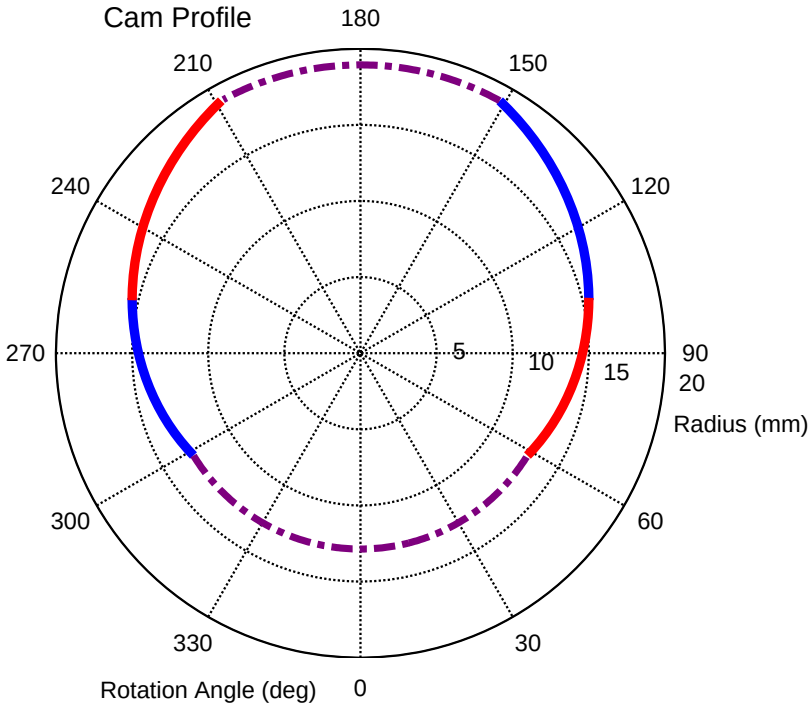

Figure B.12: Calculated cam profile. The blue profiles on opposite sides of the cam represent the pair of profile which balance the joint when turned in the clockwise direction while the red profiles are used in the counter-clockwise direction. The dashed lines are not part of the calculated profiles.

$dW/d\theta = 0$. When substituted into equation B.28 it is clear that for the two cam profiles to have a common vector P they must have a common $dT/d\theta$.

B.2.4 Wrapping Cam Profile

A cam configuration was created based on the previously described flex joint. The effective spring rate of the joint is 1.13 Nm with a working range of 45°. Dimensions and spring rates were assumed based on reasonable values and sizes for use in a small surgical tool. The radius of the cam in the undeflected state was fixed at 15mm. The cable anchors were 150.7mm from the cam axle. A spring rate of 2800 N/m (16.0 lb/in) was selected. The resulting cam profile is shown in figure B.12.

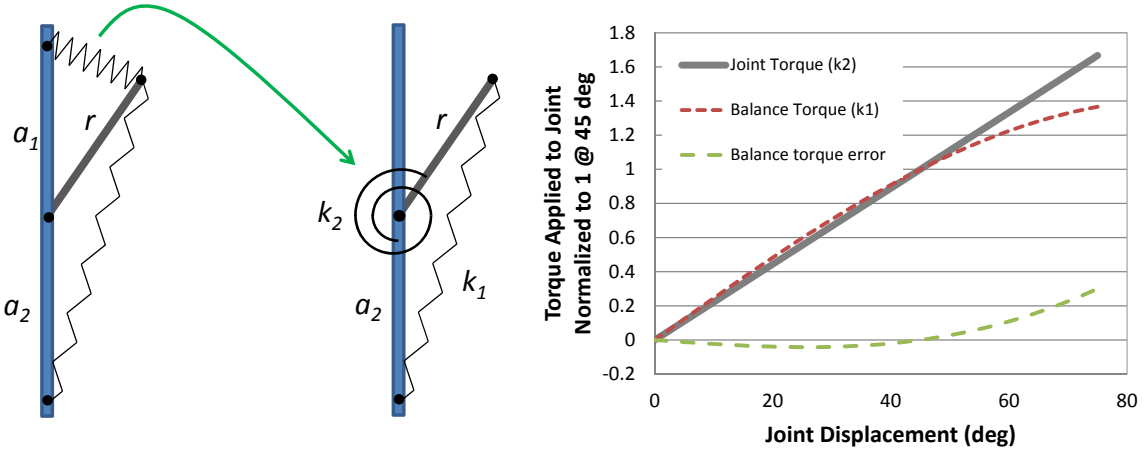

Figure B.13: A simplified elbow balance concept based on Herder's balanced crank mechanism. The upper spring in the left mechanism is replaced with a linear rate rotational spring representing the resulting torque of the actuated joint. The plot (right) indicates the effective torque applied to the joint vs. deflection angle. The spring rate k_1 is shown scaled to result in perfect balance at 0 and 45°. Note that the joint and spring mechanism torques are shown in the same direction.

B.3 Over Center Spring Mechanism

The basic mechanism presented by Herder can be used as a basis for a spring-lever balance mechanism for the device joint [38]. The upper spring of the basic balance mechanism shown in figure B.13 (left) is replaced by a torsional spring representing the effective joint torque profile $T_c(\alpha)$. Over a range of joint angles, α, the remaining lower spring applies an increasing torque to balance the joint torque. This is not a perfect balance and has a limited working range as the balance spring torque drops after approximately 45° or less depending on spring type and configuration.

The general performance shown in Figure B.13 assumed an idea spring where the free length of the spring has zero effective length when subjected to no load. Herder and te Riele have illustrated methods for creating functional zero length springs [98]

[39], a mechanical assumption required for Herder's basic balance mechanism. The addition of free length to the mechanism of Figure B.13 can have a significant, negative impact on the performance of the balance mechanism. This will be shown starting with a description of the equations which govern the system.

Figure B.14 shows the geometry of a simple over center spring mechanism. A torsion spring, τ_c at point a represents the effective torque of the continuum joint acting on the control handle, l_{ab}. The effective balance torque of the mechanism is,

$$\tau = F_s \frac{l_{cd}}{l_{bc}} l_{ab} \tag{B.32}$$

where F_s is the tension force of the spring and the ratio represents the portion of l_{bc} which is normal to the effect lever arm l_{ab}.

The total length of the spring, l_{bc} (free length plus extension) is:

$$l_{bc} = \sqrt{(l_{ac} + l_{ab}\sin\alpha)^2 + (l_{ab}\cos\alpha)^2)} \tag{B.33}$$

With the total spring length the tension in the spring is,

$$F_s = k_s(l_{bc} - X_o) \tag{B.34}$$

where k_s is the spring constant and X_o is the free length of the spring.

Line segment l_{cd} is normal to l_{ab}. Thus its length is:

$$l_{cd} = l_{ac}\sin\alpha \tag{B.35}$$

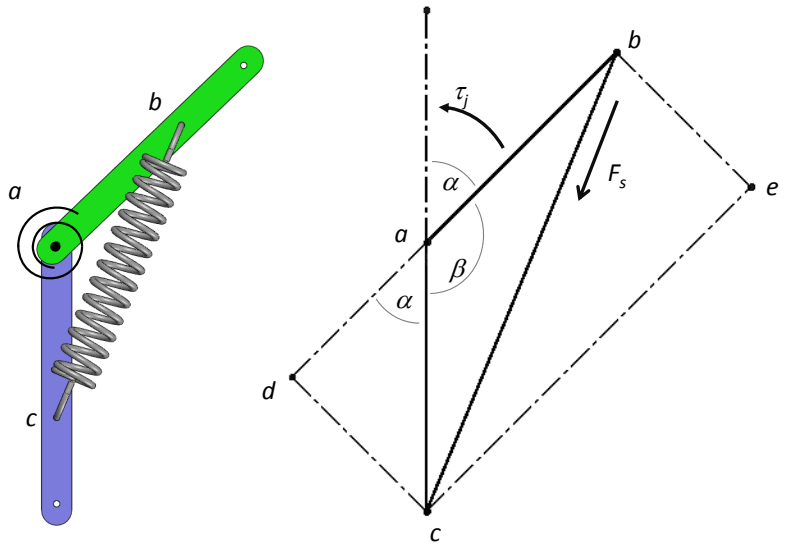

Figure B.14: The geometry of an over center spring mechanism.

The ratio of the maximum spring extension to its free length can be used to illustrate the impact of the use of real vs ideal springs. Figure B.15 shows the performance of the over center spring mechanism with a range of balance spring. In this example links l_{ab} and l_{ac} were equal length. The free length of the balance spring was varied between 0% and 60% of the extended spring length. The spring rates were normalized so all balance mechanisms produced perfect torque balance at 45°. The $x_o = 60\%$ spring required a spring rate 2.85 times that of the ideal spring to produce the same balance torque at 45°.

B.3.1 Over Center Spring with Sliding Link

Figure B.15 shows a clear decline in performance for a 60% spring at deflections over 50° and tracking errors of approximately 10% of peak torque over a range of 0-45°. The inclusion of a sliding link mechanism can both greatly improve tracking

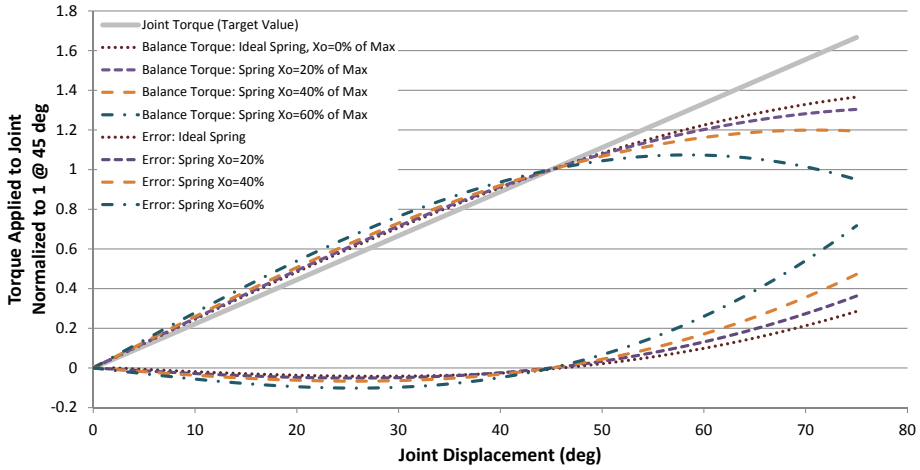

Figure B.15: Effect of spring free length on system balance performance. X_o is the ratio of the maximum spring extension vs. the free height of the spring. The 60% value is a realistic value for short, stiff extension springs.

performance as well as the operating range of the mechanism. Figure B.16 shows a concept which separates the control handle (l_{bf}) and spring link (l_{ab}).

The balance torque applied by this mechanism is:

$$\tau = F_s \frac{l_{cg}}{l_{bc}} l_{bf} \tag{B.36}$$

where F_s is the tension force of the spring and the ratio represents the portion of l_{bc} which is normal to the effect lever arm l_{ab}. The top term of the ratio, l_{cg} is found by extending a line from c which is perpendicular to line l_{bf} (extended to g).

$$l_{cg} = (l_{af} + l_{ac}) \sin(\alpha) \tag{B.37}$$

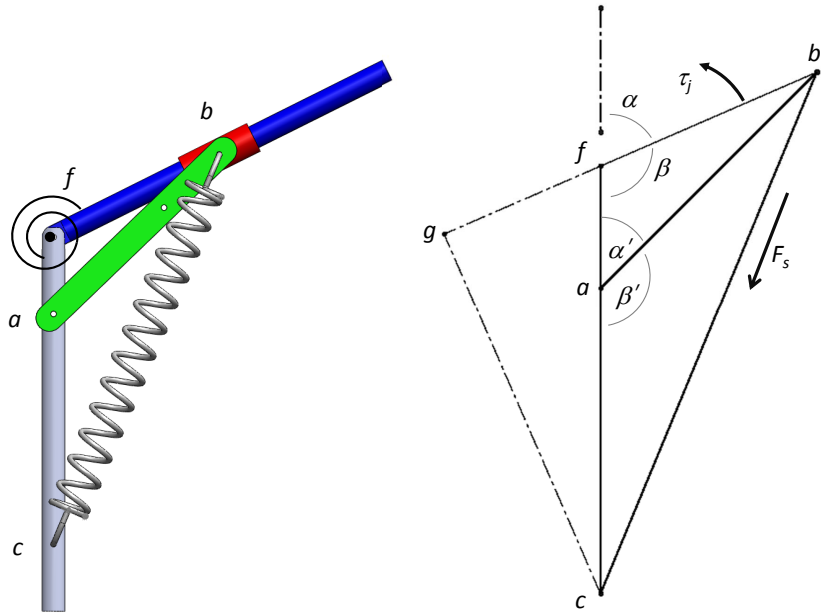

Figure B.16: The geometry of an over center spring mechanism using a sliding link to improve working range and linearity. The red collar (b) is able to slide along the control handle (l_{bf}).

The law of cosines is used to solve for α' with

$$\frac{\sin\beta}{l_{ab}} = \frac{\sin(\pi - \beta - \alpha')}{l_{af}} \tag{B.38}$$

$$\alpha' = \alpha - \arcsin(\sin\beta \frac{l_{af}}{l_{ab}}) \tag{B.39}$$

The control link length, l_{bf} is found using the law of cosines:

$$l_{bf} = \sqrt{(l_{af}^2 + l_{ab}^2 - 2 l_{af} l_{ab} \cos\alpha\prime)} \tag{B.40}$$

The total length of the spring, l_{bc} (free length plus extension) is:

$$l_{bc} = \sqrt{(l_{ac} + l_{ab}\sin\alpha\prime)^2 + (l_{ab}\cos\alpha\prime)^2)} \tag{B.41}$$

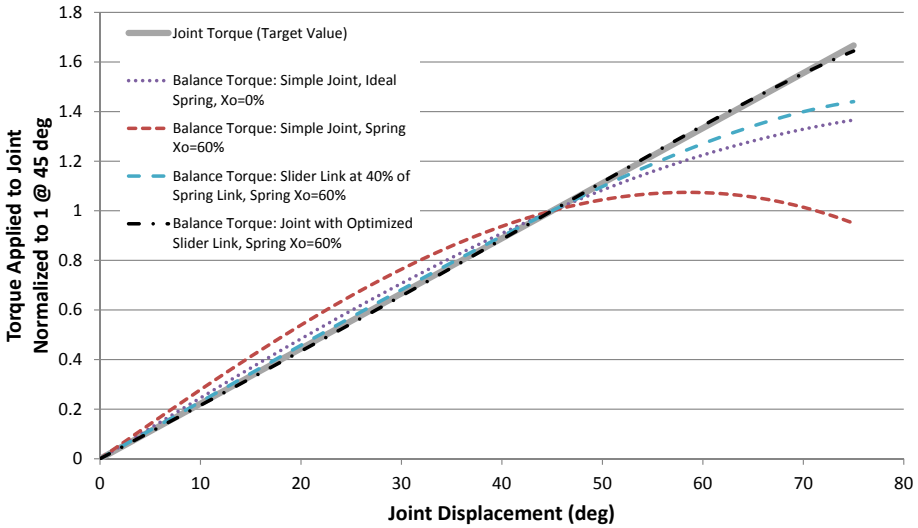

Figure B.17: The geometry of an over center spring mechanism using a sliding link to improve working range and linearity. The red collar (b) is able to slide along the control handle (l_{bf}).

With the total spring length the tension in the spring is,

$$F_s = k_s(l_{bc} - X_o) \tag{B.42}$$

where k_s is the spring constant and X_o is the free length of the spring.

In Figure B.16, the distance between joints located at points a and f can be optimized based on the ratio of spring free length to maximum extension length. To accomplish this the error between the effective torque of the continuum joint and the balance torque applied by the mechanism is discretized over the working range of interest. The squared sum of error is used as an objective function to optimize the length l_{af}. Figure B.17 shows the results of this optimization as well as the improvement in performance of the sliding link vs the simple over center spring balance mechanism. As before the spring rate was selected to produce perfect balance

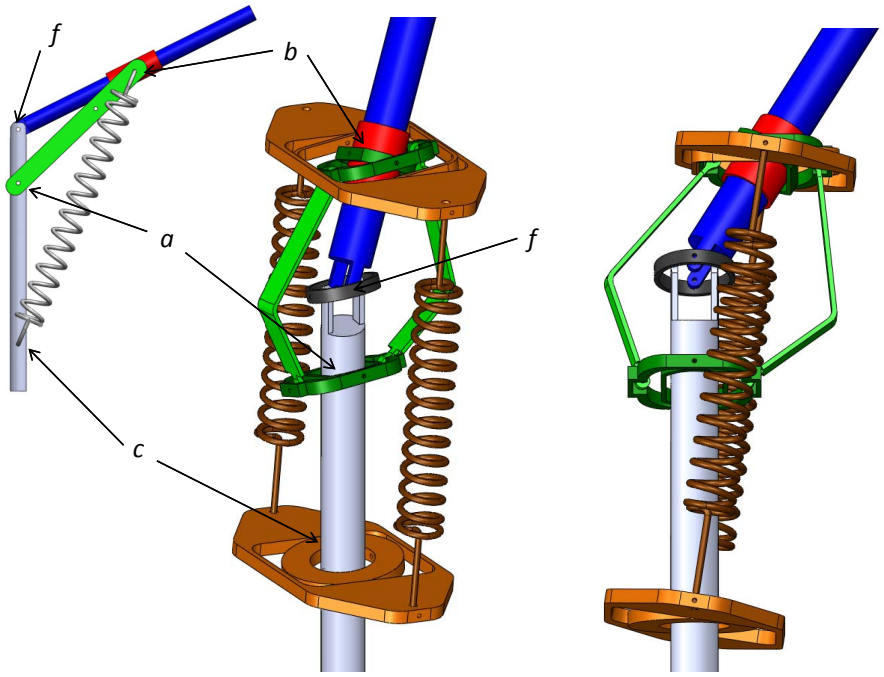

Figure B.18: 2 DOF implementation of the sliding link, over center spring mechanism. Equivalent kinematic points are indicated. Link a-b in the single DOF model is replaced with a parallelogram structure creating a virtual link connecting points at the centers of the two gimbals. The links connecting the gimbals are doglegged for clearance. The pair of gimbal supported springs act as a single virtual spring connecting the centers of the spring gimbals.

at 45°. Over 0-45° with the simple over center balance mechanism an ideal spring produced an error of 4.2% of the torque at 45°. The use of a real spring with a free length which is 60% of the maximum length had a peak error of 10% of the torque at 45°. A base line sliding link mechanism using a 60% spring showed significant improvement over either simple mechanisms. The torque error was reduced to 1.5% of the 45° value. With optimization and retaining the same 60% spring the performance improves to a 1% peak error and a realistic extension of the working range out to at least 75°. Thus the sliding link mechanism both significantly improves linearity and working range.

The sliding link mechanism can be extended into a 2 DOF model with the use of a series of gimbal supported virtual links (Figure B.18). The pivoting links of the single DOF design are replaced with parallelogram structures consisting of gimbals at opposite ends connected by springs or doglegged links. The effect of the parallelogram structure is that of a kinematic link connecting the centers of the respective gimbals. The use of gimbals to create an effective single spring will be shown in practice in the tool design of Chapter 6. Because the virtual links are the kinematic equivalent to those of the single DOF case, the effective link lengths are unchanged with the addition of the second DOF.

Bibliography

[1] Cambridge Endoscopic Devices, Inc. Farmingham, MA (USA).

[2] Intuitive Surgical Incorporated.

[3] KARL STORZ GmbH & Co. KG, Tuttlingen, Germany.

[4] RealHand TM High Dexterity (HD) Instruments, Novare Surgical Systems, Inc.

[5] John B. Adams, Peter G. Schulam, Robert G. Moore, Alan W. Partin, and Louis R. Kavoussi. New laparoscopic suturing device: Initial clinical experience. *Urology*, 46:242–245, 1995.

[6] Ron Alterovitz, Kenneth Y. Goldberg, Jean Pouliot, and I-Chow Hsu. Sensorless motion planning for medical needle insertion in deformable tissues. *IEEE Trans. Information Technology in Biomedicine*, 13(2):217–225, March 2009.

[7] K.S. Arun, T.S. Huang, and S.D Blostein. Least-squares fitting of two 3-D point sets. *IEEE Transactions on Pattern Analysis and Machine Intelligence*, 9:698–700, 1987.

[8] Shorya Awtar, Tristan T. Trutna, Rosa Abani, Jens M. Nielsen, and Andrew B. Mansfield. Flexdex: A minimally invasive surgical tool with enhanced dexterity and intuitive actuation. In *Proceedings of the ASME 2009 International Design Engineering Technical Conferences & Computers and Information in Engineering Conference*, 2009.

[9] Peter Berkelman and Ji Ma. A compact modular teleoperated robotic system for

laparoscopic surgery. *International Journal of Robotics Research*, 28(9):1198–1215, 2009.

[10] J. R. Torres Bermudez, G. Buess, M. Waseda, I. Gacek, F. Becerra Garcia, G. A. Manukyan, and N. Inak. Laparoscopic intracorporal colorectal sutured anastomosis using the radius surgical system in a phantom model. *Surgical Endoscopy*, 23:1624–1632, 2009.

[11] Paul J Besl and Neil D McKay. A method for registration of 3-D shapes. *IEEE Transactions on Pattern Analysis and Machine Intelligence*, 14:239–256, 1992.

[12] J Beutel, J M Fitzpatrick, S C Horii, Y Kim, H L Kundel, M Sonka, and R L Van Metter. *Handbook of Medical Imaging*, volume 2. SPIE Press, 2000.

[13] E.M. Boctor, M.A. Choti, E.C. Burdette, and R. J Webster III. Three-dimensional ultrasound-guided robotic needle placement: An experimental evaluation. *International Journal of Medical Robotics and Computer Assisted Surgery*, 4:180–191, 2008.

[14] Paul Breedveld, Jules S. Scheltes, Esther M. Blom, and Johanna E.i. Verheij. A new, easily miniaturized steerable endoscope. *IEEE Engineering In Medicine And Biology Magazine*, 5:40–47, 2005.

[15] J. Burgner, A. L. Simpson, J. M. Fitzpatrick, R. A. Lathrop, S. D. Herrell, M. I. Miga, and R. J. Webster III. A study on the theoretical and practical accuracy of conoscopic holography-based surface measurements: toward image

registration in minimally invasive surgery. *International Journal of Medical Robotics and Computer Assisted Surgery*, 2013.

[16] David B. Camarillo, Christopher F. Milne, Christopher R. Carlson, Michael R. Zinn, and J. Kenneth Salisbury. Mechanics modeling of tendon-driven continuum manipulators. *IEEE Transactions on Robotics*, 24(6):1262–1273, 2008.

[17] Jonathan C. Carr, Richard K. Beatson, Jon B. Cherrie, Tim J. Mitchell, W. Richard Fright, Bruce C. McCallum, and Tim R. Evans. Reconstruction and representation of 3D objects with radial basis functions. In *Proceedings of ACM SIGGRAPH 2001*, Computer Graphics Proceedings, Annual Conference Series, pages 67–76, August 2001.

[18] Jonathan C. Carr, W. Richard Fright, and Richard K. Beatson. Surface interpolation with radial basis functions for medical imaging. *IEEE Transactions On Medical Imaging*, 16:96–107, 1997.

[19] David M. Cash, William C. Chapman, Hiromi Terawaki, Benoit M. Dawant, Robert L. Galloway, and Michael I. Miga. Incorporation of a laser range scanner into image-guided liver surgery: Surface acquisition, registration, and tracking. *Medical Physics*, 30:1671–1682, 2003.

[20] Murat Cenk Cavusoglu, Isela Villanueva, and Frank Tendick. Workspace analysis of robotic manipulators for a teleoperated suturing task. *IEEE/RSJ International Conference on Intelligent Robots and Systems*, 2001.

[21] Kevin Cleary and Terry M. Peters. Image-guided interventions: Technology

review and clinical applications. *Annual Review of Biomedical Engineering*, 12:119–142, 2010.

[22] Logan W. Clements, David M. Cash, William C. Chapman, Robert L. Galloway, and Michael I. Miga. Robust surface registration using salient anatomical features in image-guided liver surgery. *Medical Physics*, 35:2528–40, 2008.

[23] K Daniilidis. Eye-hand calibration using dual quaternions. *International Journal of Robotics Research*, 18:286–298, 1999.

[24] Arati S. Deo and Ian D. Walker. Overview of damped least-squares methods for inverse kinematics of robot manipulators. *Journal of Intelligent and Robotic Systems*, 14:43–68, 1995.

[25] Jacco Drenth and Just L. Herder. Numerical Optimization of the Deisng of a Laparoscopic Grasper, Statically Balanced with Normal Springs. In *Proceedings of the ASME International Design Engineering Technical Congerences and Computer and Information in Engineering Conference - 2004*, pages 923–933, 2004.

[26] J. L. Farrell and J. C. Stuelpnagel. Problem 65-1: A least squares estimate of satellite attitude. *SIAM*, 8:384–386, 1966.

[27] G. Fichtinger, A. Deguet, K. Masamune, G. S. Fischer, E. Balogh, H. Mathieu, R.H. Taylor, L. M. Fayad, and S. J. Zinreich. Needle insertion in CT scanner with image overlay -cadaver studies. *Seventh International Conference on Med-*

ical Image Computing and Computer-Assisted Intervention, 3217:795–783, Oct 2004.

[28] Flavia Filimon. Human cortical control of hand movements: Perietofrontal networks for reaching, grasping and pointing. *The Neuroscientist*, 16:338–407, 2010.

[29] Julius Fine. Microlaryngoscopy with a new laryngoscope. *Archives of Otolaryngology*, 85:216–217, 1967.

[30] Gregory S. Fischer, Anton Deguet, Csaba Csoma, Russell H. Taylor, Laura Fayad, John A. Carrino, S James Zinreich, and Gabor. Fichtinger. MRI image overlay: Application to arthrography needle insertion. *Computer Aided Surgery*, 12:2–14, 2007.

[31] Robert L. Galloway Jr. The process and development of image-guided procedures. *Annual Review of Biomedical Engineering*, Vol. 3:83–108, 2001.

[32] Ian A. Gravagne and Ian D. Walker. On the kinematics of remotely actuated continuum robots. In *Proceedings of the 2000 IEEE International Conference on Robotics & Automation*, pages 2544–2550, 2000.

[33] W. E. L. Grimson, G. J. Ettinger, S. J. White, T. Lozano-PCrez, W. M. III Wells, and R. Kikinis. An automatic registration method for frameless stereotaxy, image guided surgery, and enhanced reality visualization. *IEEE Transactions On Medical Imaging*, 15:129–139, April 1996.

[34] Yves Guiard. Asymmetric division of labor in human skilled bimanual action: The kinematic chain as a model. *Journal of Motor Behavior*, 19, 1987.

[35] Gary S. Guthart and Jr. J. Kenneth Salisbury. The intuitive telesurgery system: Overview and application. In *Proceedings of 2000 IEEE International Conference on Intelligent Robots and Systems*, 2000.

[36] Mitsuhiro Hayashibe and Yoshihiko Nakamura. Laser-pointing endoscope system for intraoperative 3d geometric registration. In *Proceedings of the 2001 IEEE International Conference on Robotics and Automation*, 2001.

[37] Mitsuhiro Hayashibe, Naoki Suzuki, and Yoshihiko Nakamura. Laser-scan endoscope system for intraoperative geometry acquisition and surgical robot safety management. *Medical Image Analysis*, 10:509–519, 2006.

[38] Just L. Herder. Design of Spring Force Compensation Systems. *Mechanism and Machine Theory*, 33:151–161, 1998.

[39] Just L. Herder. *Energy-free Systems; Theory, conception, and design of statically balanced spring mechanisms*. PhD thesis, Delft, 2001.

[40] Alan J. Herline, Jeannette L. Herring, James D. Stefansic, William C. Chapman, Robert L. Galloway, and Benoit M. Dawant. Surface registration for use in interactive image-guided liver surgery. In C. Taylor and A. Colchester, editors, *Medical Image Computing and Computer-Assisted Intervention - MICCAI 99*, pages 892–899, 1999.

[41] S. Duke Herrell, Robert L. Galloway, and Li-Ming Su. Image-guided robotic surgery: update on research and potential applications in urologic surgery. *Current Opinion Urology*, 22:47–54, 2012.

[42] Alexander T. Hillel, Ankur Kapoor, Nabil Simaan, Russell H. Taylor, and Paul Flint. Applications of robotics for laryngeal surgery. *Otolaryngologic Clinics of North America*, pages 781–791, 2008.

[43] H Hilpert. Weight balancing of precision mechanical instruments. *Journal of Mechanisms*, 3(2):289–302, 1968.

[44] Shigeo Hirose. *Biologically Inspired Robots: Snake-Like Locomotors and Manuiplulators*. Oxford University Press, 1993.

[45] Geza J. Jako. Laryngoscope for microscopic observation, surgery, and photography; the development of an instrument. *Archives of Otolaryngology*, 91:196–199, 1970.

[46] Joris E.N. Jaspers and Cornelis A. Grimbergen. Mechanical manipulator for intuitive control of endoscopic instruments with seven degrees of freedom. In *IEEE International Conference on Systems, Man and Cybernetics*, pages 2479–2485, 2004.

[47] Filip Jelinek, Rob Pessers, and Paul Breedveld. Dragonflex smart steerable laparoscopic instrument. *Journal of Medical Devices*, 7:020911–1 to 020911–2, 2013.

[48] Ankur Kapoor, Nabil Simaan, and Russell H. Taylor. Suturing in confined spaces: Constrained motion control of a hybrid 8-dof robot. In *Proceedings of the 2005 IEEE International Conference on Robotics and Automation*, pages 452–459, 2005.

[49] Ankur Kapoor, Kai Xu, Wei Wei, Nabil Simaan, and Russell H. Taylor. Telemanipulation of snake-like robots for minimally invasive surgery of the upper airway. *MICCAI 2006*, 2006.

[50] Moon Jung Kim, Eric J Hunter, and Ingo R Titze. Comparison of human, canine, and ovine laryngeal dimensions. *The Annals of Otology, Rhinology & Laryngology*, 113:60–68, 2004.

[51] O. Kleinsasser. A larynx-microscope for early diagnosis and differential-diagnosis of carcinoma of the larynx, pharynx and oral cavity. *Z Laryng Rhinol Otol*, 40:276–279, 1961.

[52] John W. Krakauer. Motor learning and consolidation: The case of visuomotor rotation. *Advances in Experimental Medicine and Biology*, 629:405–421, 2009.

[53] V. Kumar and N. Ulrich. Mechanical design methods of improving manipulator performance. In *Proceedings of the 5th International Conference on Advanced Robotics*, pages 515–520, 1991.

[54] V. Kumar and N. Ulrich. Passive gravity compensation for robot manipulators. In *Proceedings of the IEEE International Conference on Robotics and Automation*, pages 1536–1541, 1991.

[55] R. A. Lathrop, T. T. Cheng, and R. J. Webster III. Conoscopic holography for image registration: A feasibility study. *Proceedings of SPIE*, 2009.

[56] R. A. Lathrop, T. T. Cheng, and R. J. Webster III. Laparoscopic image guidance via conoscopic holography. *ASME Journal of Medical Devices*, 3, 2009.

[57] R. A. Lathrop, D. C. Rucker, and R. J. Webster III. Guidance of a steerable cannula robot in soft tissue using preoperative imaging and conoscopic surface contour sensing. In *IEEE International Conference on Robotics and Automation*, pages 5601–5606, 2010.

[58] William E. Lorensen and Harvey E. Cline. Marching cubes: A high resolution 3D surface construction algorithm. *Computer Graphics*, 21(4):163–169, July 1987.

[59] Yair Lotan. Is robotic surgery cost-effective: no. *Current Opinion in Urology*, 22:66–69, 2012.

[60] Mitchell J. H. Lum, Diana C. W. Friedman, Ganesh Sankaranarayanan, Hawkeye King, Kenneth Fodero, Rainer Leuschke, Blake Hannaford, Jacob Rosen, and Mika N. Sinanan. The raven: Design and validation of a telesurgery system. *The International Journal of Robotics Research*, 28:1183–1197, 2009.

[61] Calvin R. Maurer, Jr., Robert J. Maciunas, and J. Michael Fitzpatrick. Registration of head CT images to physical space using a weighted combination of points and surfaces. *IEEE Transactions On Medical Imaging*, 17(5):753–761, October 1998.

[62] Ian K McLeod and Patrick C Melder. Da vinci robot-assisted excision of a vallecular cyst: A case report. *Ear, Nose & Throat Journal*, 84:170–172, 2005.

[63] A. Melzer, K. Kipfmuller, and B. Halfar. Deflectable endoscopic instrument system denis. *Surgical Endoscopy*, 11:1045–1051, 1997.

[64] William Mendenhall and Terry Sincich. *Statistics for Engineering and the Sciences (4th Edition)*. Prentice Hall, 1995.

[65] Michael I. Miga, Tuhin K. Sinha, David M. Cash, Robert L. Galloway, and Robert J. Weil. Cortical surface registration for image-guided neurosurgery using laser-range scanning. *IEEE Transactions On Medical Imaging*, 22(8):973–985, August 2003.

[66] Clyde H Moon. *Cam Design*. Commerical Cam Co. Inc, 1961.

[67] R. M. Murray, Z. Li, and S. S. Sastry. *A Mathematical Introduction to Robotic Manipulation*. CRC Press, Boca Raton, FL, 1994.

[68] Richard M. Murray, Zexiang Li, and S. Shankar Sastry. *A Mathematical Introduction to Robotic Manipulation*. CRC Press, 1994.

[69] Florent Nageotte, Philippe Zanne, Michel de Mathelin, and Christophe Doignon. A circular needle path planning method for suturing in laparoscopic surgery. *International Conference on Robotics and Automation*, 5:514–519, 2005.

[70] J. R. Napier. The prehensile movements of the human hand. *Journal of Bone and Joint Surgery*, 38 B(4):902–913, 1956.

[71] MD Neil G. Hockstein, BS J. Paul Nolan, MD Bert W. OMalley, Jr, and MD Y. Joseph Woo. Robot-assisted pharyngeal and laryngeal microsurgery: Results of robotic cadaver dissections. *The Laryngoscope*, 115:1003–1008, 2005.

[72] Ninh T. Nguyen, Kathrin L. Mayer, Richard J. Bold, Mike Larson, Samia Foster, Hung S. Ho, and Bruce M. Wolfe. Laparoscopic suturing evaluation among surgical residents. *Journal of Surgical Research*, 93:133–136, 2000.

[73] Terry Peters. *Image-Guided Interventions: Technology and Applications*. Springer, 2008.

[74] Josien P. W. Pluim, J. B. Antoine Maintz, and Max A. Viergever. Mutual information based registration of medical images: a survey. *IEEE Transactions On Medical Imaging*, 22:986–1004, 2003.

[75] Katherine M. Powell and Mary I. Frecker. Method for optimization of a nonlinear static balance mechanism with application to ophthalmic surgical forceps. In *Proceedings of ASME 2005 International Design Engineering Technical Conferences & Comoputers and Information in Engineering Conference*, 2005.

[76] Mauro Prasciolu. *3D Laser Scanner Based On Surface Silicon Micromachining Techniques For Shape And Size Reconstruction Of The Human Ear Canal*. PhD thesis, University of Trieste, 2007.

[77] Rhonda Prewitt, Victor Bochkarev, Corrigan L. McBride, Sonja Kinney, and Dmitry Oleynikov. The patterns and costs of the da vinci robotic surgery system in a large academic institution. *Journal of Robotic Surgury*, 2:17–20, 2008.

[78] Andreas Raabe M.D., Ph.D., Ren Krishnan M.D., Robert Wolff M.D., Elvis Hermann M.D., Michael Zimmermann M.D., Ph.D., and Volker Seifert M.D., Ph.D. Laser surface scanning for patient registration in intracranial image-guided surgery. *Neurosugery*, 50(4):797–803, April 2002.

[79] MD Reza Rahbar, DMD, MD Lynne R. Ferrari, MD Joseph G. Borer, and MD Craig A. Peters. Robotic surgery in the pediatric airway - application and safety. *Archives of Otolaryngology Head & Neck Surgery*, 133:46–50, 2007.

[80] W. W. Roberts, T. A. Dinkel, P. G. Schulam, L. Bonnell, and L. R. Kavoussi. Laparoscopic infrared imaging. *Surgical Endoscopy*, 11:1221–1223, 1997.

[81] G. Robinson and J.B.C. Davies. Continuum robots - a state of the art. In *Proceedings of the 1999 IEEE International Conference on Robotics and Automation*, pages 2849–2854, 1999.

[82] D. C. Rucker and R. J. Webster III. Statics and dynamics of continuum robots with general tendon routing and external loading. *IEEE Transactions on Robotics*, 27(6):1033–1044, 2011.

[83] D. C. Rucker, B. A. Jones, and R. J. Webster III. A model for concentric tube continuum robots under applied wrenches. *IEEE International Conference on Robotics and Automation*, 2010. (Submitted).

[84] D. C. Rucker and Robert J. Webster III. Parsimonious evaluation of concentric-tube continuum robot equilibrium conformation. *IEEE Transactions on Biomedical Engineering*, 56:2308–2311, 2009.

[85] Jeffrey A. Saunders and David C. Knill. Visual feedback control of hand movements. *The Journal of Neuroscience*, 24:3223–3234, 2004.

[86] Kurt Schicho, Michael Figl, Rudolf Seemann, Markus Donat, Michael L. Pretterklieber, Wolfgang Birkfellner, Astrid Reichwein, Felix Wanschitz, Franz Kainberger, Helmar Bergmann, Arne Wagner, and Rolf Ewers. Comparison of laser surface scanning and fiducial markerbased registration in frameless stereotaxy. *Journal of Neurosurgery,*, 106:704–709, 2007.

[87] P. H. Schonemann. A generalized solution of the orthogonal procrustes problem. *Psychometrika*, 31:1–10, 1966.

[88] Nabil Simaan. Snake-like units using flexible backbones and actuation redundancy for enhanced miniaturization. In *Proceedings of the 2005 IEEE International Conference on Robotics and Automation*, pages 3012–3017, 2005.

[89] Nabil Simaan, Russell Taylor, and Paul Flint. A dexterous system for laryngeal surgery. In *Proceedings of the 2004 IEEE International Conference on Robotics & Automation*, pages 351–357, 2004.

[90] Tobias Simpfendrfer, Matthias Baumhauer, Michael Mller, Carsten N. Gutt, Hans-Peter Meinzer, Jens J. Rassweiler, Selcuk Guven, and Dogu Teber. Aug-

mented reality visualization during laparoscopic radical prostatectomy. *Journal of Endourology*, 25:1841–1845, 2010.

[91] A. L. Simpson, J. Burgner, I. Chen, T. S. Pheiffer, K. Sun, R. C. Thompson, R. J. Webster, , and M. I. Miga. Intraoperative brain resection cavity characterization with conoscopic holography. In *SPIE 2012 Medical Imaging: Image-Guided Procedures, Robotic Interventions, and Modeling Conference*, 2012.

[92] A. L. Simpson, J. Burgner, C. L. Glisson, S. D. Herrell, B. Ma, R. J. Webster III, and M. I. Miga. Comparison study of intraoperative surface acquisition methods for surgical navigation. *IEEE Transactions on Biomedical Engineering*, 60:1090–1099, 2013.

[93] Gabriel Sirat and Demetri Psaltis. Conoscopic holography. *Optics Letters*, 10(1):4–6, January 1985.

[94] Gabriel Y Sirat, Freddy Paz, Gregory Agronik, and Kalman Wilner. Conoscopic systems and conoscopic holography. Optimet. Optimet White Paper.

[95] Aaron Stapel and Just L. Herder. Feasibility study of a fully compliant statically balanced laparoscopic grasper. In *Proceedings of ASME 2004 Design Engineering Technical Conferences and Computers and Information in Engineering Congerence*, 2004.

[96] G. Stetten, V. Chib, and R. Tamburo. System for location-merging ultrasound images with human vision. *IEEE Procedings of the Applied Imagery Pattern Recognition Workshop*, pages 200–205, 2000.

[97] Gerald Y. Tan, Raj K. Goel, JihadH. Kaouk, and Ashutosh K. Tewari. Technological advances in robotic -assisted laparoscopic surgery. *Urologic Clinics of North America*, 36:237–249, 2009.

[98] Freek L.S. te Riele and Just L. Herder. Perfect static balance with normal springs. In *Proceedings of ASME 2001 Design Engineering Technical Conferences and Computers and Information in Engineering Conference*, 2001.

[99] P. H. Tidwell, N. Bandukwala, S. G. Dhande, C. F. Reinholtz, and G. Webb. Synthesis of wrapping cams. *Transactions of the ASME*, 116:634–638, 1994.

[100] Nima Tolou, Gerwin Smit, Ali A. Nikooyan, Dick H. Plettenburg, and Just L. Herder. Stiffness compensation mechanism for body powered hand prostheses with cosmetic covering. *Journal of Medical Devices*, 6, 2012.

[101] Lloyd N. Trefethen and David III Bau. *Numerical Linear Algebra*. Society for Industrial and Applied Mathematics, 1997.

[102] Domingos H. Tsuji, Luciana Miwa Nita, Adriana Hachiya, Rui Imamura, and Luiz U. Sennes. T-shaped microsuture: A new suture technique for laryngeal microsurgery. *Journal of Voice*, 23:739–742, 2009.

[103] Peter van Dam, Jan Hauspy, Luc Verkinderen, Bich Trinh, Luc Van Looy, and Luc Dirix. Do costs of robotic surgery matter? *Advanced Gynecologic Endoscopy*, pages 213–222, 2011.

[104] F. Van Meer, J. Philippi, D. Esteve, and E. Dombre. Compact generic multi-

channel plastic joint for surgical instrumentation. *Mechatronics*, 17:562–569, 2007.

[105] Xiaofei Wang, Shuxin Wang, Jianmin Li, Guokai Zhang, and Zhiliang Wu. Conceptual design of a novel multi-dof manual instrument for laparoscopic surgery. *The International Journal Of Medical Robotics And Computer Assisted Surgery*, 10.1002, 2012.

[106] Robert J. Webster, III and Bryan. A. Jones. Design and kinematic modeling of constant curvature continuum robots: A review. *Iternational Journal of Robotics Research*, 29(13):1661–1683, 2010.

[107] R. J. Webster III, J. M. Romano, and N. J. Cowan. Mechanics of precurved-tube continuum robots. *IEEE Transactions on Robotics*, 25(1):67–78, 2009.

[108] P. Woo, J. Casper, B. Griffin, R. Colton, and D. Brewer. Endoscopic microsuture repair of vocal fold defects. *Journal of Voice*, 9:332–339, 1995.

[109] Kai Xu, Roger E. Goldman, Jienan Ding, Peter K. Allen, Dennis L. Fowler, and Nabil Simaan. System design of an insertable robotic effector platform for single port access (spa) surgery. In *The 2009 IEEE/RSJ International Conference on Intelligent Robots and Systems*, pages 5546–5552, 2009.

[110] Kai Xu and Nabil Simaan. An investigation of the intrinsic force sensing capabilities of continuum robots. *IEEE Transactions on Robotics*, 23(3):576–587, 2008.

[111] Karel J. Zuzak, Sabira C. Naik, George Alexandrakis, Doyle Hawkins, Khosrow Behbehani, and Edward H. Livingston. Characterization of a near-infrared laparoscopic hyperspectral imaging system for minimally invasive surgery. *Analytical Chemistry*, 79:4709–4715, 2007.